CENTRE DE RECERCA MATEMÀTICA

Title:	*Workshop and Advanced Course on Deterministic and Stochastic Modeling in Computational Neuroscience and Other Biological Topics*
Journal Information:	*CRM Preprints*,
Author(s):	Workshop and Advanced Course on Deterministic and Stochastic Modeling in Computational Neuroscience and Other Biological Topics.
Volume, pages:	*1-149*, DOI:[--]

Workshop and Advanced Course on Deterministic and Stochastic Modeling in Computational Neuroscience and Other Biological Topics

Centre de Recerca Matemàtica
Bellaterra

May 11 to 15, 2009

Acknowledgements. The Workshop and Advanced Course on Deterministic and Stochastic Modeling in Computational Neuroscience and Other Biological Topics is supported by the Ingenio Mathematica Programme (ref. C3-150) and by the Ministerio de Ciencia e Innovación (ref. MTM2007-30707-E).

Contents

Advanced Course

Workshop

Advanced Course

Schedule Advanced Course

Monday, May 11

9:00 – 9:30	REGISTRATION
9:30 – 10:30	*The neurodynamics of attention, memory and decision-making* **Gustavo Deco**, Universitat Pompeu Fabra
10:30 – 11:00	Coffee Break
11:00 – 12:00	*The neurodynamics of attention, memory and decision-making* **Gustavo Deco**, Universitat Pompeu Fabra
12:00 – 13:00	*Stochastic processes and PDEs in mathematical biology* **Juan J.L. Velázquez**, Consejo Superior de Investigaciones Científicas
13:00 – 15:00	Lunch
15:00 – 16:00	*Stochastic processes and PDEs in mathematical biology* **Juan J.L. Velázquez**, Consejo Superior de Investigaciones Científicas
16:00 – 16:15	Break
16:15 – 18:15	*Modeling large-scale dynamics in the primary visual cortex* **Louis Tao**, Beijing University

Thuesday, May 12

9:00 – 11:00	*The neurodynamics of attention, memory and decision-making* **Gustavo Deco**, Universitat Pompeu Fabra
11:00 – 11:30	Coffee Break
11:30 – 13:30	*Stochastic processes and PDEs in mathematical biology* **Juan J.L. Velázquez**, Consejo Superior de Investigaciones Científicas
13:30 – 15:30	Lunch
15:30 – 16:30	*Modeling large-scale dynamics in the primary visual cortex* **Louis Tao**, Beijing University
16:30 – 16:45	Break
16:45 – 17:45	*Modeling large-scale dynamics in the primary visual cortex* **Louis Tao**, Beijing University

The neurodynamics of attention, memory and decision-making

Gustavo Deco

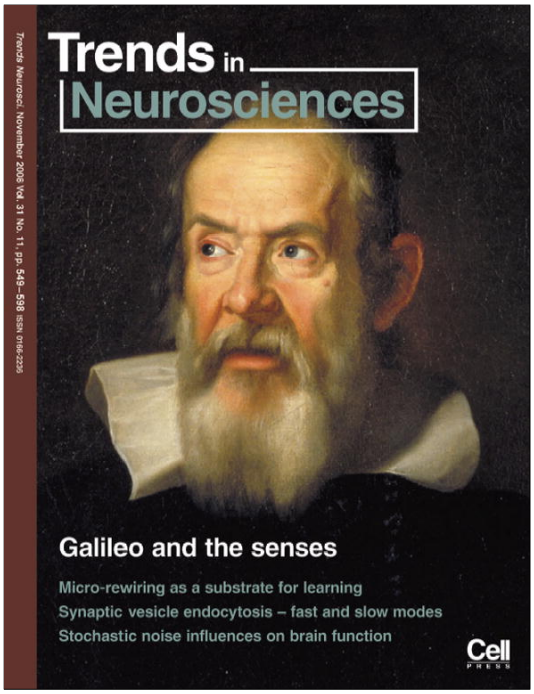

Review

Cell PRESS

The role of fluctuations in perception

Gustavo Deco[1] and Ranulfo Romo[2]

[1] Institució Catalana de Recerca i Estudis Avançats, Universitat Pompeu Fabra, Department of Technology, Computational Neuroscience, Passeig de Circumval.lació, 8, 08003 Barcelona, Spain
[2] Instituto de Fisiología Celular, Universidad Nacional Autónoma de México, 04510 México, D.F. México

Noise contributed by the probabilistic spiking times of neurons has an important and advantageous role in brain function. We go beyond the deterministic noiseless description of the dynamics of cortical networks and show how the properties of the system are influenced by the spiking noise. We review here recent results that show the direct link between brain activity and psychophysically quantified behaviors during a somatosensory detection task. We focus on the following remarkable observation in this somatosensory task: when a near-threshold stimulus is presented, a sensory percept may or may not be produced. These perceptual judgments are believed to be determined by the fluctuation in activity of early sensory cortices. We show, however, that the behavioral outcomes associated with near-threshold stimuli depend on the neuronal fluctuations of more central areas to early somatosensory cortices. Furthermore, we show that the behavioral correlate of perceptual detection is given by a noise-driven transition in a multistable neurodynamical system. Thus, neuronal fluctuations can be an advantage for brain processing because they lead to probabilistic behavior in decision making in this and other sensory tasks.

Introduction

One of the most fundamental concepts in the psychology and philosophy of the mind is the notion of perception. Perception refers to the act of acquiring individual awareness of an event or entity external to one's self. The external physical event or entity exerts an effect on the senses that, after further cortical processing, generates a new grade of mind called a percept. Since the first days of psychology, two challenging questions have been: how is sensory information encoded and, in particular, how does further processing transform this represented information into the individual awareness of a percept? In other words, the essential problem is still the seminal concept of subjective sensation. More than one century ago, the pioneering research work of Ernst Heinrich Weber and Gustav Theodor Fechner [1] began to scrutinize the concept of sensation quantitatively by studying the interplay between the physical and psychical world with the experimental paradigm of perceptual detection. In this paradigm, human subjects have to report a produced or not produced sensory percept when a near-threshold sensory stimulus is presented. Nowadays, utilizing the same perceptual-detection paradigm, modern neuroscience aims to discover the neuronal correlates of sensation by showing how neural activity encodes the physical parameters of the sensory stimuli both in the periphery and central areas of the brain [2–4]. Single-cell recordings and functional magnetic resonance imaging open the possibility to investigate more closely the brain processing underlying the generation of a percept [3,5–9]. Electroencephalogram and magnetoencephalogram techniques have also been used to study the neural systems that are involved in perceptual decision making (for a review, see Ref. [10]). Now, it is possible to provide experimentally answers to a number of questions. For example, where and how in the brain do the neuronal responses that encode the sensory stimuli translate into responses that encode a perceptual decision [2,3]? What components of the neuronal activity evoked by a sensory stimulus are directly related to perception [5,6]? Where and how in the brain is sensory information stored in memory [11]?

Despite a large amount of measurements at all macroscopic, mesoscopic and microscopic neuroscience levels, understanding the brain processing involved in perception is difficult. The main problem is that perception can be described at many different levels of abstraction, from the high-level computational principles of processes involved in perception through to the neurophysiological principles by which neurons function. The solution of this problem requires a theoretical framework that explicitly establishes a link between the underlying neuronal substrate and the algorithmic computational level of perception in a unifying way. The benefits that might be gained from this linkage can help us to understand perceptual processes.

Computational neuroscience offers a framework for understanding the computational mechanisms underlying the neuronal correlates of perception. Computational models achieve this linkage by the explicit construction and simulation of microscopic models based on local networks with large numbers of neurons (>1000) and synapses (>1 000 000) that lead to the desired global behavior of the whole system. This type of biophysical realistic microscopic model is expressed by a dynamical system owing to the fact that processing does not operate in a completely feed-forward manner because recurrent feedback is also present [12]. Apparently even the simple detection of a stimulus can depend on dynamic interactions between different groups of neurons. At a neural level, backward connections are at least as numerous as feed-forward connections, and there are good grounds for supposing that these feedback connections have a necessary function in brain processing [13]. To understand information processing we need to understand the dynamic contributions from three feed-forward and feed-back processes over time, and this involves more than a one-sweep feed-forward computation [14–16]. An in-depth

Corresponding author: Deco, G. (gustavo.deco@upf.edu).

0166-2236/$ – see front matter doi:10.1016/j.tins.2008.08.007 Available online 25 September 2008

analytical study of these detailed microscopic dynamical models is not possible and, therefore, a reduction of the hypothesized models is necessary to establish a systematic relation between structure (parameters), dynamics and functional behavior (i.e. to solve the so-called 'inverse' problem). A mere simulation of brain functions is, in general, not useful because there are usually no explicit underlying first principles. To overcome this problem, statistical physics mean-field methods have been introduced to analytically reduce the system [17,18]*. Further simplifications are possible by reducing the system dynamics to a one-dimensional diffusion equation typically used for describing the behavioral level [19].

Many recent examples in the neuroscience literature (e.g. working memory [17], attention [15,16] and decision making [20]) advocate for a dynamical system approach that enables us to discover the neuronal computation underlying specific brain function by solving the neurodynamical inverse problem of finding the connectivity structure from which the measured neuronal correlates emerges. However, dynamics alone is not enough. Neuronal recordings are typically characterized by a high degree of variability in the firing activity both within and between trials. Usually both experimentalists and theoreticians assume that these fluctuations are irrelevant and consequently they average them over repeated measurements. Nevertheless, these stochastic fluctuations in the neuronal dynamics might actually not be just a concomitant feature of real brains but could have a functional role (for a review, see Ref. [21]). In fact, the probabilistic behavior observed during certain perceptual tasks indicates a link between the stochasticity at the cellular and behavioral level [22].

Here, we show that both neurodynamics and stochastic fluctuations are important, in the sense that both have an essential computational role for a complete explanation of perception. To show this, we take as a prototypical example the most elemental and historical task of perceptual detection mentioned here. By constructing and analyzing computational models, we establish the link that accounts for measurements both at the cellular and behavioral level. In particular, we demonstrate that in perceptual detection subjects exhibit probabilistic behavior, which trial-by-trial covariates with the firing activity of single-cell recordings. The theoretical analysis of the behavioral and neuronal correlates of sensation shows how variability at the neuronal level can give rise to probabilistic behavior at the network level and how these fluctuations influence network dynamics qualitatively.

The neurophysiology of perceptual decisions

The detection of sensory stimuli is among the simplest of perceptual experiences and is a prerequisite for any further sensory processing. A fundamental problem posed by the sensory detection tasks is that repeated presentation of a near-threshold stimulus might unpredictably fail or succeed in producing a sensory percept. Where in the brain are the neuronal correlates of these varying perceptual judgments? This problem has been recently addressed by de Lafuente and Romo [5,6]. These authors trained monkeys to perform a detection task (Figure 1a). In each trial, the animal had to report whether the tip of a mechanical stimulator vibrated or not (Figure 1b). Stimuli were sinusoidal, had a fixed frequency of 20 Hz and were delivered to the glabrous skin of one fingertip. Crucially, they varied in amplitude across trials. Stimulus-present trials were interleaved with an equal number of stimulus-absent trials in which no mechanical vibrations were delivered (Figure 1b). Depending on the responses of the monkeys, trials could be classified into four types of responses: hits and misses in the stimulus-present condition and correct rejections and false alarms in the stimulus-absent condition (Figure 1c). Stimulus-detection thresholds were calculated from the behavioral responses (Figure 1d). Previous studies seeking the neuronal correlates of sensory detection showed that, in the case of the vibrotactile stimuli, the responses of neurons of the primary somatosensory cortex (S1) account for the measured psychophysical accuracy. However, imaging and physiological studies show that, in addition to the sensory cortices, areas of the frontal lobe are also active during sensory detection and discrimination [3,7,23]. This evidence raises and important question: what are the specific functional roles of primary sensory cortices and association areas of the frontal lobe in perceptual detection?

To further test the contributions of these cortical areas in perceptual detection, de Lafuente and Romo [5,6] recorded the activity of S1 and medial-premotor-cortex (MPC; a frontal lobe area involved in motor planning and decision making [23]) neurons while monkeys performed the task (Figure 1). They found that the responses of S1 neurons varied as a function of the stimulus strength (Figure 1e) but did not correlate with the behavioral responses (Figure 1f). On the contrary, the responses of MPC neurons did not vary as a function of the stimulus strength (Figure 1e), but correlated with the behavioral responses on a trial-by-trial basis (Figure 1g). The activity of the MPC neurons was strong and sustained and, with near-threshold stimuli, it was clearly different for hit-and-miss trials (Figure 1g, upper left panel). Moreover, almost 70% of the false-alarm responses were predicted from increases in the activity of MPC neurons in stimulus-absent trials (Figure 1g, upper right panel). Interestingly, the activity of MPC neurons preceding the stimulus onset was higher during hits than during misses (Figure 1g). These early increases in activity predicted detection success significantly above chance. This increased pre-stimulus activity might be associated with trial history during a run. In fact, the probability of detection of a sub-threshold stimulus was increased in trials preceding a false alarm (see Figure 3f of Ref. [5]). Thus, increased responses of MPC neurons were associated with stimulus presence or with false alarms. These results further support a detection model in which, to judge the stimulus presence or absence, a central area(s) with internal fluctu-

* In the mean-field approximation, the currents impinging on each neuron in a population have the same statistics because the history of these currents is uncorrelated. The mean-field approximation entails replacing the time-averaged discharge rate of individual cells with a common time-dependent population activity (the ensemble average). Thus, in a statistical sense, the rate of a single neuron calculated across time is equivalent to the rate of activity across the neurons in a given population at a given time. These approximations enable us to reduce consistently the dynamics of a large number of differential equations describing each neuron in a population by a single rate equation describing the steady state of the population dynamics.

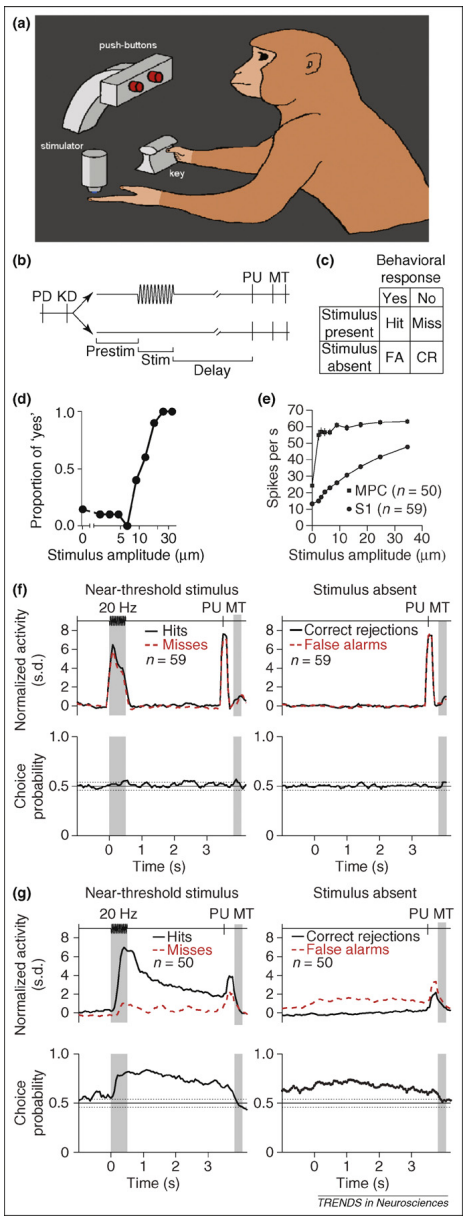

Figure 1. The detection task. **(a)** Drawing of a monkey working in the detection task. **(b)** The sequence of events during the detection trials. Trials began when the stimulation probe indented the skin of one fingertip of the left, retrained hand (probe down, PD). The monkey then placed its right, free hand on an immovable key (key down, KD). On half of the randomly selected trials, after a variable pre-stimulus period (Prestim, 1.5–3.5 s), a vibratory stimulus (Stim, 20 Hz, 0.5 s) was presented. Then, after a fixed delay period (Delay, 3 s), the stimulator probe moved up (probe up, PU), indicating to the monkey that it could make the response movement (MT) to one of the two buttons. The button pressed indicated whether or not the monkey felt the stimulus. Henceforth, these are referred to as 'yes' and 'no' responses, respectively. **(c)** Depending on whether the stimulus was present or absent and on the behavioral response, trial outcome was classified as a hit, miss, false alarm (FA) or correct reject (CR). Trials were pseudo-randomly chosen: 90 trials were stimulus absent (amplitude 0) and 90 trials were stimulus present with varying amplitudes (9 amplitudes with 10 repetitions each). **(d)** Classical psychometric detection curve obtained by plotting the proportion of 'yes' responses as a function of the stimulus amplitude. **(e)** Mean firing rate of hit trials for S1 ($n = 59$) and MPC ($n = 50$) neurons. **(f)** Comparison of normalized neuronal-population activity of S1 neurons during hits and misses for near-threshold stimuli and during correct rejections and false alarms in stimulus-absent trials. Normalized activity was calculated as a function of time, using a 200 ms window displaced every 50 ms. This was calculated by subtracting the mean activity and dividing by the standard deviation (s.d.) of the activity from a 200 ms window of the pre-stimulus period. The lower panels show the choice probability index as a function of time. This quantity measures the overlap between two response distributions: in this case, between hits and misses and between correct rejection and false-alarm trials. Dotted lines mark significance levels. **(g)** The same as in (f) but for a neuronal population activity of MPC neurons. Reproduced, with permission, from Ref. [5].

ations must track the activity of S1. These results indicate that perceptual judgments arise in the activity of frontal lobe neurons but not in sensory cortices. Importantly, internal fluctuations of frontal lobe neurons have an impact on the behavior of an animal, as shown by the data of de Lafuente and Romo [5,6].

Computing a percept: noise and neurodynamics

To understand the computational mechanisms underlying perceptual detection, we analyze here which kind of stochastic neurodynamical model underlies the experimental results of Ref. [5]. Their experimental results indicate that MPC neurons correlate with the behavioral performance, with a high firing rate for a 'yes' report and a low firing rate for a 'no' report. From a theoretical point of view, this indicates that the underlying neuronal substrate presents a bistable dynamic. For the same stimulus (amplitude intensity) two possible behavioral responses were observed, namely 'stimulus detection' and 'no stimulus detection'. These two possible choices are associated with two possible steady states (attractors) of the underlying neurodynamical system, which coexist for the same stimulus condition (i.e. the system is bistable). In this case, sufficiently strong probabilistic fluctuations could drive the system from the default stable spontaneous state (no stimulus detection) to the other stable stimulus-detection state corresponding to the generation of the percept. The computation of a percept is then understood as a fluctuation-driven, probabilistic transition to one of the two possible bistable decision states (see Ref. [22] for other examples of computation with noise). Thus, in the bistable regime, fluctuations are essential for perceptual detection and bears a striking resemblance to a decision-making mechanism [11,20,24,25], meaning paradoxically that perception results from a cognitive decision-making process.

A minimal network model that captures the computation involved in perceptual detection and that is consistent with the neurophysiological and behavioral evidence described earlier was proposed in Ref. [26]. Their model is schematically shown in Figure 2. The model consists of a network of spiking integrate-and-fire units organized into discrete populations of excitatory and inhibitory neurons.

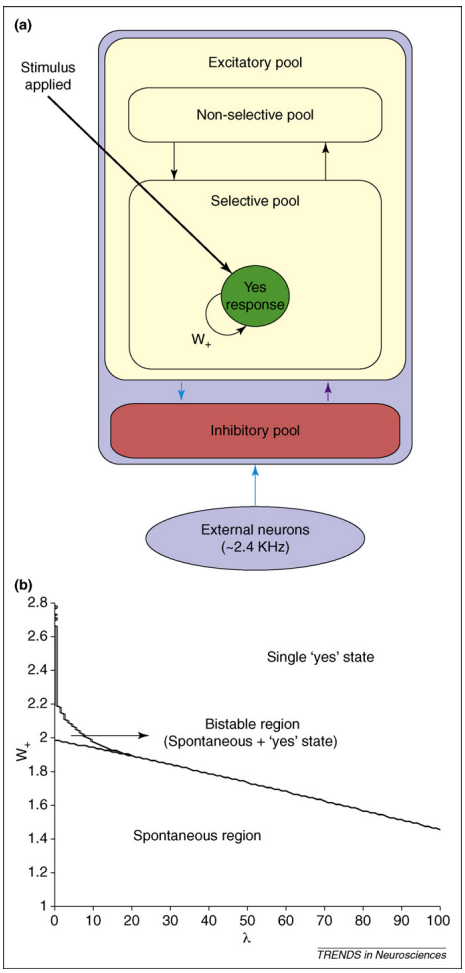

Figure 2. **(a)** The perceptual-detection model (NCYN) has excitatory populations selective to the applied vibrotactile stimulation. A 'no' response is given when the selective population has low activity and a 'yes' response is given when it has high activity. The arrows indicate the recurrent connections between the different neurons in a pool (see main text for more details). **(b)** Phase diagrams for the NYCN model for parameter exploration of the attractor states (stationary states) of the underlying dynamical system. The diagrams show the different attractor regions as a function of the stimulus input (λ) and the level of coupling (W_+) within the neurons of the same selective population (cohesion; see main text for more details).

Some excitatory 'selective' neurons were linked to the sensory input generated by external neurons, reflecting the presentation of vibrotactile stimulation. The other excitatory neurons were grouped into a 'non-selective' population and there was one additional pool of local inhibitory neurons that implemented competition in the network. Neurons in the network were connected by three types of receptors that mediate the synaptic currents coming into them: g-amino-3-hydroxy-5-methyl-4-isoxazolepropionic acid (AMPA), N-methyl-d-aspartic acid (NMDA) glutamate and γ-aminobutyric acid (GABA) receptors. Neurons within an excitatory population were mutually coupled with a strong self-supporting weight (W_+). In this network, called the 'non-competing yes neuron model' (NCYN), there was a single pool of excitatory units the activity of which was taken to reflect a 'yes' response to the presence of a vibrotactile stimulus.

To obtain the appropriate steady states for the perceptual-detection model and to capture the transient changes of the network enroute, the connectivity parameters that sustain the required two bistable steady states associated with a low or high activity for the selective population corresponding to a 'no' or 'yes' detection response, respectively, must be found. This is an inverse problem – first, the whole-system behavior (the steady state) is studied to obtain approximate parameters that enable the study of how the system evolved to the steady-state in the first place. We study the steady states of the system via the mean-field approach [17]. Using this approximation, the relevant parameter space given by the self-excitatory weight W_+ versus the external input λ can be scanned. Figure 2 also shows the parameter space for making a 'yes' response divided into two broad areas: where the self-excitatory weight was high when the model generated a 'yes' response across broad variations in λ and when the weight was low and the selective population maintained its spontaneous state across different values of λ (corresponding to a 'no' response). There was also a small bistable region of the parameter space, where the selective population had a probability of being in either a 'yes' state or in a state of spontaneous firing ('no' state), that is, in this region both states are stable. This region of genuine bistability is one of the main ingredients in our model. The bistability is essential for having (for a given specific external input λ) two possible responses, namely 'detection' or 'no detection', each one corresponding to the two possible stable states. This, together with the noise, would enable a probabilistic behavior. Note that the model shows bistable behavior only when the external input is applied to the MPC network, which is when the decision is prepared. During the following delay period, the system is no longer bistable but the decision was already internally made.

The solution derived at the mean field level holds only for the steady state of the network. To get the information about how the system evolves to a steady state and with which probability it goes to the different possible bistable steady states (i.e. performance), the full spiking network simulations must be run. We can do this by using the parameters found at the mean field level within spiking-level simulations, because these parameters have been derived consistently from the integrate-and-fire level [27]. These spiking-level simulations give us the statistical variations that we are interested in and that we can compare with the experiments. On each trial, statistical fluctuations influence the outcome that is reached. Thus, noise contributed by the probabilistic spiking times of neurons plays a crucial and advantageous part in brain function. Spiking noise is a important contribution to the outcome that is reached, in that this noise is a factor in a

network with a finite number of neurons. In fact, this noise results from 'coherent' fluctuations into the finite-size system [28,29].

Figure 3 shows the probability that the model makes a correct 'yes' response as a function of the sensory signal (λ). In each case, there is a function in which the probability of making a 'yes' response increases with the sensory input (λ), emulating the behavior of monkeys detecting a vibrotactile stimulus [5]. The firing rate of the neurons involved in selection (the MPC neurons), however, showed a different function in which the mean firing rate was approximately constant across different input values (λ), at least beyond a certain level, as reflected in the experimental results. Thus, the model is consistent with the neuronal and behavioral experimental results of Lafuente and Romo [5,6] shown in the previous section.

To stress more explicitly the functional role of noise in this system, one can establish a direct link between neuronal variability and probabilistic behavior. It has been shown that the dynamics of bistable models can be reduced

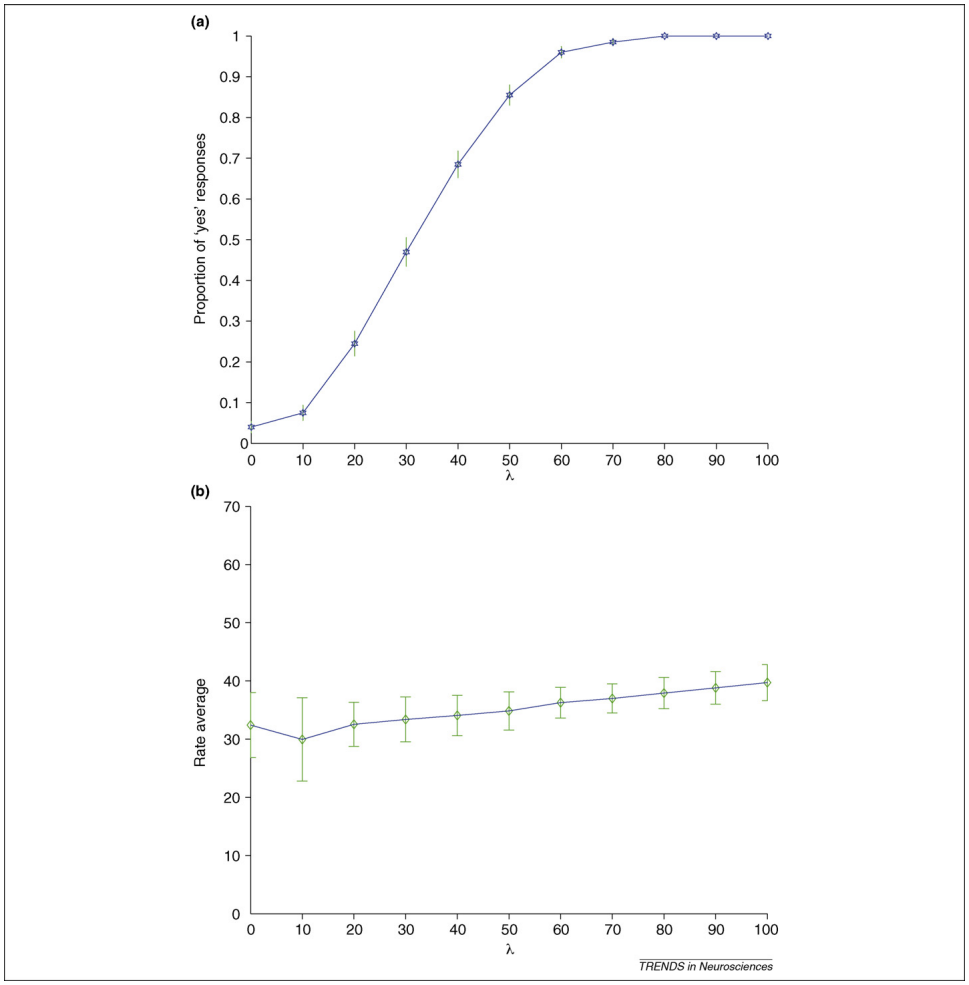

Figure 3. Simulated results plotting the detection curves resulting from 200 trials (overall performance) and the mean rate activity of hit trials at a function of the input strength λ for the MPC neurons for the experimental design of de Lafuente and Romo [5]. **(a)** Probability of a 'yes' response (hit). **(b)** Mean firing-rate activity of neurons in the 'yes' population. The simulations of the nonstationary and probabilistic behavior of the neurodynamical activity were performed by a full spiking and synaptic simulation of the network.

to a one-dimensional diffusion equation typically used to describe the behavioral level [19]. In diffusion models it is assumed that the information that drives the decision process (in this case a perceptual decision) is integrated continuously over time until a decision boundary is reached. Given the success of diffusion models in explaining behavioral data, it seems likely that perceptual decision processes in the nervous system indeed rely on a similar accumulation of evidence. This analysis establishes a link between neuronal and behavioral models of detection. It has been shown that the dynamics of a bistable neuronal model, such as the one analyzed earlier, can be captured in a noise-driven amplitude equation given by the normal form for a saddle-node bifurcation (D. Marti, PhD thesis. Universitat Pompeu Fabra, Barcelona, Spain, 2008). This reduced-amplitude normal form[†] can be derived analytically from the original neuronal dynamics [30]. The main idea is that the dynamics close to the bifurcation point (between bistable and single stable steady states; in the stimulus intensity λ-axis, we call this bifurcation point λ_{bif}) are slow and confined to a center manifold. The reduced amplitude equation corresponds to a nonlinear diffusion equation, which describes properly the original neuronal dynamics. More specifically, the reduced one-dimensional diffusion equation describes the motion of a noise-driven over-damped particle in a potential where $\mu/(\lambda - \lambda_{bif})$ and $a > 0$.

$$V(x) = -\mu x - \frac{ax^3}{3} \qquad \text{[Equation 1]}$$

Figure 4 shows this potential for different values of μ around the bifurcation point λ_{bif}. Thus, the probability of perceptual detection can be seen as the probability of escaping from the lower-rate branch of this potential function owing to the underlying fluctuations within a certain time after the onset of the stimulus. The boundary is naturally given by the peak of the right hill. Note that this potential is not bistable but is only describing locally at the bifurcation point (of bistability), the escaping dynamics from the spontaneous state, which is enough for solving the detection problem.

A second different bistable network model called 'competing yes–no neurons' (CYNN) was also studied [26]. In the CYNN model, there were two competing populations of excitatory neurons, one corresponding to a 'yes' response and the other to a 'no' response. The 'no' response was modeled as a constant bias coming into the 'no' units supporting that response. Both models (NCYN and CYNN) are consistent with the existing single-cell recordings, but they involve different types of bistable decision states and, consequently, different types of computation and neurodynamics. By analyzing the temporal evolution of the firing-rate activity of neurons on trials associated with the two different behavioral responses, evidence was produced in favor of the CYNN model [26]. Specifically, the 'no' responses in the models were further examined [26]. In the NCYN model, the 'yes' population maintained a spontaneous rate of firing on trials with no perceived signal. By contrast, in the CYNN model, the 'yes' population is pushed into a low rate of firing by the competitive rise in the 'no' population. Strikingly, this conformed to the experimentally observed activity pattern in neurons in the MPC. The work demonstrates that such models can separate out stimulus-dependent firing from decision making and it does this in a probabilistic manner, matching (in this case) the behavioral performance of monkeys. The way that activity moves to a decision boundary, and the interplay between decisions (the competition between units for 'yes' and 'no'), is crucial for understanding the operation of the system.

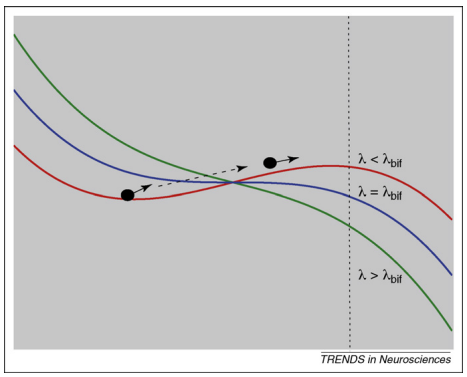

Figure 4. Energy landscape of the analytically reduced one-dimensional nonlinear diffusion equation for the neuronal dynamics computing perceptual detection in the vicinity of the bifurcation point. Three different values around the bifurcation point λ_{bif} are plotted. For values of the intensity of the stimulus $\lambda < \lambda_{bif}$, the energy landscape shows a low-activity valley on the left and a hill on the right. A perceptual detection corresponds, in this case, to the noise-driven escape of the low-activity valley by jumping the right barrier. In fact, the vertical dashed line corresponds to the boundary of the diffusion process, here, naturally given by the neuronal landscape. For increasing values of λ the valley and the hill disappear, resulting in an increase of the performance.

Discussion

Experimental neuronal and behavioral correlates of perceptual detection indicate an underlying computation that is given by a noise-driven transition in a multistable neurodynamical system. Furthermore, this mechanism resembles a decision-making-like cognitive operation [31]. Recently, theoretical and behavioral studies have shed light on the neural mechanisms underlying decision making. At the behavioral level, linear diffusion models describe a wide range of experimental results [19]. In particular, diffusion models are well suited for fitting perceptual performance and choice reaction time. Diffusion models postulate that the information driving the decision process is accumulated continuously over time until a decision boundary is reached. More specifically, the information from a stimulus (the sensory evidence) is represented in a diffusion equation by the mean drift rate of the random variable. This random variable is accumulated over time from the starting point toward one or the other boundaries. The escaping through a given boundary

[†] Normal forms are the canonical equations for bifurcations, that is, they describe the dynamics of the system in a much simpler form, at least for the specific parameters where a qualitative change in the dynamics of the system is observed. Strictly speaking, normal forms are valid only at the bifurcation points, although they catch the main features of the dynamical behavior even far from the bifurcation point [30]. See also Ref. [41] for a formal treatment of normal forms.

corresponds to making a specific decision. A key feature of diffusion models is the consideration of randomness due to noisy fluctuations of the path reflecting the accumulation of sensory evidence. These fluctuations enable the explanation of the generation of both correct and error responses. The well-known speed–accuracy tradeoffs are usually reproduced by adjusting the boundaries. Shifting the boundaries apart results in a better performance and slower response reaction times, whereas shifting the boundaries closer produces more errors and faster response times. The astonishing capability of diffusion models to fit behavioral data seems to indicate that some decision-making processes in the nervous system are really computed by a similar mechanism that accumulates sensory evidence [32]. Similar phenomenological models have been proposed in which the drift of the decision variable is proportional to the value of the variable itself [33] (also called the ballistic model in Ref. [34]). Such connectionist model differs from the classical diffusion model in that the drift of the decision variable is proportional to the value of the variable itself (i.e. it can be leaky or repelling). The diffusion, thus, occurs not on a flat landscape but on a curved one, and the effective dynamics is equivalent to an Ornstein-Uhlenbeck process with fixed boundaries. Psychometric measures of performance in addition to reaction times for two alternative forced-choice paradigms can be analytically studied within such phenomenological model frameworks (see, for example, Ref. [35]).

One disadvantage of the phenomenological models discussed here is the difficulty in assigning a biological meaning to the model parameters. Biologically plausible models motivated and constrained by electrophysiological data have been developed in recent years to establish a link between behavior and neuronal activity [11,20,24,25]. These models involve two groups of neurons coupled through mutually inhibitory connections. Each group receives an input proportional to the evidence for the respective alternative, and the inhibition-driven competition leads to one of the groups winning out at the expense of the other. Usually, the dynamics relevant for decision making in these nonlinear networks depend on the stability of the spontaneous activity state (i.e. the state in which no decision has yet been made). If, once the stimulus is presented, the spontaneous state destabilizes, the dynamics rapidly evolve towards one of the two decision states [25]. The model developed in Ref. [20] provides a remarkable qualitative match with behavioral measures of performance and reaction times in addition to certain aspects of neuronal activity. This is not dissimilar to the repelling Ornstein-Uhlenbeck connectionist ballistic model [36].

The biologically plausible models establish a solid foundation for the phenomenological diffusion models. The dynamics of detailed biophysical rate and spike-based models can be reduced to a one-dimensional diffusion model as shown in Ref. [30], which derived a diffusion equation analytically from the original neuronal dynamics. This is possible because the dynamics close to the bifurcation point are slow and confined to a center manifold. The reduced amplitude equation is a nonlinear diffusion equation, which describes the original neuronal dynamics, and enables also the fit of performance and reaction-time data. The macroscopic phenomenological diffusion description is extended (from linear to nonlinear) and, at the same time, is explicitly linked with a biologically realistic implementation. Biologically realistic models complement diffusion models without losing their capabilities to explain behavioral data.

We review here, for perceptual detection, a decision-making scenario that occurs when the spontaneous state does not lose stability but is rather bistable with the decision state (positive detection), hence leading to multi-stability between two possible fixed points. Such multi-stability only occurs if the recurrent excitation within each neuronal group or population is strong enough. In this case, only a sufficiently strong perturbation would drive the system from the stable spontaneous state to the detection state. Thus, in the multi-stable regime, fluctuations (perhaps noise-driven), are essential for decision making. In fact, the large-scale neuronal system can be reduced to a simple diffusion equation corresponding to an escape problem. If circuits exhibiting multi-stability are comprised of large numbers of spiking neurons, the fluctuations, needed to drive the transitions, arise naturally through noisy input and/or disorder in the collective behavior of the network. Within these models, noise is not just a nuisance variable because it has a crucial computational role in decision making.

Of course alternative scenarios are plausible. For example, one can adjust the neuronal model such that the onset of the external sensory signal deforms the energy landscape so that only one highly excited attractor exists (corresponding to a 'yes' response). In this case, within-trial noise variability would not be necessary for computing a response, but between-trial noise would be required to explain the observed probabilistic behavior. Specifically, one has to assume that the external signal that drives the dynamics is stochastic, so that sometimes the new 'yes' attractor state appears and some other times it does not. At the phenomenological level this would correspond to very successful approaches such as LATER (the linear approach to threshold with ergodic rate), which explain behavioral variability in terms of between-trial noise (implemented as stochastic system parameters) [37]. In our neuronal model, this would shift the problem of probabilistic detection to the implementation of a between-trial stochastic system parameter (in our case the external sensory signal). The problem is that the explanation of a between-trial stochastic parameter such as the external input is exactly what we are aiming to understand (i.e. variability of neuronal responses that covaries with behavior). In conclusion, at the behavioral label, LATER-like models assuming between-trial noise are plausible and could explain behavioral data, but, when we try to reconcile this phenomenological level with the neuronal background (model and data), the explanation turns tautological.

This kind of multistable landscape could also serve for further computational purposes. For instance, a model has been proposed with multistable states for maintaining a memory of the perceptual decision after the stimulus has been removed [25]. Another application is to bistable perception and binocular rivalry. Perceptions can change

'spontaneously' from one to another interpretation of the world, even when the visual input is constant; a good example is the Necker cube, in which visual perception flips occasionally to make a different edge of the cube seem nearer to the observer [38]. It has also been hypothesized that the switching between these multistable states is due, in part, to the statistical fluctuations in the network because of the Poisson-like spike firing that is a form of noise in the system [39,40].

In conclusion, neuronal fluctuations can be an advantage for brain processing because they lead to probabilistic behavior that is advantageous in decision making, by preventing deadlock, and is important in signal detectability. We have shown how computations can be performed through stochastic dynamical effects, including the role of noise in enabling probabilistic jumping across barriers in the energy landscape describing the flow of the dynamics in attractor networks.

Acknowledgements

G.D. was supported by the European Union, grant EC005–024 (Specific Targeted Research Project [STREP] 'Decisions in Motion'; www.decisionsinmotion.org), by the Spanish Research Project BFU2007–61710 and CONSOLIDER CSD2007–00012. R.R. was supported by an International Scholars Award from the Howard Hughes Medical Institute (www.hhmi.org) and by grants of the Direccion General del Personal Academico de la Universidad Nacional Autonoma de Mexico and the Consejo Nacional de Ciencia y Tecnologia (www.conacyt.mx).

References

1 Fechner, G. (1860) *Elemente der Psychophysik,* Breitkopf und Hrtel.(reprinted, Thoemmes Press, 1999)
2 Gold, J.I. and Shadlen, M.N. (2007) The neural basis of decision making. *Annu. Rev. Neurosci.* 30, 535–574
3 Romo, R. and Salinas, E. (2003) Flutter discrimination: neural codes, perception, memory and decision making. *Nat. Rev. Neurosci.* 4, 203–218
4 Glimcher, P.W. (2003) The neurobiology of visual-saccadic decision making. *Annu. Rev. Neurosci.* 26, 133–179
5 de Lafuente, V. and Romo, R. (2005) Neuronal correlates of subjective sensory experience. *Nat. Neurosci.* 8, 1698–1703
6 de Lafuente, V. and Romo, R. (2006) Neural correlates of subjective sensory experience gradually builds up across cortical areas. *Proc. Natl. Acad. Sci. U. S. A.* 103, 14266–14271
7 Shulman, G.L. *et al.* (2001) Multiple neural correlates of detection in the human brain. *Proc. Natl. Acad. Sci. U. S. A.* 98, 313–318
8 Schall, J.D. (2001) Neural basis of deciding, choosing and acting. *Nat. Rev. Neurosci.* 2, 33–42
9 Quiroga, R.Q. *et al.* (2008) Human single neuron responses at the threshold of conscious recognition. *Proc. Natl. Acad. Sci. U. S. A.* 105, 3599–3604
10 Heekeren, H.R. *et al.* (2008) The neural systems that mediate human perceptual decision making. *Nat. Rev. Neurosci.* 9, 467–479
11 Brody, C.D. *et al.* (2003) Basic mechanisms for graded persistent activity: discrete attractors, continuous attractors, and dynamic representations. *Curr. Opin. Neurobiol.* 13, 204–211
12 Ermentrout, G. (1998) Neural networks as spatio-temporal pattern-forming systems. *Rep. Prog. Phys.* 61, 353–430
13 Felleman, D.J. and Van Essen, D.C. (1991) Distributed hierarchical processing in the primate cerebral cortex. *Cereb. Cortex* 1, 1–47
14 Roelfsema, P.R. *et al.* (1998) Object-based attention in the primary visual cortex of the macaque monkey. *Nature* 395, 376–381
15 Rolls, E.T. and Deco, G. (2002) *Computational Neuroscience of Vision,* Oxford University Press
16 Deco, G. and Rolls, E. (2005) Neurodynamics of biased competition and cooperation for attention: a model with spiking neurons. *J. Neurophysiol.* 94, 295–313
17 Brunel, N. and Wang, X.J. (2001) Effects of neuromodulation in a cortical network model of object working memory dominated by recurrent inhibition. *J. Comput. Neurosci.* 11, 63–85
18 Brunel, N. and Amit, D. (1997) Model of global spontaneous activity and local structured delay activity during delay periods in the cerebral cortex. *Cereb. Cortex* 7, 237–252
19 Smith, P.L. and Ratcliff, R. (2004) Psychology and neurobiology of simple decisions. *Trends Neurosci.* 27, 161–168
20 Wang, X.J. (2002) Probabilistic decision making by slow reverberation in cortical circuit. *Neuron* 36, 955–968
21 Ermentrout, G.B. *et al.* (2008) Reliability, synchrony and noise. *Trends Neurosci.* 31, 428–434
22 Faisal, A.A. *et al.* (2008) Noise in the nervous system. *Nat. Rev. Neurosci.* 9, 292–303
23 Hernandez, A. *et al.* (2002) Temporal evolution of a decision-making process in medial premotor cortex. *Neuron* 33, 959–972
24 Machens, C.K. *et al.* (2005) Flexible control of mutual inhibition: a neural model of two-interval discrimination. *Science* 307, 1121–1124
25 Wong, K.F. and Wang, X.J. (2006) A recurrent network mechanism of time integration in perceptual decisions. *J. Neurosci.* 26, 1314–1328
26 Deco, G. *et al.* (2007) Perceptual detection as a dynamical bistability phenomenon: a neurocomputational correlate of sensation. *Proc. Natl. Acad. Sci. U. S. A.* 104, 20073–20077
27 Deco, G. *et al.* (2008) The dynamic brain: from spiking neurons to neural masses and cortical fields. *PLOS Comput. Biol.* 4, e1000092s
28 Mattia, M. and Del Giudice, P. (2004) Finite-size dynamics of inhibitory and excitatory interacting spiking neurons. *Phys. Rev. E Stat. Nonlin. Soft Matter Phys.* 70, 052903
29 Deco, G. and Rolls, E.T. (2003) Attention and working memory: a dynamical model of neuronal activity in the prefrontal cortex. *Eur. J. Neurosci.* 18, 2374–2390
30 Roxin, A. and Ledberg, A. (2008) Neurobiological models of two-choice decision making can be reduced to a one-dimensional nonlinear diffusion equation. *PLOS Comput. Biol.* 4, e1000046
31 Deco, G. *et al.* (2007) Weber's law in decision-making: integrating behavioral data in humans with a neurophysiological model. *J. Neurosci.* 27, 11192–11200
32 Gold, J.I. and Shadlen, M.N. (2002) Banburismus and the brain: decoding the relationship between sensory stimuli, decisions, and reward. *Neuron* 36, 299–308
33 Usher, M. and McClelland, J. (2001) On the time course of perceptual choice: the leaky competing accumulator model. *Psychol. Rev.* 108, 550–592
34 Glimcher, P.W. (2005) Indeterminacy in brain and behavior. *Annu. Rev. Psychol.* 56, 25–56
35 Bogacz, R. *et al.* (2006) The physics of optimal decision making: a formal analysis of models of performance in two-alternative forced choice tasks. *Psychol. Rev.* 113, 700–765
36 Brown, S. and Heathcote, A. (2005) A ballistic model of choice response time. *Psychol. Rev.* 112, 117–128
37 Carpenter, R.H. (2004) Contrast, probability, and saccadic latency: evidence for independence of detection and decision. *Curr. Biol.* 14, 1576–1580
38 Leopold, D.A. and Logothetis, N.K. (1999) Multistable phenomena: changing views in perception. *Trends Cogn. Sci.* 3, 254–264
39 Moreno-Bote, R. *et al.* (2007) Noise-induced alternations in an attractor network model of perceptual bistability. *J. Neurophysiol.* 98, 1125–1139
40 Shpiro, A. *et al.* (2007) Dynamical characteristics common to neuronal competition models. *J. Neurophysiol.* 97, 462–473
41 Wiggins, S. (2003) *Introduction to Applied Nonlinear Dynamical Systems and Chaos,* Springer

Modeling of Large-Scale Dynamics in the Primary Visual Cortex

Louis Tao

An Overview

In these notes I review a particular approach to the large-scale computational modeling of the mammalian primary visual cortex (V1). The main objectives of this modeling are to (i) capture groups of experimentally observed phenomena in a single theoretical model of cortical circuitry, and (ii) identify the physiological mechanisms underlying the model dynamics. These goals are achieved by building parsimonious models based on minimal, yet sufficient, sets of anatomical and physiological assumptions and constraints. This work has identified a particular operating state of the cortical model which I believe to underlie how V1 responds to visual stimulation.

This state is characterized by (i) high total conductance, (ii) strong cortical inhibition, (iii) large synaptic fluctuations, (iv) an important role of NMDA conductance in the orientation-specific, long-range interactions, and (v) a high degree of correlation between the neuronal membrane potentials, NMDA-type conductances, and firing rates. Tuning our model to this operating state, we have studied and identified network mechanisms underlying cortical phenomena such including (i) neuronal orientation tuning in V1 [123], (ii) spatiotemporal patterns of spontaneous cortical activity [20], and (iii) cortical activity patterns induced by the Hikosaka line-motion illusion stimulus paradigm [94].

Due to the time limitations of this CRM short course, in these notes I will focus on the first 3 characterizations of what I believe is the visual cortical operating point. I will review some of the relevant neurophysiological background in Chap. 1 and modeling background in Chap. 2. I will highlight the cortical mechanisms that underlies the so-called Simple and Complex cell populations in Chap. 3. The work that led to [124] showed that there were network nonlinearity we had not yet fully appreciated or understood: the strong cortico-cortical excitation that was needed to produce Complex cell-type behavior often led to runaway amplification. The elucidation of this instability led to the identification of a particular bifurcation in the model network system and showed the importance of synaptic fluctuations in maintaining stability in the presence of strong recurrent excitation. In conjunction with strong cortical inhibition, we were able to identify a possible network mechanism underlying orientation selectivity. I review this work in Chap. 4 before turning to theoretical developments in Chap. 5 and concluding remarks in Chap. 6.

In this modeling endeavor, I have had the good fortune to work with David Cai, Gregor Kovačič, David McLaughlin, Aaditya Rangan, Robert Shapley and Michael Shelley, each of whom has moved forward the work I am about to describe to you. I would

also like to thank the Centre de Recerca Matemàtica for its hospitality, and especially, Professors José Antonio Carrillo, Àngel Calsina and Antoni Gullamón for kindly inviting me to be a part of the Research Programme on Mathematical Biology: Modelling and Differential Equations. This work was supported in part by the NSF grant DMS-0506257 and by the Swartz Foundation.

Chapter 1

Physiological Background

Located in the back of the skull, the mammalian primary visual cortex (V1) is a thin sheath of densely packed and highly interconnected neuron. Along the "visual pathway", *Retina* $\rightarrow$ *Thalamus (LGN)* $\rightarrow$ *V1* $\rightarrow$ *And Beyond*, it is in V1 where neuronal responses are first simultaneously selective to elementary features of visual scenes, including a pattern's orientation. For instance, the *orientation tuning* property is the selective response of a *single* neuron to some orientations of a simple visual pattern (say a bar or grating), but not to other orientations [49].

The primary visual cortex is several cm^2 in lateral area and 1-2 mm in thickness. It has a complex, laminar structure (layers 1, 2/3, 4*B*, 4$C\alpha$, 4$C\beta$, 5, and 6, labeled from the cortical surface inwards). Each layer is anatomically distinct, containing excitatory and inhibitory neurons with dense lateral connectivity, augmented by specific feed-forward and feed-back projections between different layers. Visual input first arrives at V1 via axons from the neurons in the Lateral Geniculate Nucleus (LGN, in the thalamus) primarily into the layers 4$C\alpha$ ("magno pathway") and β ("parvo pathway"). These inputs are excitatory only.

Neurons in V1 are roughly divided into "simple" and "complex" cells. This division dates back to [49]. The responses of simple cells to visual stimuli tend to be approximately linear, while those of complex cells tend to be nonlinear. For instance, if the stimulus is a drifting grating, the spiking rate of a simple cell will be modulated at the frequency at which the grating's peaks and troughs pass through the cell's receptive field; the spiking rate of a complex cell will change with the presentation of the stimulus, but then stay basically constant in time for duration of the stimulus presentation. For a standing, contrast-reversing grating, simple-cell firing rates are sensitive to its spatial phase and modulate at the stimulus frequency, while complex-cells are spatial-phase insensitive and modulate at double the stimulus frequency [86, 87].

The long-standing, theoretical model of [49] proposes that simple cells receive LGN input and pool their output to drive complex cells. (Evidence for excitatory connections from simple to complex cells can be found in [125].) Phase sensitivity is lost in this non-specific spatial pooling. However, most V1 neurons are neither wholly simple nor

wholly complex [99]. Experiments show that complex cells receive inputs not just from simple cells, but also receive strong input from other complex cells [125] and from the LGN [37, 48, 114]. Furthermore, some complex cells can be excited without strongly exciting simple cells [44, 72, 73, 80, 85]. Therefore, an alternative hypothesis is that the amount of excitatory LGN input varies from one V1 neuron to the next (indirect evidence for this is given in [4, 97, 122]), and is compensated by the amount of cortical excitation, so that each V1 neuron receives roughly the same amount of excitation [124], as suggested by cortical development theories [81, 82] and experiments [102, 103]. We adopt this hypothesis in our model, as described below. We note that simple cell properties were recovered in a model of V1 neurons that all received equal amount of LGN drive [131]. In this model network, strong cortical inhibition cancels the nonlinearity in the LGN drive to produce the linear response properties of simple cells.

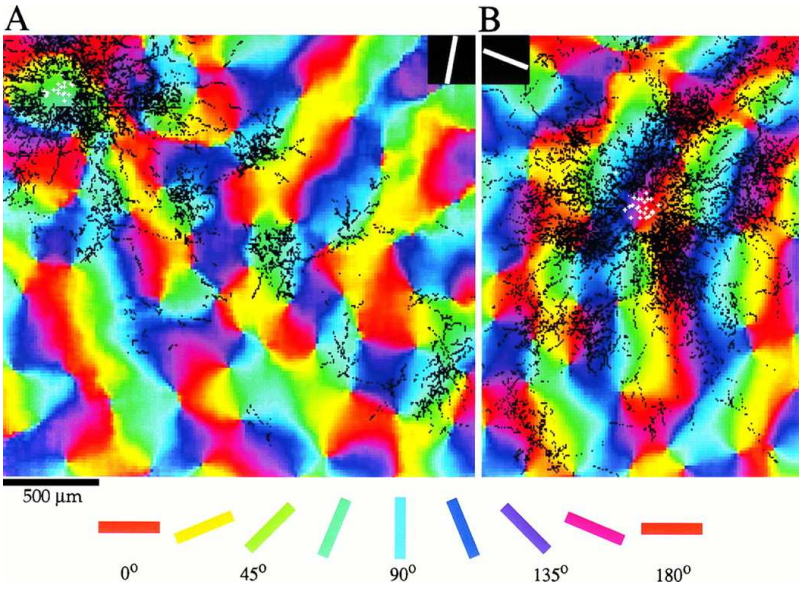

Figure 1.1: Optical imaging of orientation hypercolumns and long range connections: Fig. 4 of [16] showing the map of orientation preference in color and the distribution of connections in black. The orientation preference is color-coded to the oriented color bars below (e.g., the areas colored orange prefer gratings oriented at 0°). The white symbols indicate the sites of biocytin injection. Local to the injection site, the distribution of connectivities is nearly isotropic. However, at distances larger than a hypercolumn, the connections are between neurons that have similar orientation preferences.

Optical imaging experiments [12–14] reveal orientation preference as organized into millimeter-scale "orientation hypercolumns" that tile the cortical surface, with ori-

entation preference laid out in spokes emanating from the so-called "pinwheel centers." Orientation preference appears to be well correlated even between single pairs of nearby cortical neurons, whereas preferred spatial phase does not, indicating the possibility that spatial phase preference may be mapped across V1 in a disordered fashion [34]. The exact nature of the spatial frequency preference distribution across V1 is still in dispute: Interpretations of experiments have ranged from spatial domains with only high or low spatial frequency preference [52] to continuous pinwheel patterns [36]; however, most recent work seems to indicate that the spatial distribution is most likely to be disordered [53, 84, 115].

Anatomical, electrophysiological and optical imaging studies suggest that lateral connectivity shows different types of organization on different spatial and temporal scales. At the local hypercolumn scales ($< 500\mu$m), the pattern of connectivity appears to be isotropic, with monosynaptic inhibition at or below the range of excitation [24,25,39,67]. The excitatory short-range connections appear to be mostly mediated by the fast, AMPA, neurotransmitter [100] (with time-scale $\sim$3 ms [62]), while the inhibitory connections are mediated by $GABA_A$ (with time-scale $\sim$7 ms [62]).

At longer lengthscales, $\sim$1-5 mm, the intralaminar and reciprocal lateral connections [6–8, 16, 68, 112] (also referred to as the horizontal connections) in V1 are much less isotropic. These horizontal connections emanate only from excitatory neurons, and terminate on both excitatory ($\sim$75%) and inhibitory ($\sim$25%) neurons [59,75,76]. They are only strong enough to elicit subthreshold responses in their postsynaptic neurons [47, 136].

Long-range projections have been found to connect sites of like preferences, such as orientation preference [58, 69], ocular dominance and cytochrome oxydase blobs [137], and direction preference [101]. The shapes of the cortical regions covered by horizontal projections of a given neuron differ from species to species, ranging from just barely elongated along the retinotopic axis in macaque [137] and new world monkeys [112] (anisotropy ratio $\sim$1.5–1.8) to highly elongated in the tree shrew [16] (whose anisotropy ratio is $\sim$4).

In contrast to short-range connections, long-range connections in V1 appear to be mediated by both AMPA and NMDA. In particular, *in vitro* stimulation of white matter shows that firing by layer 3 pyramidal neurons may be driven and synchronized by long-range, horizontal connections, mediated in part by NMDA [100]. Additionally, long-range horizontal inputs to cells in layers 2 and 3 can sum nonlinearly [136]. This strongly indicates NMDA involvement in the long-range connections, since the NMDA channel is voltage dependent [32]. Moreover, visual response in the superficial V1 layers 1-3 has been observed to be in part mediated by NMDA receptors, both in cats [104] and the macaque [105].

The precise role of the long-range horizontal connections in V1 is as yet unknown; however, it appears that they contribute to spatial summation of stimuli and "contextual" effects from outside of a given neuron's classical receptive field [8]. They may also contribute to synchronous firing of cells with similar orientation preferences, especially when those cells are separated by more than 0.4 mm [41, 63] (see also [20]), and the synchronization of fast, γ-band (25–90Hz), oscillations present in the collective firing rates of neuronal populations over distances of $\sim$5 mm [71, 113]. Simulations using our

model [20, 94] suggest that particularly striking examples of the long-range connection contributions may be in millimeter-scale spatiotemporal patterns of spontaneous cortical activity [57, 128] and activity induced by the Hikosaka-motion-illusion stimulus [54], which have been observed in experiments using voltage-sensitive dyes.

In addition to the diverse spatial scales, the neuronal network in V1 also operates within a large range of temporal scales. The manifestations of selectivities such as orientation tuning are actually strongly dynamical, as revealed by reverse-time correlation experiments [98, 135], which reveal some of the time-scales operating during V1 processing. These are: the LGN response time $\tau_{lgn} = \mathcal{O}(10^2)$ ms, reflecting the concatenation of retinal and LGN processing of visual stimulation; the various time-scales of synaptically mediated currents $\tau_{syn} = \mathcal{O}$(3-200 ms), as described above; and $\tau_G = C/[G]$, where C is cellular capacitance and $[G]$ a characteristic size of total synaptic conductances. This τ_G is the time-scale of response of a single neuron, but is a property of network activity. The higher the network activity, the shorter the τ_G, which is usually about $\mathcal{O}$(2-5 ms). Intracellular measurements have shown that under visual stimulation, cellular conductances can become large, increasing by factors of two or three and dominated by (cortico-cortical) inhibition [15, 35, 65, 92, 108]

Some prior theoretical studies of cortical effects induced by short- and long-range horizontal connections in V1 include (but are by no means limited to) the following: An I&F computational model with an idealized architecture [118]; The mainly analytical studies of [17, 18, 107] addressing the role of long-range connections on stationary cortical pattern formation and stability; The role of recurrent excitation in a network model of [29]; A large-scale computational model of neuronal orientation tuning in V1 [127]; A detailed large-scale, highly-realistic, local computational model of neurons in 4 orientation hypercolumns in the input layer $4C\alpha$ of macaque V1 [77, 111, 131], which included only short-range connections. Orientation selectivity of cells in this model was shown to be greatly enhanced by recurrent interactions [77]. In [124], the model was extended to include heterogeneity in LGN input. It is to this last model we first turn.

Chapter 2

Modeling Background

In recent work [77, 123, 124, 131], my collaborators and I have developed a computational model of a small, local patch of layer $4C\alpha$, which is the primary input layer in macaque V1. Here, I describe the mathematical and biological detail it incorporates.

The cortical model contains four orientation hypercolumns with pinwheel centers within a 1 mm^2 patch of V1 4Cα. For simplicity, the boundary conditions are taken to be periodic. Individual neurons are modeled as conductance-based, linear I&F point neurons [66] (i.e., all spatial effects within a cell are neglected). Between "spike times," the intracellular potentials v^j are described by the linear differential equation:

$$\frac{dv_P^j}{dt} = -g_L\ \left(v_P^j - V_R\right) - g_{PE}^j(t)\ \left(v_P^j - V_E\right) - g_{PI}^j(t)\left(v_P^j - V_I\right),\ \ P = E, I. \tag{2.1}$$

The m^{th} spike time, t_m^j, of the j^{th} model neuron, is determined by $v_P^j(t_m^{j-}) = V_T;\ v_P^j(t_m^j + \tau_{ref}) = V_R$ where τ_{ref} is an absolute refractory period. Here the membrane potentials of the excitatory (E) (inhibitory (I)) neurons are denoted by v_E^j (v_I^j) where the superscript j indexes the spatial location of the neuron within the network. g_L, g_{PE}, and g_{PI} are the leak, excitatory, and inhibitory conductances, respectively. The various synaptic potentials are ordered, $V_I < V_L < V_T < V_E$, and therefore, the term $-g_E^j(t)\left[v^j - V_E\right]$ drives the voltage up and is "excitatory," while $-g_I^j(t)\left[v^j - V_I\right]$ drives the voltage down and is "inhibitory." We take $\tau_{ref} = 3$ ms (1 ms) for excitatory (inhibitory) neurons.

The **time-dependent** postsynaptic conductances (PSCs) arise due to visual stimulation and from the cortical network activity of the excitatory and inhibitory populations, and have the general form

$$\begin{aligned} g_{PE}^j(t) &= F_{PE}(t) + [(1-\lambda^j)S_{PE} + S_{PE}^0]\sum_k a_{j,k}\sum_l p_{kl}^j G_E(t - t_l^k), \\ g_{PI}^j(t) &= F_{PI}(t) + S_{PI}\sum_k b_{j,k}\sum_l p_{kl}^j G_I(t - t_l^k), \end{aligned} \tag{2.2}$$

where $F_{PE}(t) = \lambda^j g_{lgn}^j(t)$ (the conductance $g_{lgn}^j(t)$ denotes the *feedforward*, excitatory

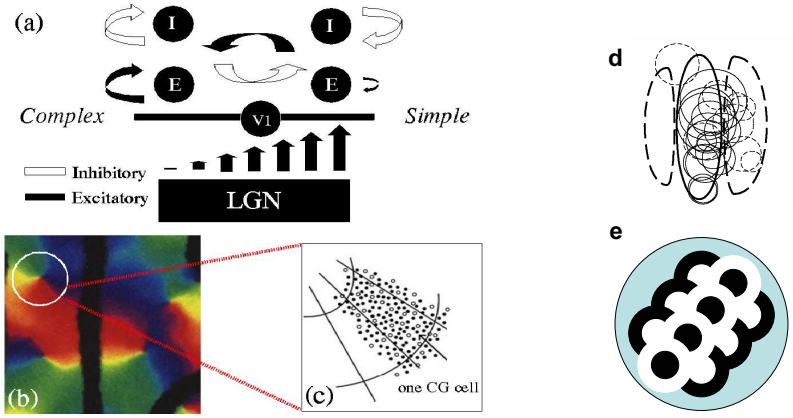

Figure 2.1: Model description. (a) A schematic of the large-scale model network, indicating the mechanisms by which Simple and Complex neuronal responses are created: Simple cells by strong LGN input and strong cortical inhibition, together with phase randomization (not shown but described in [124]); and Complex cells by weak LGN input and strong cortical excitation. (b) Optical imaging of the orientation preference in a single mm^2 of layer 2/3 of macaque V1, containing 4 pinwheel centers [12, 13]. The cells on the white circle are described by a ring model. (c) A schematic of one coarse-grained (CG) cell located, for example, on a small section of a ring. (d) (taken from [96]) Circles indicate receptive fields of LGN cells. The thick solid (dashed) lines indicate the on (off) portion of the receptive field of a V1 Simple cell receiving afferents from recorded LGN cells. This is evidence for convergent LGN input creating Gabor-like V1 receptive fields. (e) A schematic of how a V1 receptive field can be built from excitatory inputs from on- and off-centered LGN cells.

forcing from the LGN), $F_{PI}(t) = c_{inh} \sum_i G_I \left(t - s_I^j \right)$ is a stimulus-independent inhibition modeled by homogeneous Poisson spike trains. Since the LGN does not generate inhibitory PSC in V1 cells, inhibition arises from the LGN driving inhibitory neurons (via g_{EI}^j) and this is sometimes referred to as a *"feedforward" inhibition*.

2.1 Model of the LGN input

The LGN drive, $g_{lgn}^j(t)$, of the I&F model (2.1-2.2), is modeled as time-dependent Poisson spike trains whose rate is given by the sum of linear spatio-temporal filters. Response properties of individual LGN cells are estimated from experimental studies [50, 64, 132]. Each LGN neuron shows no orientation selectivity and a "center-surround" receptive field. There are two types of such neurons: on-center and off-center. For an on-center

neuron, illuminating the center of its receptive field increases its firing rate, while illuminating a surrounding annulus decreases it. For an off-center neuron, the respective responses are reversed. The temporal response curve of an LGN neuron increases to a maximum at about $40\,ms$, to a sub-background response with a minimum at about $60\,ms$, has zero overall integral (which holds for LGN cells in the magno pathway), and is taken from [11, 43].

An individual V1 neuron "sees" the world through the pooling of about $N_{LGN} \approx 20$ LGN cells [122]. Thus the LGN input into a single V1 neuron is represented by a sum of Poisson spike trains, with total rate given by

$$\nu_{lgn}^{j}(t) = \sum_{m=1}^{N_{LGN}^{j}} \left\{ R_B \pm C\left[\int_{R^2} d\mathbf{X} K_{lgn}(|\mathbf{X}-\mathbf{X}_m|) \int_{-\infty}^{t} ds\, G_{lgn}(s-t) I(\mathbf{X},s) \right] \right\}^{+}. \quad (2.3)$$

Here R_B is the background LGN firing rate (about 20 Hz). The on- and off-centered LGN cells at $\mathbf{X}_m$ are arrayed in the Gabor-like pattern to be described below [96, 97], tilted by a preferred angle Θ and a spatial phase Φ. The $\pm$-signs model the processing of on-center and off-center neurons. The symbol $\{\cdot\}^{+}$ stands for $A^{+} = \max\{A, 0\}$ (i.e., rate rectification). The function $C[\cdot]$ describes LGN contrast saturation at high contrasts [55, 56, 109]. The exact forms of the LGN kernels K_{lgn} and G_{lgn} are given in [124, 131]. In particular, to model the "center-surround" receptive fields of the LGN neurons, K_{lgn} is taken to be a difference of two Gaussians, with parameters as in [117, 127]. The kernel G_{lgn} is taken directly from [11, 43]. Retinotopy can be ignored in this model and should be unimportant for questions of orientation arising in the local, sub-hypercolumn circuit, but will need to be addressed in any extended modeling. In practice, I will focus on two types of visual stimuli:

1. Drifting grating: $I(\mathbf{X},t) = I_0[1 + \varepsilon \sin(\mathbf{k}\cdot\mathbf{X} - \omega t - \phi)]$, with $\mathbf{k} = k(\cos\theta, \sin\theta)$
2. Contrast reversal: $I(\mathbf{X},t) = I_0[1 + \varepsilon \sin(\mathbf{k}\cdot\mathbf{X} - \phi)\sin\omega t]$,

where I_0 is the average intensity, $\varepsilon \leq 1$ is the stimulus contrast, $\mathbf{k} = k(cos\theta, sin\theta)$ is parameterized by spatial frequency k and orientation θ, ω is the temporal frequency and ϕ is the spatial phase.

This feedforward LGN drive is highly structured: The receptive fields of on- and off-centered LGN neurons are segregated into elongated subregions, which together shape the receptive field of the V1 neuron with Gabor-like inputs with preferred angle Θ, preferred spatial frequency k and preferred spatial phase Φ. (See Fig. 2.1 for details.) In this local model of 4 orientation pinwheels, the preferred orientation is built-in to the model by tying the preferred orientation of a single V1 neuron to the neuron's location relative to the pinwheel pattern. To model the spatial phase variations across the cortical surface, the preferred spatial phase of each V1 neuron is distributed randomly from cell to cell, as is consistent with recent experiments [34, 78].

To capture the diversity of feedforward input as seen in experiments, I assume that N_{LGN}^{j}, the number of LGN cells with outputs converging on the j^{th} V1 neuron, is distributed randomly and uniformly between 0 and 30. Furthermore, N_{LGN}^{j} is also distributed

randomly in space. Thus some cortical cells receive significant LGN drive while their neighbors may receive little LGN excitation. Finally, this is combined with the constraint that the total excitatory synaptic drive onto each cell is approximately constant, though divided between LGN and cortico-cortical inputs, as is suggested by theories of cortical development [81] and by recent experiments [102, 103]. Therefore those neurons receiving weak or no LGN drive, receive stronger recurrent excitation. As I describe below, these basic model assumptions naturally lead to a neuronal population response diversity consistent with recent experiments.

2.2 The Structure of Network Coupling

The kernels $a_{j,k}$ and $b_{j,k}$ describe the spatial structure of the cortical coupling and are normalized to have unit sum so that the S_{PE} and S_{PI}'s denote synaptic strengths; we take $S_{EI} = S_{II}$ so that the cortical inhibition is the same for both excitatory and inhibitory neurons. The parameter $\lambda^j \in [0,1]$ in these equations indicates heuristically how the distribution of Simple and Complex cells is set in our models and characterizes the Simple-Complex nature of the j^{th} neuron (with $\lambda^j = 0$ the most Complex, $\lambda^j = 1$ the most Simple, and S^0_{PE} models weak cortical excitatory couplings for Simple cells), by setting the strength of LGN drive relative to the strength of the cortico-cortical excitation. The parameter λ^j is distributed uniformly in $[0,1]$ for our large-scale V1 model (see Fig. 2a).

Individual PSCs are taken to be $\Theta(t)(\tau_d - \tau_r)^{-1}\left[\exp\left(\frac{-t}{\tau_d}\right) - \exp\left(\frac{-t}{\tau_r}\right)\right]$, where Θ is the Heaviside step function. The time constants are $\tau_r = 1, 2, 1$ ms and $\tau_d = 5, 80, 10$ ms for AMPA, NMDA and $GABA_A$, respectively. For excitatory synapses,

$$G_E(t) = (1 - f_N)\, G_{AMPA}(t) + f_N G_{NMDA}(t),$$

where f_N denotes the fractional contribution of NMDA receptors; for inhibitory synapses, $G_I(t) = G_{GABA_A}(t)$. For networks with synaptic failure p^j_{kl} is a Bernoulli random variable chosen to be 1 with probability p for each spike-time; for *sparse* networks, p^j_{kl} is independent of l, is chosen to be 1 with probability p and is fixed for individual realizations of the network model. (Thus, in both types of networks, each neuron is coupled to $N_{eff} = pN$ other neurons statistically.) In Chap. 3, we review work using an *all-to-all* network model, with p^j_{kl} identically equal to 1. In Chap. 4, we discuss a model where the network coupling is sparse and study the effects of intrinsic synaptic fluctuations on the stability of the network dynamics.

Chapter 3

An Egalitarian Network Model

3.1 Simple and Complex Cells

A fundamental classification of neurons in the primary visual cortex (V1) is as Simple or Complex [49]. A Simple cell responds to visual stimulation in an approximately linear fashion. For example, when responding to the temporal modulation of standing grating patterns, Simple cells modulate their firing at the stimulus frequency and are sensitive to its spatial phase (or location). Complex cells are very nonlinear, modulating their firing at twice the stimulus frequency and showing little sensitivity to spatial phase.

Simple and Complex cells may have different tasks in visual perception. Cortical cells must represent spatial properties such as surface brightness and color, and the perceptual spatial organization of a scene that is the basis of form. Simple cells are assumed to be necessary for all of these functions because they are the V1 neurons that are able to respond monotonically to signed edge contrast. Complex cells, being insensitive to spatial phase, cannot provide a cortical representation of signed contrast, but they are sensitive to texture, firing at elevated rates in response to stimuli within their receptive fields.

While long-standing, the Simple/Complex classification is hardly sharp. Recent work by Ringach et al [99] analyzes the extracellular responses of neurons in macaque V1 experiments. They find that many V1 cells are neither completely Simple nor completely Complex, but lie somewhere in between. And while most cells in V1 might be classified as Complex, the cortical layer which receives the bulk of LGN excitation, $4C\alpha$, has Simple and Complex cells in approximately equal proportion. A central assumption of this model is that the strength of LGN excitation varies broadly, so that some cortical cells receive significant LGN drive, while others receive little. This is combined with the constraint that the total excitatory synaptic drive onto each cell is approximately constant, though divided between geniculate and striate sources, as is suggested by theories of cortical development [81,82] and by recent experiments [102]. Simple cells arise in a manner similar to those of the earlier model of [131], as we describe below.

The aim of our modeling is to understand the function of the V1 cortical network

in terms of its network connectivity and dynamics. Thus to be successful, the model must account in a realistic manner for orientation selectivity, response dynamics with a wide range of input stimuli, firing rate patterns in background, as well as during stimulation. In this chapter we focus on the model's performance in spatial summation experiments that have been used to classify neurons as Simple or Complex. We show that this egalitarian model, which combines natural assumptions on the variability of cortical and geniculate drive and what is known about the neuronal architecture of V1, can rationalize many aspects of the available experimental data. The model yields physiologically reasonable Simple and Complex cell responses, both in the rate and the form of spiking. The architecture leads to distinctive predictions of population measures of Simple/Complex responses, which have the qualitative structure seen in recent experimental measurements.

3.2 Modeling Results

In the present chapter, we will review how simple and complex cellular responses arise in a large-scale neuronal network model of an input layer $4C\alpha$ of macaque V1 [124]. The model represents a 1 mm^2 local patch with 4 orientation hypercolumns containing $\sim O(10^4)$ conductance based, integrate-and-fire (I&F) neurons — 75% excitatory and 25% inhibitory. The coupling is **all-to-all**, with local synaptic coupling kernels Gaussian with lengthscales of roughly 0.2 mm. The cortical architecture, the LGN drive, and the cortico-cortical synaptic couplings are described in Chap. 2 and constrained whenever possible by anatomical and physiological measurements [77, 124, 131].

3.2.1 Contrast reversal and spatial phase dependence

"Contrast reversal" is the sinusoidal modulation in time of the contrast of a standing sine-wave pattern. Response to contrast reversal is a critical test of linearity in Simple cells [33, 120]. A simple cell's response depends strongly upon the spatial phase or position of the standing grating pattern relative to the midpoint of the neuron's receptive field, has a large amplitude response at the fundamental driving frequency at one spatial phase (the "preferred-phase"), and very little response at the "orthogonal phase", 90° away from the preferred phase. Response at both of these phases shows little or no generation of the higher temporal harmonics that might be expected for a nonlinear system. On the other hand, nonlinear harmonic distortion products are apparent in the responses of cortical Complex cells [33]: their temporal responses show little sensitivity to spatial phase, and firing modulates at twice the stimulus frequency (i.e., at the 2^{nd} harmonic).

Simple and Complex cell responses, like those seen in experiment, arise in this model cortex. For contrast reversal stimulation, Fig. 3.1a shows a model cell responding like a Simple cell, and Fig. 3.1b shows another cell responding like a Complex cell. These are but two cells taken from a large-scale network simulation with $\sim 4,000$ cells (75% excitatory, 25% inhibitory). Orientation and spatial phase preferences are conferred on cortical cells from the convergence of output from many LGN cells [96], with orientation

preference laid out in pinwheel patterns [12–14, 70], and spatial phase preference varying widely from cortical cell to cortical cell [34].

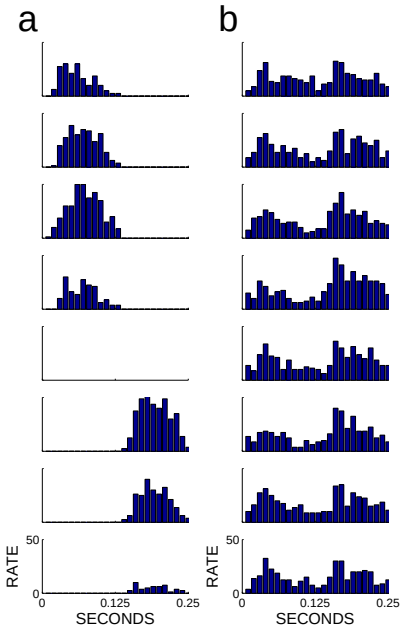

Figure 3.1: Responses of model neurons to contrast reversal stimulation (8 spatial phases, at optimal orientation, and temporal and spatial frequency). (a) and (b) are predicted responses from respectively a Simple and a Complex neuron in the model network. (a) Model Network Simple cell driven at 4 Hz. The spatial phase is defined so that one spatial cycle of the grating pattern is 360°. At 180°, the response is zero. (b) Model Network Complex cell driven at 4 Hz. The response is at the second harmonic and is insensitive to spatial phase. [Reproduced from Ref. [124].]

3.2.2 Trade-off between LGN and cortico-cortical input

Phase insensitivity and frequency doubling are key to how this network produces both Simple and Complex cells. For example, Fig. 3.2b shows that LGN excitation is frequency doubled at the orthogonal phase, yet this strong nonlinearity in the LGN input is not expressed in the spiking of the cell. As explained in [131], if excitation and cortico-cortical inhibition are roughly in balance, phase insensitive cortico-cortical inhibition is sufficient to suppress frequency-doubled firing at the orthogonal phase.

Another structural element is that the number of excitatory, LGN afferents driving a cortical cell is inversely correlated to the number of excitatory cortico-cortical afferents.

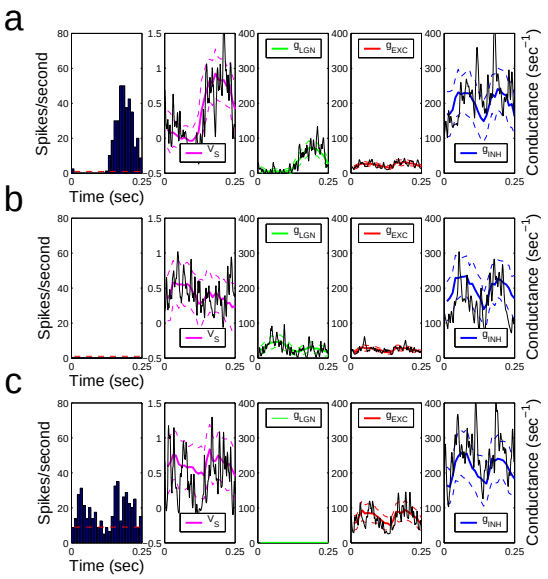

Figure 3.2: Extra- and intracellular responses to 4 Hz contrast reversal. (a) and (b) show the model Simple Cell in Fig. 3.1a responding at its preferred and orthogonal spatial phases. (c) the model Complex Cell in Fig. 3.1b at one of the phases. From left to right: cycle-averaged firing rate (with the spontaneous rate in red dashes); effective reversal potential V_S (magenta); LGN-driven conductance (green); cortico-cortical excitatory conductance (red); cortico-cortical inhibitory conductance (blue). Dotted lines are standard deviations for each of the conductances and for the potential. Thin black lines indicate instantaneous values of conductances and potentials. [Reproduced from Ref. [124].]

That is, the fewer synapses on a cell taken up by the LGN, the more are available to excitatory (presynaptic) neurons in the network. This assumption is based on theories of cortical development in which the number of excitatory synapses is kept constant [81, 82] (recent experiments support this theoretical constraint [102]). The consequences of this assumption are made clear in Fig. 3.3c. For the Complex cell, the lack of LGN excitation is compensated for by a strong, frequency-doubled cortico-cortical excitation, balanced by likewise frequency-doubled inhibition. The firing pattern of the cell is then naturally frequency-doubled, and phase insensitive, as is observed for Complex cells.

3.2.3 Drifting grating responses

Another common visual stimulus used to classify the response properties of cortical neurons is drifting sinusoidal gratings (a traveling, spatially modulated intensity pattern, held at a fixed orientation). For the model Simple and Complex cells of Figs. 3.1 and 3.2,

Fig. 3.3 shows their extra- and intracellular responses to a drifting grating stimulus (8 *Hz* at optimal orientation and spatial frequency). Their extracellular spiking is typical of experimentally observed Simple and Complex cells: The Simple cell follows the temporal modulation of the grating as the grating drifts across its receptive field, whereas the Complex cell shows an elevated, mostly unmodulated firing over the entire duration of the stimulation.

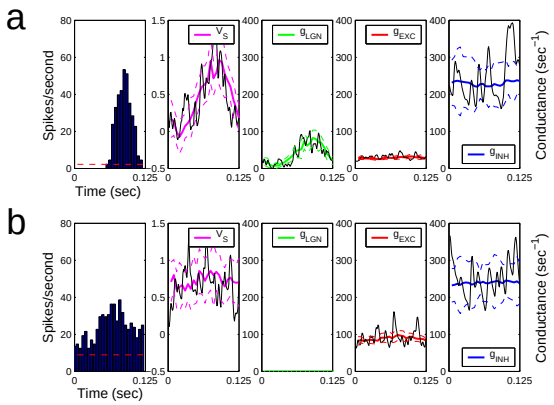

Figure 3.3: Responses to 8 Hz drifting grating at optimal orientation: (a) The model Simple cell in **Fig. 3.1A**. (b) The model Complex cell in Fig. 3.1a. From left to right: cycle-averaged firing rates (spontaneous rates as dashed red lines); effective reversal potential V_S (magenta); LGN-driven conductance (green); cortico-cortical excitatory conductance (red); cortico-cortical inhibitory conductance (blue). The dotted lines are standard deviations for each of the conductances and for the potential. The thin black lines indicate instantaneous values of conductances and potentials. [Reproduced from Ref. [124].]

Examination of LGN and cortico-cortical conductances in Fig. 3.3 accounts for the model's response to drifting gratings. First, the strong LGN excitation into the Simple cell modulates with the stimulus frequency. Different cells receive LGN excitation of similar wave-form, but due to variability in both the number of LGN afferents, and in spatial phase preference, they are diverse in both amplitude and time of peak excitation. For drifting grating stimulation, this yields a bulk forcing to the model that is nearly constant in time and which is manifested as nearly time-invariant cortico-cortical conductances [131]. Thus, for the model Simple cell, both the intracellular V_S and its extracellular firing pattern modulate on the time dependence of its LGN input. Conversely, for the model Complex cell both V_S and the firing pattern are driven by the unmodulated cortico-cortical conductances, and hence show only elevated, unmodulated responses.

3.2.4 Population distributions of modulation ratio

Keeping in mind the structure of the model, it should be clear that these two sample cells, one Simple and one Complex, must sit within a continuum of possible intracellular and extracellular responses. We explore this with a standard characterization of response: Figure 3.4a shows the histogram of *modulation ratio* F_1/F_0 for the cycle-averaged effective reversal potential, V_S, across the whole population of $\sim 3,000$ excitatory cells within the model. The modulation ratio is the ratio of first harmonic amplitude (at the stimulus frequency) to the mean. The distribution of modulation ratio is broad, unimodal and monotonically decreasing, and reflects the broad distribution in number of LGN afferents and the constraint of fixed, total excitation. In recent unpublished work David Ferster and colleagues measured the modulation ratio of the intracellular potential for 168 cells in cat cortex (personal communication; see Fig. 11 of [26] for an analysis on a much smaller set of cat V1 cells). Like our model here, their measurements show also a broad and unimodal distribution of intracellular F1/F0.

Curiously, this unimodality is not preserved in extracellular measures, neither in experiment nor in the model. Fig. 3.4b shows for the model cortex the distribution of modulation ratio of the cycle-averaged firing rate. Following others (e.g. [99, 116]), we use this extracellular F_1/F_0 as a classifier, labeling as Simple those cells with $F_1/F_0 > 1$ (red in the figure), and as Complex those with $F_1/F_0 < 1$ (blue in the figure). Qualitatively similar, both distributions show a bimodal structure peaked near the extremes of the classifier, but with a large proportion of cells having responses that are neither completely Simple, nor completely Complex.

Mechler & Ringach [79] have recently shown that spike-rate rectification could lead to a bimodal distribution in extracellular F_1/F_0, even though intracellular response is unimodally distributed (see also [1]). Our work here shows that this result can arise within a network model which incorporates many elements that are biologically realistic. For our model, we note that the form of the intracellular and extracellular F_1/F_0 distributions changed little when the uniform distribution used for N_{LGN}, the number of LGN afferents impinging on a model V1 neuron, was replaced by a Gaussian distribution whose standard deviation was half its mean. When the N_{LGN} distribution was made strictly bimodal (1/2 the cortical cells receiving LGN excitation and 1/2 receiving none at all), this created an extracellular F_1/F_0 distribution with a greater population of Complex cells as seen in Fig. 3.4c, but also a plainly bimodal intracellular distribution.

3.3 Remarks

The main results thus far are these: We have constructed a neuronal network model, based on macaque V1, for the emergence of Simple and Complex cells within the same basic circuit. Their different responses reflect the underlying distribution of geniculate versus cortico-cortical excitation. While the amount of excitation is kept roughly fixed, its division varies widely from cell to cell, as do many other elements of the model, such as strength of coupling and of extra-cortical drive, and the receptive field properties of

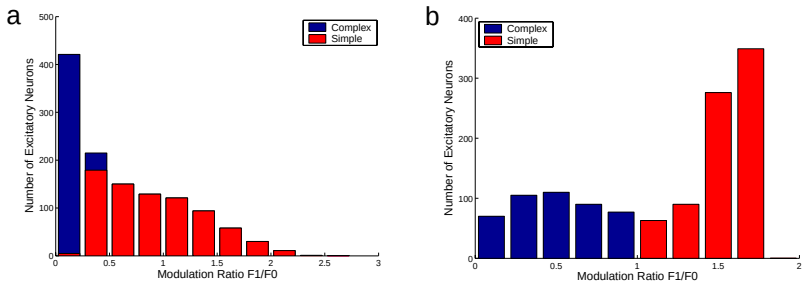

Figure 3.4: Comparison of intracellular and extracellular F_1/F_0 between model and experiment. (a) Distribution of F_1/F_0 of membrane potential (relative to background activity) of excitatory neurons in model network, when stimulated at optimal orientation and spatial frequency. The height of each bar indicates the total number of excitatory neurons in each bin, while the blue and red portions correspond to the cells that are classified as "Simple" or "Complex" based on their extracellular responses. 9b) Distribution of the modulation ratio F_1/F_0 of the firing rate for excitatory neurons in model network. (The distribution for the inhibitory population is qualitatively similar.) For these two distributions, only cells with mean rates above 8 spikes/second are included. [Reproduced from Ref. [124].]

convergent LGN excitation. In a manner consistent with experiment measurement, we predict a bimodal but broad structure of extracellular modulation ratio, itself arising from a distribution of intra-cellular modulation ratios that is broad *but* monotonic.

This model is very different from the influential hierarchical model of Hubel & Wiesel [49], wherein Simple cells receive geniculate drive and their pooled output drives the Complex cells. Clearly, a strict rendering of the Hubel & Wiesel model would yield a bimodal population response in both the extra- and intra-cellular modulation ratio, as is not observed here, nor in experiment. Our model is more egalitarian than hierarchical, with all cell types receiving strong inputs from the network of both simple and complex cells and with almost all cells receiving LGN drive.

A crucial feature of our model is cortico-cortical inhibition, which allows the possibility of nearly linear, Simple cell responses in the network, even when driven by LGN cells with their attendant rectification nonlinearities [131].

While our model is motivated by an interpretation of macaque V1 cortical architecture [77, 131] and instantiated in a large-scale computational model with spiking neurons, it shares important features with the modeling of Chance et al [29]. As in [29], recurrent excitation plays a central role in creating Complex cell responses. However, in our model recurrent excitation does not so much play the role of yielding phase invariant responses, as in Chance et al, but rather in yielding sufficiently high, physiologically reasonable firing rates for complex cells that are also being inhibited. Phase invariance is built into the Complex cell's total synaptic input by summing over both Complex cells

and Simple cells nonspecifically. In an elaboration of their basic model, Chance et al also demonstrated that a mixed population of Simple, Complex, and intermediate cells could be found by randomly varying the strength of connectivity to the model cortical network.

Finally, we have emphasized in this chapter the form of the model's cycle- or time-averaged responses. However, examination of Figs. 3.2 and 3.3 show that instantaneous values of V_S and the conductances are strongly fluctuating, with the mean V_S mostly below, or barely above, the threshold to firing. Clearly, fluctuations are important to creating the network state. Futhermore, as large ranges in coupling parameters were explored, regions where multi-stable and hysteretic behavior (with respect to stimulus parameters) were uncovered, we found that stable and physiologically realistic behavior can only be maintained by adding background noise. It is at this point when we realized the importance of fluctuations in the membrane potential and synaptic conductances, issues which we will address in the next Chapter.

Chapter 4

Orientation Selectivity and Fluctuation-Driven Criticality

Orientation selectivity and spatial summation are two of the most fundamental visual processing tasks performed by the mammalian primary visual cortex (V1). V1 is the first area along the visual pathway where neurons are selective for stimulus orientation. Individual neurons in V1 respond preferentially to lines and edges of a particular orientation. This orientation selectivity is also independent of stimulus contrast: In computing orientation tuning curves, i.e., firing rates of individual neurons as a function of stimulus orientation, the bandwidth (half-width at half maximum), the circular variance (CV), and the orientation selectivity index of individual tuning curves are roughly independent of stimulus contrast. How orientation selectivity arises in V1 has not been fully understood [38, 119]. According to the classical Hubel and Wiesel picture, orientation selectivity directly arises from the convergence of lateral geniculate (LGN) afferents [51]. However, modeling based on the Hubel and Wiesel, or the "feedforward," picture shows that the degree of selectivity provided by the convergent LGN inputs alone is insufficient to account the selectivity of individual neurons [119]. Some form of cortical processing must be necessary. Furthermore, in purely feedforward models, at higher contrasts broader tuning is expected since the feedforward drive surpasses threshold at more orientations. (This is the so-called iceberg effect.) Noise in the membrane potential has been suggested to be important for shaping contrast invariance [5, 45, 83, 110]. However, how this "noise" arises in the visual cortical network is yet to be elucidated.

Modifications of the feedforward scheme follow Hebbian ideas to posit cortical circuitry with highly specific cortical inhibition. The push-pull model is an example of such a modification: intracortical inhibition is anti-correlated with the excitatory synaptic drive [127]. However, other models, without highly specific coupling, demonstrate that selectivity can arise from the sharpening of weakly tuned feedforward excitation by broadly tuned intracortical inhibition (see, e.g., [3, 27, 117]). The so-called marginal phase arises when cortical excitation is sufficiently strong to allow symmetry-breaking states [10].

In the previous chapter, we reviewed how simple and complex cellular responses arise in a large-scale neuronal network model of an input layer $4C\alpha$ of macaque V1 [124]. In the previous model, a continuum of simple and complex cellular responses arise from the varying degrees of balance between cortico-cortical and feedforward inputs: the most "simple" of the model neurons are driven strongly by the LGN and are "linearized" by strong cortical inhibition [131], while the most "complex" receive strong cortical excitation and inhibition [124]. While this model was capable of reproducing many aspects of simple and complex cell behavior, it does not have complex cells that are orientation selective. The strong cortical amplification causes an apparent bistability: complex cells tend to fire at rates that are too high (and are limited by the absolute refractory period) or not at all. Reasonable complex cell firing rates can be obtained after the introduction of sufficiently strong noise. In [23], we suggested that strong cortical fluctuations may stabilize network dynamics and allow complex cell selectivity. In this chapter, within the framework of a simplified version of [124], we demonstrate how strong synaptic fluctuations in sparsely-coupled networks or networks with synaptic failure, can transform destabilizing recurrent network amplification to near-bistability in a regime dominated by fluctuations. In simple cells, strong dynamic synaptic fluctuations provide the "noise" to circumvent the iceberg effect. In complex cells, the near bistability provides steep, graded response to recurrent amplification to achieve contrast-invariant orientation selectivity. Finally, the role of synaptic fluctuations is analyzed detail using the bifurcation structure of an all-to-all network model.

In contrast with the all-to-all model reviewed in the previous chapter, the modeling results here were taken from a *sparsely coupled* network. We use the p_{kl}^{j} terms in Eq. 2.2 to model sparsity in the network coupling. That is, for each pair of neurons j,k, p_{kl}^{j} is independent of l and is chosen to be 1 with probability $p = 1/N_{eff}$. Note that the spatial coupling kernel still has Gaussian lengthscales. Unless otherwise noted, the results presented below were from network simulations with $N_{eff} = 96$ (i.e., each neuron projects to 96 postsynaptic target neurons).

4.1 Orientation Selectivity in a Large-Scale Model of V1

Orientation selectivity is measured using orientation tuning curve, i.e., time-average firing rates as a function of stimulus orientation. A tuned neuron responds strongly at a few orientations and shows very little response at the "orthogonal" orientation. In our large-scale model, both simple and complex cells show orientation selective responses. Figure 4.1 shows the tuning properties of sample neurons: well-tuned firing rates for both simple and complex cells, regardless of their location within their respective orientation hypercolumns (see, for instance, [70,74,106]). On the other hand, the membrane potential and the total conductance are tuned more broadly in neurons near pinwheel centers (Fig. 4.1a-d) than in the iso-orientation domains (Fig. 4.1e-f) (see also, [74,106]). Furthermore, in iso-orientation domains, the firing-rate, membrane-potential, and conductance tuning curves for a given neuron are well aligned in orientation angle with one another (their peaks are at the same angle locations), while near the pinwheel centers the relationship

between the conductance and firing-rate tuning curves is, in general, more varied and complicated (for example, their peak locations can differ) [74].

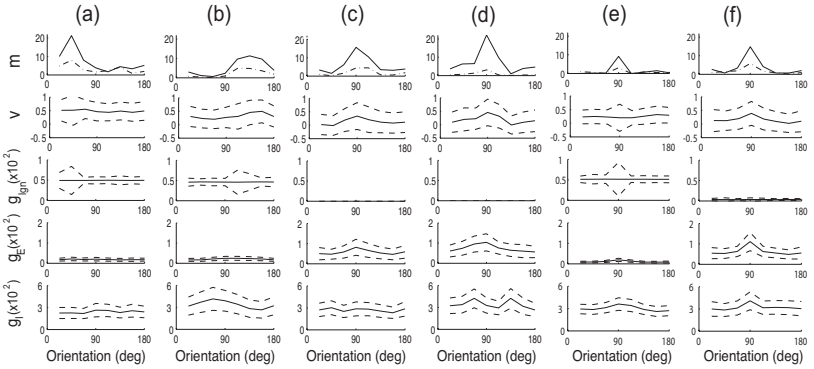

Figure 4.1: Tuning curves for neurons near the pinwheel center (a–d) and in iso-orientation domains (e,f); (a,b,e) are simple and (c,d,f) complex cells. Firing rate, membrane potential, geniculate excitation, excitatory and inhibitory cortico-cortical conductances are plotted. Solid lines represent the mean values at medium contrast. Dash-dotted lines represent the mean values at low contrast. Dashed lines represent the mean plus/minus one standard deviation. There is little or no LGN input to complex cells in (c,d,f). [Reproduced from Ref. [123].]

One quantitative measure of orientation selectivity for drifting grating stimuli is the circular variance (CV), defined as $CV[m] = 1 - \left|\int_0^\pi m(\theta)\, e^{2i\theta}\, d\theta\right| / \int_0^\pi m(\theta)\, d\theta$, where $m(\theta)$ is the time-averaged firing rate. CV is near 0 for well-tuned neurons, near 1 for poorly-tuned neurons, and in-between otherwise. We display the statistical distribution of the CV for the excitatory neurons in our network in Figure 4.2. In particular, Fig. 4.2a reveals the approximate contrast invariance of orientation selectivity [5], and Fig. 4.2b shows that orientation selectivity of the firing rates is almost independent of the neuron's location within the orientation column [70, 74, 106].

The mechanism for orientation tuning in iso-orientation domains is relatively simple: all neurons receive spikes only from neighbors with like orientation preference, so all the cortical conductances, membrane potentials, and firing rates are simply sharpened versions of the LGN drive. Near pinwheel singularities, however, sparsity of connections in our model network is needed for conductances and membrane potentials to be tuned. Namely, in a densely connected network, they would be untuned as they would be composed of roughly equal contributions from a number of LGN-drive-dominated simple cells with all possible orientation preferences. Sparsity is thus also needed to achieve tuned firing rates for complex cells near pinwheel centers, since untuned conductances could not confer any tun ing upon them. (See [123] for details.) In addition, strong cortical amplification is needed to sharpen the complex cell tuning, and strong gain for contrast invariance. Synaptic fluctuations in the network, again induced by its sparsity, give

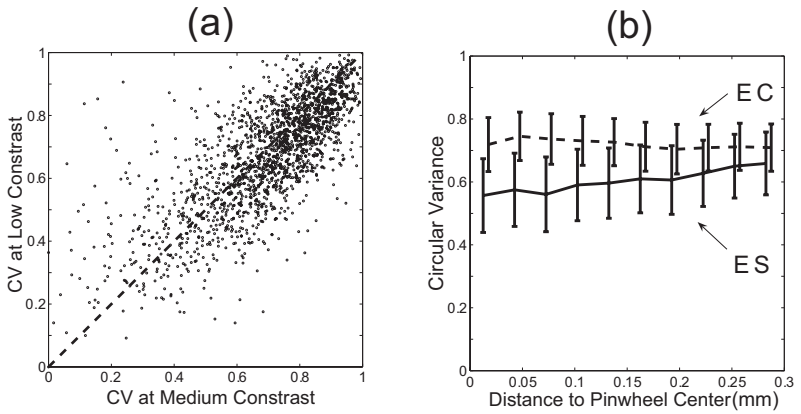

Figure 4.2: (a) Circular variance at medium versus low contrasts. (b) Dependence of circular variance on the distance from a pinwheel center: E C and ES are excitatory complex and simple cells, respectively. [Reproduced from Ref. [123].]

it stability. Our modeling work further reveals that there is a bifurcation mechanism, the "fluctuation-controlled criticality" [123], underlying the orientation tuning dynamics of simple and complex cells.

In producing these model results, large regions of the synaptic coupling strength parameter space were explored. We find that in order to have contrast invariant orientation selective complex cells, there must be strong recurrent excitation [124] with large temporal fluctuations [23]. To understand the effect of synaptic fluctuations on network dynamics, we systematically varied N_{eff}, through synaptic failure or through network sparsity.

Without sufficient synaptic fluctuations, the complex cells tended to be bistable in the presence of the strong recurrent excitation needed for cortical amplification and for orientation tuning. This can be illustrated by comparing model networks with different N_{eff}. Fixing the stimulus (drifting grating) orientation (say, at θ_0), the stimulus contrast was increased from zero contrast to 100% contrast before it was decreased to zero. Let ΔN_{spikes} denote the difference in the number of spikes during the contrast decrement and during the contrast increment. Figure 4.3 shows the distribution of ΔN_{spikes} of the excitatory simple and the excitatory complex population for networks with different N_{eff}. Fixing the stimulus (drifting grating) orientation (say, at θ_0), the stimulus contrast was increased from zero contrast to 100% contrast before it was decreased to zero. For the network model with $N_{eff} = 96$ ($N_e = 72$ and $N_i = 24$), the neurons are not hysteretic on average: the distribution of ΔN_{spike} is symmetric about 0. In the network with larger N_{eff} ($= 768$), the distribution of ΔN_{spikes} for the excitatory complex population is skewed: the complex cells are hysteretic in stimulus contrast. We note that this hysteresis increases as

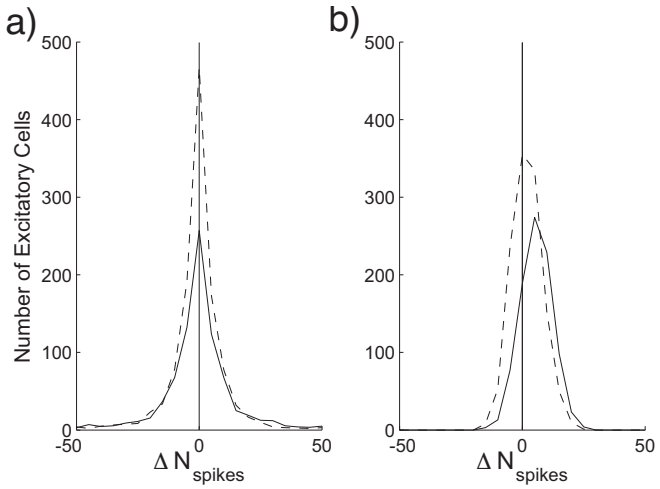

Figure 4.3: Firing-rate hysteresis in the V1 model as characterized by ΔN_{spikes}. $\Delta N_{spikes} > 0$ if the cell spiked more during the contrast decrease than increase. Simple cells are depicted by broken line and complex by solid line. (a) $N_{eff} = 96$. (b) $N_{eff} = 768$. [Reproduced from Ref. [123].]

N_{eff} is further increased.

4.2 Fluctuation-Controlled Criticality

The effect of intrinsic synaptic fluctuations can be further illustrated using a highly idealized, minimal network model. In this model, we let one half of the neurons receive feedforward drive in the form of Poisson spike trains with identical rates ν_0 and spike strengths f (simple cells), and the other half only strong intracortical excitation (complex cells). Both receive the same, strong, cortico-cortical inhibition. We ignore the detailed time-dependence and any spatial structure of the visual drive, and focus instead on the dynamics of networks containing two types of cells (simple or complex, i.e., strongly driven by feedforward or by recurrent excitation) in the presence of synaptic fluctuations. Figure 4.4 displays the complex cell population firing rate as a function of the mean feedforward drive, $g_{Input} = c_0 \nu_{LGN}$, in networks with the same synaptic coupling strengths but of different N_{eff}. These firing rate curves are obtained by first increasing and then decreasing in succession the feedforward input. In the $N_{eff} = 200$ network, hysteresis is observed as we ramp up and then down the strength of the feedforward drive. The transition is a saddle-node bifurcation in g_{Input} for the mean population firing rate. As N_{eff} is decreased (here by increasing the probability of synaptic failure, $1-p$), while strengthening individ-

ual synapses to keep the effective network drive constant, the region of bistable behavior in g_{Input} becomes smaller and smaller, until the bistability disappears completely and a smooth firing rate curve is observed (e.g., the curve for $N_{eff} = 25$).

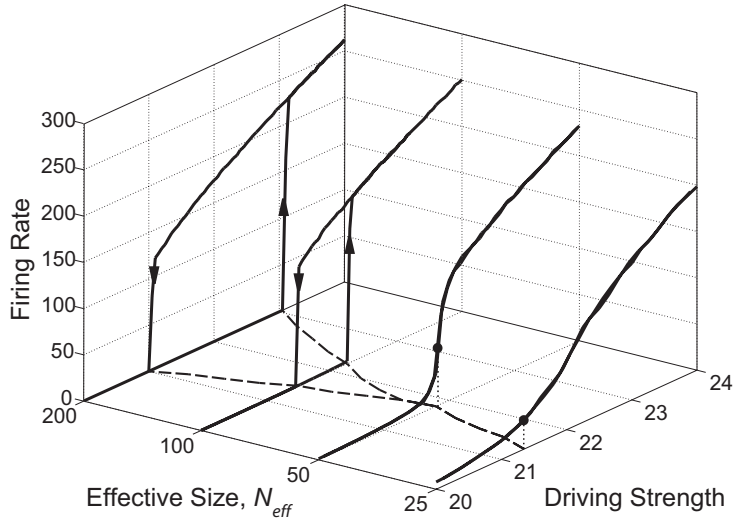

Figure 4.4: Bifurcation diagram near the "fluctuation-controlled criticality" in an idealized network. The firing rate is for complex cells. There is a transition to bistability as N_{eff} is increased. [Reproduced from Ref. [123].]

The transition also occurs when we change the relative contributions of fast and slow excitation (see [123]). NMDA receptors acts on a longer timescale and each PSC has a smaller temporal variance than a PSC mediated by AMPA receptors. Decreasing the NMDA component increases the amount of fluctuations, thus smoothing the gain curves and taking the network out of the bistable range.

To further illustrate the notion of fluctuation-driven dynamics, we rewrite the I&F equations as $\frac{dv^j}{dt} = -g_T(t)\left[v^j - V_S^j(t)\right]$, where g_T is the total conductance and V_S^j is an effective reversal potential, which is necessarily greater than the voltage threshold V_T whenever the neuron fires. In the statistically steady state situation, what distinguishes the bifurcation is the time-average of V_S^j. We say the dynamics is *mean-driven* whenever $\overline{V_S^j} = T^{-1}\int_{t_0}^{t_0+T} V_S^j(t)\,dt$ is greater than V_T, i.e., the mean of the synaptic input is sufficient to drive the neuron to fire. We call the other case *fluctuation-driven*, since temporal fluctuations in the drive are needed for spiking. This notion of fluctuation-driven dynamics is distinct from the dynamics of the so-called "balanced networks" where the overall excitatory and inhibitory currents nearly cancel [129, 130]. (In models of Sects. 3.1 and 3.2, the mean synaptic currents are strongly inhibitory and the effective reversal potentials are

far below threshold.)

Both intrinsic and extrinsic synaptic fluctuations have the effect of smoothing the relation between synaptic input and neuronal output in the form of spikes. With sufficiently strong recurrent excitation, as we increase the strength of synaptic fluctuations, the region of bistability in synaptic input shrinks to achieve near-hysteresis at a critical level of fluctuations. As we increase fluctuations even further, network is no longer hysteretic, but the network gain is decreased. Since this transition occurs as the amount of synaptic fluctuations is varied, we call it **fluctuation-controlled criticality**. The network dynamics near this point is characterized by near-bistability and rapid changing firing rates as a function of synaptic input.

4.3 Remarks

How contrast invariant orientation selectivity arises in V1 is one of the important problems of visual neuroscience [38, 119]. An immediate problem confronting any model is that the Hubel-Wiesel thalamo-cortical drive is broader at high contrasts, as the input at non-preferred orientations becomes super-threshold. Some form of noise is often invoked to provide contrast invariance in simple cells. Assuming that a transfer function between membrane potential and neuronal firing rates can be found, [45, 83] showed that a power transfer function is the only relation that transforms contrast invariant membrane potential tuning curves to contrast invariant spike responses. Within a wide range of contrasts, stimulus-independent noise does transform threshold-linear firing rate curves into approximate power laws in the membrane potential [26, 45, 83] consistent with experimental findings [5]. However, the effects of synaptic conductances has not been considered and how contrast invariant membrane potentials arise in the first place is not yet understood. Here we show that synaptic fluctuations provides a natural form of "noise," allowing the iceberg effect to be circumvented in simple cells, while the fluctuation-controlled criticality gives rise to contrast-invariant orientation-selective V1 complex cells.

While many of our model results can be analyzed using kinetic theory and population density equations [23], in this chapter, we have given a mechanistic account of how contrast invariance may be achieved in a fluctuation-driven setting, and relegate the framework for theoretical analysis to the next chapter. Here we have demonstrated that an important effect of synaptic fluctuations is to stabilize network dynamics in highly recurrent networks so that large cortical gain or amplification is possible at a fluctuation-controlled critical point, which we believe is the underlying mechanism governing contrast invariance in V1.

Chapter 5

An Effective Kinetic Representation of Neuronal Network Dynamics

In this chapter, we present a detailed theoretical framework for statistical descriptions of neuronal networks and derive $(1+1)$-dimensional kinetic equations, without introducing any new parameters, directly from conductance-based integrate-and-fire neuronal networks. We describe the details of derivation of our kinetic equation in the case of networks of excitatory neurons. A more complete description, containing, for instance, derivations of kinetic equations for networks consisting of both excitatory and inhibitory neurons, and for networks consisting of many coarse-graining patches, can be found in [22].

The dimension reduction in our theory is achieved via a novel moment closure. To establish accuracy, we compare the prediction of our kinetic theory with the full simulations of the original point-neuron networks.

The hierarchy of the multiple spatial and temporal scales in the cortical dynamics presents a significant theoretical challenge to computational neuroscience. While we may devise increasingly more efficient numerical methods for simulations of dynamics of large-scale neuronal networks [20, 77, 94, 117, 127], basic computational constraints will eventually limit the power of our simulations. Furthermore, to gain qualitative understanding of the cortical mechanisms underlying cortical processing, a major theoretical issue is how to derive effective dynamics under a reduced representation of large-scale neuronal networks. Therefore, we have developed efficient and effective representations for simulating and understanding the dynamics of larger, multi-layered networks. As suggested, for example, by the laminar structure of cat's or monkey's primary visual cortex, in which many cellular properties such as orientation preference are arranged in regular patterns or maps across the cortex [12–14, 36, 70], some neuronal sub-populations may be effectively represented by coarse-grained substitutes. Conceivably, we may partition the two-dimensional cortical layers into coarse-grained patches, each sufficiently large to

contain many neurons, and yet sufficiently small that these regular response properties of the individual neurons within each patch can be taken as constant for each neuron in the patch.

Furthermore, there is another important issue that needs to be addressed in coarse-graining, i.e., how to capture *fluctuation-dominated* spiking processes mathematically, because neuronal networks, as demonstrated in Chaps. 3 and 4, whether real cortical networks [5, 121] or computer models [20, 40, 110], frequently operate in a dynamical regime in which the spiking of individual neurons is caused by irregular temporal fluctuations of the membrane potential. In this cortical state, the mean membrane potential (say, obtained by averaging locally in time, or by trial averages, i.e., averaging over many voltage traces under the same stimulus condition), does not reach firing threshold, but fluctuations in the membrane potential do reach spiking threshold. We note that, since a purely excitatory network can still operate in a fluctuation-driven regime, this notion of fluctuation-dominated dynamics is distinct from the notion of fluctuation *near threshold* in the so-called balanced network that uses near cancellation of excitatory and inhibitory currents [129, 130].

In [23], starting with large-scale model networks of point neurons, which are sufficiently detailed for modeling neuronal computation of large systems, we tiled the model cortex with coarse-grained patches. We then derived an effective dynamics to capture the statistical behavior of the neurons within each coarse-grained patch in their interaction with other coarse-grained patches. We have used as extension of this kinetic theory to study rich dynamic phenomena within these networks, including transitions to bistability and hysteresis, even in the presence of large fluctuations. We have also used these representations to study simplified models of orientation selectivity to suggest the possible role of large fluctuations and cortico-cortical excitation in the orientation tuning of complex cells [23, 123]. This kinetic theory approach has been shown to be rather powerful, allowing for both computational scale-up and insight into the mechanisms underlying the operation of neuronal networks [21, 23].

In this chapter, we present the detailed theoretical framework for capturing these coarse-grained dynamics that can be fluctuation-dominated. (For earlier probabilistic representations, upon which our coarse-grained theory is based, see, e.g., [2, 9, 19, 30, 40, 42, 46, 60, 88–91, 93, 126, 133]). Starting with networks of conductance-based integrate-and-fire (I&F) neurons, we derive a full kinetic description directly, without introduction of any new parameters. In the limit of infinitely fast conductances, these kinetic equations can be further reduced to one-dimensional Fokker-Planck equations. As the number of point neurons N tends to infinity, our kinetic theory reduces further to the classical firing rate representation [110, 126, 134]. As pointed out in [23], at moderate and even small N, this kinetic theory captures the effects of large synaptic fluctuations, with efficiency and surprising accuracy. We establish the *dynamical* accuracy of our kinetic theory by benchmarking its predictions against the full simulations of the point neuron network under *time-inhomogeneous* inputs. Although the derivation of our kinetic theory assumes that the number of neurons in a coarse-grained patch is large, the numerical verification of this asymptotics shows that the number N can become as small as $\mathcal{O}(10)$, with accuracy retained [23]. As expected [23, 28, 46, 61], the kinetic representation is far more efficient

computationally than the full I&F network. The savings are two-fold: *(i)* For a given I&F network, the probability density representation eliminates the need for simulating to very long times or for simulating many ensembles so as to reduce the statistical error in computing firing rates; *(ii)* The reduction of the dimension, for probability density description, provides significant computational savings. For example, to achieve a firing rate computation with 1% accuracy for a network of 100 neurons, a reduction in computation time of 4-6 orders of magnitude can be easily obtained [23, 95].

5.1 All-to-all Coupled Excitatory Neuronal Networks

Let us start with a coupled network consisting of N all excitatory neurons with an exponential time-course for conductances. The dynamics of all-to-all coupled excitatory I&F neuronal network is governed by

$$\tau \frac{dV_i}{dt} = -(V_i - \varepsilon_r) - G_i(t)(V_i - \varepsilon_E), \tag{5.1a}$$

$$\sigma \frac{dG_i}{dt} = -G_i + f \sum_{\mu} \delta\left(t - t_{\mu}^{i}\right) + \frac{S}{N} \sum_{j} \sum_{\mu} p_{j\mu} \delta\left(t - t_{j\mu}\right), \tag{5.1b}$$

where V_i is the membrane potential of ith neuron in the network and σ is the decay timescale of the excitatory conductance time-course. S is the strength of coupling between neurons in the network. $p_{j\mu}$ describes the probability of synaptic release, which is modeled by a Bernoulli process, with release probability equal to p, i.e., $p_{j\mu} = 1$ with probability p; 0, otherwise. For each incoming external spike, the jump in the conductance of a neuron is f/σ, and, for each incoming spike from other neurons in the network, the jump in the conductance is $S/N\sigma$.

For a fixed neuron j, the output spike statistics of $\{t_{j\mu}\}$ is, in general, not Poisson. However, the input to the ith neuron is a spike train summed over output spike trains from many neurons in the network. If we assume that each neuron firing event has a very low rate and is statistically independent from each other, then the spike train obtained by summing over a large number of output spike trains of neurons in the network asymptotically tends to be a Poisson spike process [31]. Therefore, we will assume that the input spike train summed from all other neurons to the ith neuron is Poisson with rate $pNm(t)$, where $m(t)$ is the population-averaged firing rate per neuron and pN is an effective number of neurons that are coupled to neuron i.

To study the statistical behavior of the network, we construct a statistical ensemble of identically structured neuronal networks that differ only in their input, each of which is an independent set of N independent realizations of the Poisson input spike trains with the same rate $\nu_0(t)$. We are interested in what is the probability of finding a neuron whose voltage is in $(v, v+dv)$ and whose conductance is in $(g, g+dg)$ at time t. The corresponding probability density function is

$$\rho(v,g,t) = \mathbb{E}\left[\frac{1}{N}\sum_{i=1}^{N} \delta(v - V_i(t))\,\delta(g - G_i(t))\right].$$

where $\mathbb{E}(\cdot)$ is the expectation with respect to all possible sets of N independent realizations of the input Poisson spike process with rate $\nu_0(t)$ for given initial data (we can further average over an ensemble of initial conditions $V(0)$ if necessary.) Denote $\rho = \rho(v,g,t)$, the governing equation for the probability density is (see Appendix B of [22] for a detailed derivation)

$$\begin{aligned}
\partial_t \rho &= \partial_v \left\{ \left[\left(\frac{v-\varepsilon_r}{\tau} \right) + g \left(\frac{v-\varepsilon_E}{\tau} \right) \right] \rho \right\} + \partial_g \left(\frac{g}{\sigma} \rho \right) && \text{(5.2a)} \\
&\quad + \nu_0(t) \left[\rho \left(v, g - \frac{f}{\sigma}, t \right) - \rho(v,g,t) \right] && \text{(5.2b)} \\
&\quad + pm(t) N \left[\rho \left(v, g - \frac{\bar{S}}{pN\sigma}, t \right) - \rho(v,g,t) \right], && \text{(5.2c)}
\end{aligned}$$

for $v \in [\varepsilon_r, V_T)$ and $g \in [0,\infty)$, where $\bar{S} = pS$. The first two terms in Eq. (5.2) describe the streaming dynamics of neurons without receiving any spikes and the second term in Eq. (5.2a) describes the streaming arising from a finite σ. The third and fourth terms in Eq. (5.2) describe the conductance jumps of the neurons upon receiving external input spikes and spikes from other neurons in the network, respectively.

Eq. (5.2) is a $(2+1)$-dimensional partial differential equation with delays in g-space. Eq. (5.2) is not exact since the summed input from other neurons in the network is only approximately Poisson, and thus term (5.2c) is valid only in an asymptotic sense. We invoke a small-jump approximation to derive a $(2+1)$-dimensional, nonlinear advection-diffusion equation below, and discuss how to reduce the dynamics in two dimensions (v,g) to dynamics in only one dimension v.

5.1.1 Diffusion Approximation

Note that the jump in conductance of a neuron, induced by a single spike from another neuron in the network, is $\bar{S}/(pN\sigma)$, whereas the jump, induced by a single spike from the external input, is f/σ. Assuming that these jumps are small, we can Taylor expand $(5.2b)$ and $(5.2c)$ to get expansion to obtain

$$\partial_t \rho = \partial_v \left\{ \left[\left(\frac{v-\varepsilon_r}{\tau} \right) + g \left(\frac{v-\varepsilon_E}{\tau} \right) \right] \rho \right\} + \partial_g \left\{ \left[\frac{1}{\sigma} (g - \bar{g}(t)) \rho + \frac{\sigma_g^2(t)}{\sigma} \partial_g \rho \right] \right\} \quad (5.3)$$

with

$$\begin{aligned}
\bar{g}(t) &\equiv f\nu_0(t) + \bar{S}m(t), && \text{(5.4a)} \\
\sigma_g^2(t) &\equiv \frac{1}{2\sigma} \left[f^2 \nu_0(t) + \frac{\bar{S}^2}{pN} m(t) \right]. && \text{(5.4b)}
\end{aligned}$$

Eq. (5.3) can be written in conservation form:

$$\partial_t \rho + \partial_v J_V(g,v) + \partial_g J_G(g,v) = 0, \quad \text{for } v \in [\varepsilon_r, V_T), \text{ and } g \in [0,\infty),$$

with the flux

$$J_V(v,g) = -\left[\left(\frac{v-\varepsilon_r}{\tau}\right)+g\left(\frac{v-\varepsilon_E}{\tau}\right)\right]\rho(v,g), \tag{5.5a}$$

$$J_G(v,g) = -\left[\frac{1}{\sigma}(g-\bar{g}(t))\rho(v,g)+\frac{\sigma_g^2(t)}{\sigma}\partial_g\rho(v,g)\right], \tag{5.5b}$$

where the flux $J_V(v,g)$ and $J_G(v,g)$ are the flux along the v-direction and the g-direction, respectively.

The reset dynamics of our I&F neurons is instantaneous, i.e., once a neuron's voltage crosses the threshold V_T, the voltage resets immediately without any refractory period (i.e., without any delay) and the conductance stays with the same value upon voltage reset. Hence,

$$J_V(V_T,g) = J_V(\varepsilon_r,g), \quad \text{for } \forall g \in [0,\infty). \tag{5.6}$$

Boundary condition (5.6) simply expresses the fact that the neurons that just fired all enter through the reset voltage. Furthermore, since there are no neurons whose conductance will go below zero or go to infinity, the g-flux vanishes at the boundary $g=0$ and $g=\infty$, i.e.,

$$J_G(v,g=0)=0, \;\; J_G(v,g=\infty)=0, \quad \text{for } \forall v \in [\varepsilon_r,V_T). \tag{5.7}$$

Eqs. (5.6) and (5.7) constitute boundary conditions for Eq. (5.3).

One of the most important statistical characterizations of neuronal networks is the firing rate, which is often measured in physiological experiments to describe neuronal network properties. Here, the dynamics of the network (5.1) is described by the population-averaged firing rate per neuron as determined by the total probability flux across the threshold *regardless* of the values of conductance, i.e.,

$$\begin{aligned} m(t) &= \int_0^\infty J_V(V_T,g,t)\,dg \\ &= -\int_0^\infty \left[\left(\frac{v-\varepsilon_r}{\tau}\right)+g\left(\frac{v-\varepsilon_E}{\tau}\right)\right]\rho(V_T,g,t)\,dg. \end{aligned} \tag{5.8}$$

Once the solution $\rho(v,g,t)$ is known, we can determine the firing rate using Eq. (5.8). However, Eq. (5.3) is specified with the parameters $\bar{g}(t)$ and $\sigma_g^2(t)$, which are functions of $m(t)$ (see Eqs (5.4)). The firing rate $m(t)$, in turn, depends on the boundary value of $\rho(V_T,g,t)$ through Eq. (5.8). Therefore, Eq. (5.3) is a nonlinear equation.

Since Eq. (5.3) is a nonlinear $(2+1)$-dimensional partial differential equation, we can achieve computational advantage if we are able to reduce further the dynamics to a $(1+1)$-dimensional effective dynamics. Through this reduction, we can also gain analytical insight to the neuronal network dynamics. In what follows, we discuss, in turn, two possible reductions: *(i)* in the limit of *mean-driven* dynamics and *(ii)* in the limit of *fluctuation-driven* dynamics.

5.1.2 Closure in the Mean-Driven Limit

We define the *mean-driven limit* as the limit where $N \to \infty$, and $f \to 0$, $\nu_0(t) \to \infty$, but $f\nu_0(t) =$finite. In this limit, $\sigma_g^2(t) = 0$ from Eq. (5.4b) and there will be no fluctuations in the input conductance for a neuron from either external input or the input from other neurons in the network. In this all-to-all network, the input conductance from the external input without fluctuations will be the same to all neurons, i.e., the effect of the second term $f\sum_\mu \delta\left(t - t_\mu^i\right)$ in Eq. (5.1b) is equivalent to a smooth input $f\nu_0(t)$, whereas the third term, which signifies the network interaction, in Eq. (5.1b), is equivalent to a smooth input $pSm(t)$ to a neuron from all other neurons in the network — the fluctuations have been scaled away by the factor $1/\sqrt{N}$. Notice that, under these smooth conductance inputs without fluctuations, Eqs. (5.1) show the voltages of neurons can move rapidly from the reset voltage ε_r to the threshold V_T and fire, which leads to the observation that the knowledge about the value of conductance of a neuron does not provide much information about the value of the voltage of the neuron statistically. Therefore, intuitively, the dynamics of conductance and voltage are uncorrelated in the mean-driven limit. If the dynamics of conductance and voltage are assumed to be statistically independent, i.e.,

$$\rho(v,g,t) = \rho^{(v)}(v,t)\,\rho^{(g)}(g,t),$$

then, the marginalization of Eq. (5.3) to v and g yields

$$\partial_t \rho^{(v)}(v) = -\partial_v j_V(v) \tag{5.9a}$$

$$\frac{d}{dt}\langle g\rangle = -\frac{1}{\sigma}\left[\langle g\rangle - \bar{g}(t)\right] \tag{5.9b}$$

where

$$j_V = -\left[\left(\frac{v-\varepsilon_r}{\tau}\right) + \langle g\rangle\left(\frac{v-\varepsilon_E}{\tau}\right)\right]\rho^{(v)}(v), \quad \text{and} \quad \langle g\rangle \equiv \int g\rho^{(g)}(g,t)\,dg.$$

In the derivation, we have used the fact that the flux across the threshold V_T is equal to the flux entering through the reset voltage ε_r, i.e.,

$$\int_{\varepsilon_r}^{V_T} \partial_v\left\{\left[\left(\frac{v-\varepsilon_r}{\tau}\right) + g\left(\frac{v-\varepsilon_E}{\tau}\right)\right]\rho(v,g)\right\}dv = -J_V(V_T,g) + J_V(\varepsilon_r,g) = 0$$

by the boundary condition (5.6). Eqs. (5.9) are closed with respect to $\rho^{(v)}(v,t)$ and $\langle g\rangle(t)$: Eq. (5.9a) is a $(1+1)$-dimensional PDE that describes the evolution of $\rho^{(v)}(v,t)$, whereas Eq. (5.9b) describes the evolution of the average conductance $\langle g\rangle(t)$.

For the case of time-homogeneous external input, i.e., $\nu_0(t) = \nu_0$, a constant, we can determine the steady-state firing rate as follows. First, note that the flux j_V in Eq. (5.9a) is constant over (ε_r, V_T) for a steady state. This constant can be determined by the flux at the boundary V_T, at which, the flux j_V is equal to the firing rate. Therefore,

$$m = j_V(v) = -\left[\left(\frac{v-\varepsilon_r}{\tau}\right) + \langle g\rangle\left(\frac{v-\varepsilon_E}{\tau}\right)\right]\rho^{(v)}(v),$$

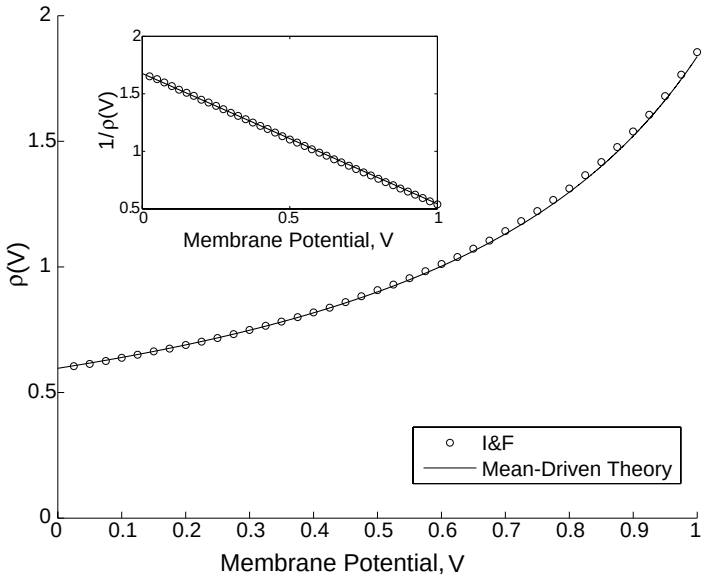

Figure 5.1: Mean-driven limit: Plotted here is the probability density function of a neuron's voltage. Solid line: Theoretic Prediction (5.10); Circles: Simulation of the original I&F neuronal network dynamics (5.1) in a steady state. Parameters are $N = 1600$, $f = 0.001$, $\nu_0 = 20000$, $S = 0.05$, $\sigma = 3ms$, $\tau = 20ms$ and $p = 1$. Inset: plotted is $1/\rho(v)$, which is a linear function of v from Eq. (5.10). We have scaled voltage units such that $\varepsilon_r = 0$ $V_T = 1$, and $\varepsilon_E = 14/3$ [77]. This convention of units will be used throughout all the figures in this chapter. [Reproduced from Ref. [22].]

For a steady state in a mean-driven regime, the probability density thus has the following form:

$$\rho^{(v)}(v) = -\frac{m\tau}{(v-\varepsilon_r)+\langle g\rangle(v-\varepsilon_E)} \quad \text{for } v \in [\varepsilon_r, V_T), \tag{5.10}$$

and $\rho^{(v)}(v) = 0$ for $v \notin [\varepsilon_r, V_T)$, where $\langle g\rangle = \bar{g} = f\nu_0 + \bar{S}m$ by Eq. (5.9b). Using the normalization condition $\int_{\varepsilon_r}^{V_T} dv\rho^{(v)}(v) = 1$ and noticing that the denominator in Eq. (5.10) must be negative to ensure $\rho^{(v)}(v) \geq 0$, we arrive at

$$m = \begin{cases} \dfrac{1+\bar{g}}{\tau \log\left|\dfrac{\bar{g}(\varepsilon_r-\varepsilon_E)}{(V_T-\varepsilon_r)+\bar{g}(V_T-\varepsilon_E)}\right|}, & \text{if } \bar{g} > \dfrac{V_T-\varepsilon_r}{\varepsilon_E-V_T} \\ 0, & \text{otherwise} \end{cases} \tag{5.11}$$

with $\bar{g} = f\nu_0 + \bar{S}m$. By solving Eq. (5.11) for m, we can determine the firing rate. Note that Eq. (5.11) is not a new result and is commonly quoted in literature (see, for example, [110, 126]). Here, we merely illustrate how to use the probability density description to reproduce this result.

Finally, we point out that, for an integrate-and-fire neuronal network operating in a mean-driven regime, the probability distribution for voltage is indeed well captured by Eq. (5.10), as is illustrated in Fig. (5.1).

5.1.3 Closure in Fluctuation-driven Regimes

In general, unlike in the mean-driven limit, g and v are correlated. Stronger fluctuations in g are expected to correlate with larger values of v. To describe this general dynamics, here, for the network described by Eq. (5.1), we derive a system of $(1+1)$-dimensional kinetic equations.

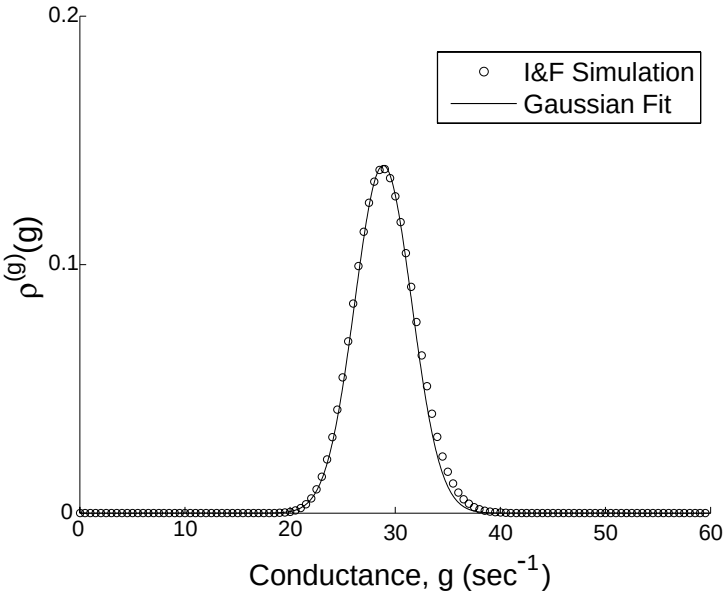

Figure 5.2: Conductance dynamics: Probability density function of g. Circles: Simulation of the original I&F neuronal network dynamics (5.1); Solid line: Gaussian fit (5.13). [Reproduced from Ref. [22].]

Dynamics of Conductances

Using the flux condition (5.6) at the boundary, we integrate Eq. (5.3) over v to obtain

$$\partial_t \rho^{(g)}(g) = \partial_g \left[\frac{1}{\sigma}(g - \bar{g}(t))\rho^{(g)}(g) + \frac{\sigma_g^2(t)}{\sigma}\partial_g \rho^{(g)}(g) \right] \tag{5.12}$$

for $g \in [0, +\infty)$. The flux $J_g(g) = -\left[\sigma^{-1}(g - \bar{g}(t))\rho^{(g)}(g) + \sigma^{-1}\sigma_g^2(t)\partial_g \rho^{(g)}(g)\right]$ vanishes at $g = 0$ and $g = \infty$. For time-homogeneous input, ν_0 and σ_g^2 are constant, and the time-invariant solution can be approximated by the following Gaussian solution

$$\rho^{(g)}(g) = \frac{1}{\sqrt{2\pi}\sigma_g} \exp\left[-\frac{1}{2\sigma_g^2}(g - \bar{g})^2 \right] \tag{5.13}$$

where $\bar{g} = \nu_0 f + \bar{S}m$, under the condition $f\nu_0 + \bar{S}m \gg \sigma_g$. Hence, the mean and variance of the conductance are

$$mean(g) = \bar{g}, \quad var(g) = \sigma_g^2,$$

respectively. If the domain of g were $(-\infty, \infty)$, then Eq. (5.13) would be exact. The numerical simulation of the full original I&F dynamics (5.1) demonstrates that in certain regimes this approximate solution well captures the distribution of conductance as shown in Fig. (5.2). Note that the time-scale for the evolution of $\rho^{(g)}(g)$ is σ. For sufficiently small σ, starting with any initial condition of $\rho^{(g)}(g)$, the solution rapidly converges to the approximate form in Eq. (5.13). If the time-scale of a time-dependent $\sigma_g^2(t)$ is much slower than σ (which generally is the case for AMPA conductances, which are much faster than typical time-scales of stimulus input [62]), then, in the limit of $\sigma \to 0$, $\rho^{(g)}(g,t)$ is essentially slaved to the time-invariant solution that has the approximate form in Eq. (5.13).

Dynamics of Membrane Potentials

Next, we project out the variable g from Eq. (5.3). Define the conditional moments

$$\mu_1(v) = \int_0^\infty g\rho(g|v)\,dg, \quad \mu_2(v) = \int_0^\infty g^2\rho(g|v)\,dg,$$

where

$$\rho(v,g) = \rho(g|v)\rho^{(v)}(v), \quad \text{and} \quad \rho^{(v)}(v) = \int_0^\infty \rho(v,g)\,dg.$$

Integrating Eq. (5.3) over g yields

$$\partial_t \rho^{(v)}(v) = \partial_v \left\{ \left[\left(\frac{v - \varepsilon_r}{\tau} \right) + \mu_1(v) \left(\frac{v - \varepsilon_E}{\tau} \right) \right] \rho^{(v)}(v) \right\}, \tag{5.14}$$

and multiplying Eq. (5.3) by g, then integrating over g yields

$$\begin{aligned}\partial_t\left[\mu_1(v)\rho^{(v)}(v)\right] &= -\frac{1}{\sigma}\left[\mu_1(v)-\bar{g}(t)\right]\rho^{(v)}(v) \\ &\quad +\partial_v\left[\left(\frac{v-\varepsilon_r}{\tau}\right)\mu_1(v)\rho^{(v)}(v)\right]+\partial_v\left[\left(\frac{v-\varepsilon_E}{\tau}\right)\mu_2(v)\rho^{(v)}(v)\right],\end{aligned} \tag{5.15}$$

where we have used Eq. (5.5b) and the boundary conditions (5.7). Using Eq. (5.14), we can cast Eq. (5.15) in the following form

$$\begin{aligned}\partial_t\mu_1(v) &= -\frac{1}{\sigma}\left(\mu_1(v)-\bar{g}(t)\right)+\left[\left(\frac{v-\varepsilon_r}{\tau}\right)+\mu_1(v)\left(\frac{v-\varepsilon_E}{\tau}\right)\right]\left[\partial_v\mu_1(v)\right] \\ &\quad +\frac{\Sigma^2(v)}{\rho(v)}\partial_v\left[\left(\frac{v-\varepsilon_E}{\tau}\right)\rho^{(v)}(v)\right]+\left[\partial_v\Sigma^2(v)\right]\left(\frac{v-\varepsilon_E}{\tau}\right),\end{aligned} \tag{5.16}$$

where

$$\Sigma^2(v)\equiv\mu_2(v)-\mu_1^2(v)$$

is the conditional variance.

Closure

Equations (5.14) and (5.16) show that the evolution of $\rho^{(v)}(v)$ depends on the first conditional moment $\mu_1(v)$ and that the evolution of $\mu_1(v)$ depends on the second moment $\mu_2(v)$ through the conditional variance $\Sigma^2(v),\ \cdots$. Therefore, projecting the dynamics (5.3) to the variable v generates a hierarchy of an infinite number of equations governing the conditional moments. A theoretical issue naturally arises: how to truncate this hierarchy to a closed set of equations of a lower order such that the truncated dynamics can still capture the essential dynamics of the system. Mathematically, a closure issue is often a coarse-graining issue, namely, whether there exits a scale below which the dynamics either by itself is sufficiently slowly varying function of v. If so, then, we can postulate the following **closure:**

$$\Sigma^2(v,t)=\sigma_g^2(t). \tag{5.17}$$

Therefore, we have $\partial_v\Sigma^2(v)=0$ and Eq. (5.16) becomes

$$\begin{aligned}\partial_t\mu_1(v) &= -\frac{1}{\sigma}\left[\mu_1(v)-\bar{g}(t)\right]+\frac{\sigma_g^2(t)}{\rho^{(v)}(v)}\partial_v\left[\left(\frac{v-\varepsilon_E}{\tau}\right)\rho^{(v)}(v)\right] \\ &\quad +\left[\left(\frac{v-\varepsilon_r}{\tau}\right)+\mu_1(v)\left(\frac{v-\varepsilon_E}{\tau}\right)\right]\partial_v\mu_1(v).\end{aligned} \tag{5.18}$$

Now Eqs. (5.14) and (5.18) are closed with respect to $\rho^{(v)}(v)$ and $\mu_1(v)$. In summary,

$$\partial_t \rho^{(v)}(v) = \partial_v \left\{ \left[\left(\frac{v-\varepsilon_r}{\tau} \right) + \mu_1(v) \left(\frac{v-\varepsilon_E}{\tau} \right) \right] \rho^{(v)}(v) \right\}, \tag{5.19a}$$

$$\begin{aligned} \partial_t \mu_1(v) = & -\frac{1}{\sigma}\left[\mu_1(v) - \bar{g}(t)\right] + \frac{\sigma_g^2(t)}{\rho^{(v)}(v)} \partial_v \left[\left(\frac{v-\varepsilon_E}{\tau} \right) \rho^{(v)}(v) \right] \\ & + \left[\left(\frac{v-\varepsilon_r}{\tau} \right) + \mu_1(v) \left(\frac{v-\varepsilon_E}{\tau} \right) \right] \partial_v \mu_1(v) \end{aligned} \tag{5.19b}$$

constitute our key result: kinetic equations for dynamics of coupled excitatory neuronal networks. From Eq. (5.19a), the corresponding probability flux clearly is

$$\mathscr{J}_V(v,t) = -\left[\left(\frac{v-\varepsilon_r}{\tau} \right) + \mu_1(v) \left(\frac{v-\varepsilon_E}{\tau} \right) \right] \rho^{(v)}(v). \tag{5.20}$$

Therefore, the population-averaged firing rate per neuron is determined by the flux (5.20) at the threshold:

$$m(t) = \mathscr{J}_V(V_T, t).$$

Boundary Conditions

Now we discuss how to derive boundary conditions for the kinetic equations (5.19). Note the probability flux (5.5a) along the v-direction satisfies the boundary condition (5.6). Therefore,

$$\int_0^\infty J_V(V_T, g)\, dg = \int_0^\infty J_V(\varepsilon_r, g)\, dg,$$

which leads to

$$\left[(V_T - \varepsilon_r) + (V_T - \varepsilon_E)\, \mu_1(V_T) \right] \rho^{(v)}(V_T) = (\varepsilon_r - \varepsilon_E)\, \mu_1(\varepsilon_r)\, \rho^{(v)}(\varepsilon_r) \tag{5.21}$$

Furthermore, for the quantity,

$$\eta(v) = \int_0^\infty g J_V(v,g)\, dg$$

using the closure (5.17), it is easy to show that

$$\eta(v) = \mathscr{J}_V(v,t)\, \mu_1(v) - \sigma_g^2 \left(\frac{v-\varepsilon_E}{\tau} \right) \rho^{(v)}(v)$$

with $\mathscr{J}_V(v,t)$ as in Eq. (5.20). The boundary condition (Eq. (5.6)) entails

$$\eta(V_T) = \eta(\varepsilon_r),$$

i.e.,

$$\begin{aligned} & \mathscr{J}_V(V_T,t)\,\mu_1(V_T) - \sigma_g^2\left(\frac{V_T-\varepsilon_E}{\tau}\right)\rho^{(v)}(V_T) \\ = \quad & \mathscr{J}_V(\varepsilon_r,t)\,\mu_1(\varepsilon_r) - \sigma_g^2\left(\frac{\varepsilon_r-\varepsilon_E}{\tau}\right)\rho^{(v)}(\varepsilon_r) \end{aligned}$$

Note that $\mathscr{J}_V(V_T,t) = \mathscr{J}_V(\varepsilon_r,t) = m(t)$. Hence,

$$\tau m(t)\left[\mu_1(V_T) - \mu_1(\varepsilon_r)\right] = \sigma_g^2\left[(V_T-\varepsilon_E)\,\rho^{(v)}(V_T) - (\varepsilon_r-\varepsilon_E)\,\rho^{(v)}(\varepsilon_r)\right]. \qquad (5.22)$$

Eqs. (5.21) and (5.22) constitute nonlinear boundary conditions for the kinetic equations (5.19).

5.1.4 Accuracy of Kinetic Theory

As pointed out in Ref. [23], our kinetic theory can reproduce the voltage distribution and network firing rates very well. Figure (5.3) illustrates a comparison between the predictions of our kinetic theory and the full numerical simulation of the original I&F excitatory-only neuronal networks (5.1) in a steady state. Note that even when the conductance mean input $G_{input} = f\nu_0$ is not sufficiently strong to force a neuron to fire in the mean-driven limit (for example, for the values of $G_{input} < 13.6$ in Eq. (5.11)), our kinetic theory captures the fluctuation-induced firing very well, as shown in Fig. (5.3). Further, here we show that the time-dependent solutions of our kinetic theory can also capture very well the original dynamics of the full I&F neuronal network (5.1). Figure (5.4) clearly demonstrates the dynamical accuracy of our kinetic theory.

We note that under the mean-driven limit, i.e., $N \to \infty$, and $f \to 0$, $\nu_0 \to \infty$, with $f\nu_0$ =finite, for which $\sigma_g^2 = 0$, the kinetic equations (5.19) recovers the mean-driven equations (5.9) with $\langle g\rangle$ being slaved to $\bar{g}$. Therefore, our kinetic theory has a wide range of validity — from the mean-driven regimes to the fluctuation-dominate regime. We will further discuss the issue of v-g correlation and fluctuations below.

5.1.5 Fokker-Planck Equation

The kinetic equations (Eqs (5.19)) can be viewed as asymptotic equations for describing the neuronal network dynamics for small but finite σ. Now we discuss the $\sigma \to 0$ limit of kinetic equations (Eqs (5.19)). Note that

$$\sigma\sigma_g^2(t) = \frac{1}{2}\left[f^2\nu_0(t) + \frac{\bar{S}^2}{Np}m(t)\right] \sim \mathscr{O}(1).$$

As $\sigma \to 0$, Eq. (5.19b) reduces to

$$\begin{aligned} \mu_1(v) &= \bar{g}(t) + \frac{\sigma\sigma_g^2}{\rho^{(v)}(v)}\partial_v\left[\left(\frac{v-\varepsilon_E}{\tau}\right)\rho^{(v)}(v)\right] \\ &= \bar{g}(t) + \frac{\sigma\sigma_g^2}{\tau} + \frac{\sigma\sigma_g^2}{\rho^{(v)}(v)}\left(\frac{v-\varepsilon_E}{\tau}\right)\partial_v\rho^{(v)}(v). \end{aligned} \qquad (5.23)$$

This expression of $\mu_1(v)$ makes it transparent the meaning of corrections to the first term in Eq. (5.23), i.e., $\bar{g}(t)$, which describes the mean-driven, uncorrelated limit.

Finally, substituting Eq. (5.23) into Eq. (5.19a) yields the following Fokker-Planck equation,

$$\partial_t \rho^{(v)}(v) = \partial_v \left\{ \left[\left(\frac{v-\varepsilon_r}{\tau} \right) + \gamma(t) \left(\frac{v-\varepsilon_E}{\tau} \right) \right] \rho^{(v)}(v) + \sigma \sigma_g^2(t) \left(\frac{v-\varepsilon_E}{\tau} \right)^2 \partial_v \rho^{(v)}(v) \right\} \tag{5.24}$$

where $\gamma(t) \equiv \bar{g}(t) + \sigma \sigma_g^2(t)/\tau$. Clearly, we have condition that $\int_{\varepsilon_r}^{\varepsilon_E} \rho^{(v)}(v)\, dv = 1$. The probability flux in Eq. (5.24) is

$$J_{\text{FP}}(v,t) = -\left[\left(\frac{v-\varepsilon_r}{\tau} \right) + \gamma(t) \left(\frac{v-\varepsilon_E}{\tau} \right) \right] \rho^{(v)}(v) - \sigma \sigma_g^2(t) \left(\frac{v-\varepsilon_E}{\tau} \right)^2 \partial_v \rho^{(v)}(v).$$

5.2 Remarks

In this chapter, we developed a coarse-grained representation of the dynamics of an all-to-all coupled, excitatory-only neuronal network, in terms of kinetic equations, directly from the original Integrate-and-Fire system of equations. Comparison with full numerical simulations of the original I&F network established that the reduced dynamics is very accurate and numerically efficient. Both analytical insight and scale-up of numerical represtation can be achieved by this kinetic approach. For instance, in [23], using a version of this theory, we studied orientation selectivity of a network model in a ring architecture. In [22], we present detail derivations of the kinetic equations for networks consisting of both excitatory and inhibitory neurons and extend the theoretical framework to describe the interaction between many coarse-grained patches.

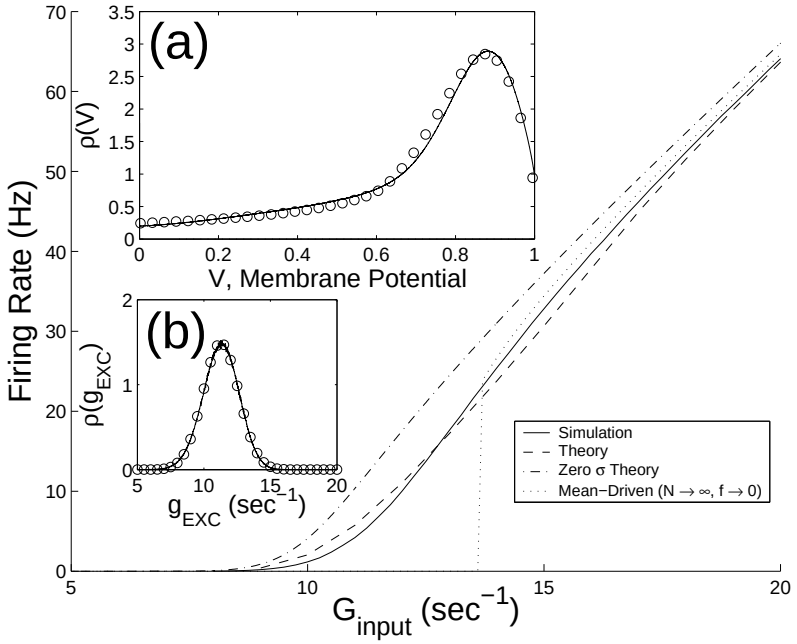

Figure 5.3: Steady state accuracy of kinetic theory for a case of fluctuation-driven dynamics: The population-averaged firing rate per neuron m as a function of mean input conductance $G_{input} = f\nu_0$. Inset: probability density function of the membrane potential. Circles: Simulation of the original excitatory-only I&F neuronal dynamics (5.1) in a statistical steady state; Solid line: Kinetic Theory (5.19); Dot-dashed line: Fokker-Planck Equation (5.24); Dotted line: Mean-Driven Limit (5.11). Parameters: $f = 0.01, S = 0.05$, $\sigma = 3ms$, $\tau = 20ms$, $N = 300$, and $p = 0.25$. ($\nu_0 = 1200$ for the inset.) [Reproduced from Ref. [22].]

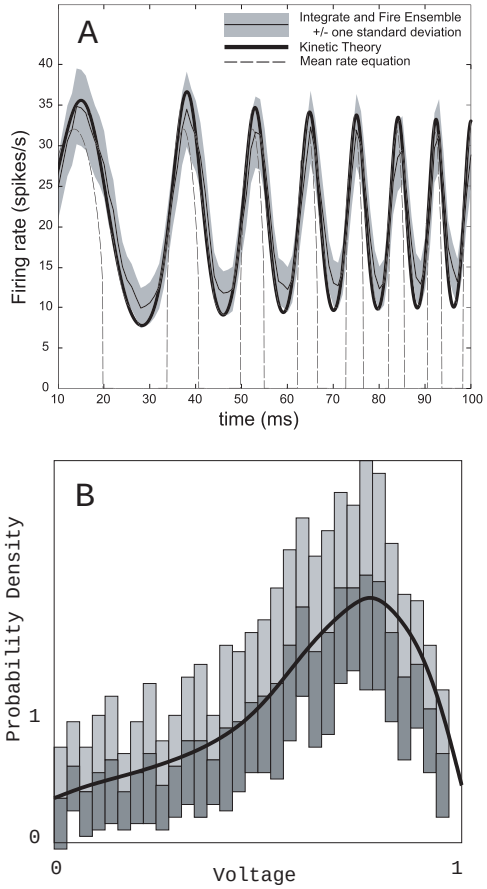

Figure 5.4: Dynamical accuracy of kinetic theory in a fluctuation-driven regime: Plotted for a network (5.1) of $N = 100$ excitatory I&F neurons driven by a time-varying input rate $\nu_0(t) = \nu_a \exp\left[0.25\sin(2\pi t/s + (2\pi t/s)^2)\right]$, where $\nu_a = 0.5 spikes/ms$, $s = 100ms$, is (A) The firing rate $m(t)$ (Thin solid line: simulation result averaged over an ensemble of 10^4 identically structured networks. The firing rate is measured using a bin size of 1msec. The upper and lower boundaries of the gray area mark the values one-standard deviation away from the mean, measured from an ensemble of the 10^4 networks. Thick solid line: Kinetic theory (5.19). Dashed line: Mean-driven limit (5.11)); (B) Instantaneous probability density function of the membrane potential at time $t = 79.625ms$ (The upper and lower boundaries of the gray area mark the values one-standard deviation away from the mean, measured from an ensemble of the 10^4 networks. Thick solid line: Kinetic theory (5.19)). Parameters: $f = 0.5$, $\tau = 20ms$ and $\sigma = 0.1ms$, $S = 0.125$ and $p = 0$. [Reproduced from Ref. [22].]

Chapter 6

Concluding Remarks

The primary visual cortex (V1) is one area of the brain where computational modeling has been successfully used to investigate the link between physiological mechanisms and cortical function. Our approach to large-scale computational modeling of V1 [20, 94, 123, 124] has been reviewed in these notes. Clearly, to gain a deeper theoretical understanding of even the simplest brain functions, modeling must strike a careful balance between mathematical abstraction and physiological detail.

To recap, the main objectives of our computational neuronal network modeling were to (i) capture groups of experimentally observed cortical phenomena in a single theoretical model of cortical circuitry, and (ii) identify the physiological mechanisms underlying the resulting model dynamics. In this way, computational modeling with sufficient realism may help to pick from among a number of theoretical scenarios those that could be truly realized in nature. To achieve these objectives, we have built "parsimonious" models based on a minimal, yet sufficient, set of anatomical and physiological assumptions that allow us to qualitatively and quantitatively reproduce a given set of distinct physiological effects within a unified dynamical regime and within a single realistic cortical architecture. A clear advantage of a single large-scale computational model over more idealized models is that it is broad enough to explore a large number of possible dynamical regimes, all within a single framework, and thus identify those regimes that are physiologically relevant. Furthermore, by incorporating longer-range coupling, an extended model can account for the observed spatiotemporal patterns of spontaneous cortical activity [20], and cortical activity patterns induced by the Hikosaka line-motion illusion stimulus paradigm [94].

Furthermore, one of the ultimate goals of large-scale computational neuronal network modeling is to use the network mechanisms identified in computational modeling for guiding the design of new experiments, as well as to contrast these mechanisms with experimental results, so that we can reach a better understanding of the underlying physiological phenomena.

In contrast to statistical physics that provides general principles governing large-scale equilibrium systems, no unifying law has so far been found that would govern

large-scale networks in neuroscience. We have therefore strived to extract the general governing features of the neuronal networks in a robust way that is insensitive to the insignificant details of both the computational model used and the parameter regime it operates in. However, unlike in analytical considerations where this simply means discussing a sufficiently general model family, computational models are very concrete in terms of their specifications, such as the values of parameters used in the model. Therefore, special attention must be paid to the "structural robustness" of the uncovered dynamical mechanisms. In our minds, this means that the models must be able to capture multiple phenomena in a single dynamical regime, within *broad parameter ranges*, and also that the models should capture bifurcations wherever they exist and reproduce their correct dynamical behavior as observed experimentally. These requirements constrain the models structurally. Additionally, in a stronger sense, one can only be reasonably convinced that the network mechanisms discovered via this modeling process are robust structurally when physiologically reasonable variations of the network architecture all reproduce the studied phenomena and confirm the discovered mechanisms in similar parameter regimes.

Moreover, when we study phenomena that are hypothesized to be network induced instead of being controlled by the cellular dynamics of particular neurons, we can demonstrate the robustness of the hypothesized network mechanism by replacing the underlying Hodgkin-Huxley-type equations with, for example, a simpler integrate-and-fire (I&F) neuron model. If the presumed network-induced mechanism is indeed at work, the particular choice of the neuronal equations (Hodgkin-Huxley; Fitzhugh Nagumo; or linear, quadratic, or exponential I&F) should make no essential difference. In fact, a study by comparing a number of such related models can be systematically employed for examining the robustness of the hypothesized mechanisms.

Bibliography

[1] L. Abbott and F. Chance. Rethinking the taxonomy of visual neurons. *Nature Neuroscience*, 5:391–292, 2002.

[2] L.F. Abbott and C. van Vreeswijk. Asynchronous states in networks of pulse-coupled oscillators. *Phys. Rev. E*, 48:1483–1490, 1993.

[3] P. Adorjan, J. Levitt, J. Lund, and K. Obermayer. A model for the intracortical origin of orientation preference and tuning in macaque striate cortex. *Visual Neuroscience*, 16:303–318, 1999.

[4] J.-M. Alonso, W.M. Usrey, and R.C. Reid. Rules of connectivity between geniculate cells and simple cells in cat primary visual cortex. *J. Neurosci.*, 21:4002–4015, 2001.

[5] J. Anderson, I. Lampl, D. Gillespie, and D. Ferster. The contribution of noise to contrast invariance of orientation tuning in cat visual cortex. *Science*, 290:1968–1972, 2000.

[6] A. Angelucci and J. Bullier. Reaching beyond the classical receptive field of V1 neurons: horizontal or feedback axons? *J. Physiol. (Paris)*, 97(2-3):141–154, 2003.

[7] A. Angelucci, J.B. Levitt, P. Adorjan, Y. Zheng, L.C. Sincich, N.P. McLoughlin, G.P. Blasdel, and J.S. Lund. Bar-like patterns of lateral connectivity in layers 4B and upper 4Cα of macaque primary visual cortex, area V1. preprint.

[8] A. Angelucci, J.B. Levitt, E.J. Walton, J.M. Hupe, J. Bullier, and J.S. Lund. Circuits for local and global signal integration in primary visual cortex. *J. Neurosci.*, 22:8633–8646, 2002.

[9] G. Barna, T. Grobler, and P. Erdi. Statistical model of the hippocampal ca3 region, ii. the population framework: model of rhythmic activity in ca3 slice. *Biol. Cybern.*, 79:309–321, 1998.

[10] R. Ben-Yishai, R. Bar-Or, and H. Sompolinsky. Theory of orientation tuning in the visual cortex. *Proc Nat Acad Sci USA*, 92:3844–3848, 1995.

[11] E. Benardete and E. Kaplan. The dynamics of primate M retinal ganglion cells. *Vis Neurosci*, 16:355–368, 1999.

[12] G. Blasdel. Differential imaging of ocular dominance and orientation selectivity in monkey striate cortex. *J. of Neurosci.*, 12:3115–3138, 1992.

[13] G. Blasdel. Orientation selectivity, preference, and continuity in the monkey striate cortex. *J. of Neurosci.*, 12:3139–3161, 1992.

[14] T. Bonhoeffer and A. Grinvald. Iso-orientation domains in cat visual cortex are arranged in pinwheel like patterns. *Nature*, 353:429–431, 1991.

[15] L. Borg-Graham, C. Monier, and Y. Fregnac. Visual input evokes transient and strong shunting inhibition in visual cortical neurons. *Nature*, 393:369–373, 1998.

[16] W.H. Bosking, Y. Zhang, B. Schofield, and D. Fitzpatrick. Orientation selectivity and the arrangement of horizontal connections in tree shrew striate cortex. *J. Neurosci.*, 17:2112–2127, 1997.

[17] P.C. Bressloff. Bloch waves, periodic feature maps, and cortical pattern formation. *Phys. Rev. Lett.*, 89(8):088101–1–088101–4, 2002.

[18] P.C. Bressloff, J.D. Cowan, M. Golubitsky, P.J. Thomas, and M.C. Wiener. Geometric visual hallucinations, euclideansymmetry and the functional architecture of striate cortex. *Phil. Trans. R. Soc. Lond. B*, 356:299–330, 2001.

[19] N. Brunel and V. Hakim. Fast global oscillations in networks of integrate-and-fire neurons with low firing rates. *Neural Comp.*, 11:1621–1671, 1999.

[20] D. Cai, A.V. Rangan, and D.W. McLaughlin. Architectural and synaptic mechanisms underlying coherent spontaneous activity in V1. *Proc. Nat'l Acad. Sci (USA)*, 102:5868–5873, 2005.

[21] D. Cai, L. Tao, and D. W. McLaughlin. An embedded network approach for scale-up of fluctuation-driven systems with preservation of spike information. *Proc. Natl. Acad. Sci. USA*, 101:14288–14293, 2004.

[22] D. Cai, L. Tao, A.V. Rangan, and D.W. McLaughlin. Kinetic theory for neuronal network dynamics. *Commun. Math. Sci.*, 4(1):97–127, 2006.

[23] D. Cai, L. Tao, M. Shelley, and D.W. McLaughlin. An effective representation of fluctuation-driven neuronal networks with application to simple & complex cells in visual cortex. *Pro. Nat. Acad. Sci. (USA)*, 101:7757–7762, 2004.

[24] E. Callaway. Local circuits in primary visual cortex of the macaque monkey. *Ann. Rev. Neurosci.*, 21:47–74, 1998.

[25] E. Callaway and A. Wiser. Contributions of individual layer 2 to 5 spiny neurons to local circuits in macaque primary visual cortex. *Visual Neuroscience*, 13:907–922, 1996.

[26] M. Carandini and D. Ferster. Membrane potential and firing rate in cat visual cortex. *J. Neurosci.*, 20:470–484, 2000.

[27] M. Carandini and D.L. Ringach. Predictions of a recurrent model of orientation selectivity. *Vision Res*, 37(21):3061–3071, 1997.

[28] A. Casti, A. Omurtag, A. Sornborger, E. Kaplan, B. Knight, J. Victor, and L. Sirovich. A population study of integrate-and-fire-or-burst neurons. *Neural Computation*, 14:957–986, 2002.

[29] F. Chance, S. Nelson, and L.F. Abbott. Complex cells as cortically amplified simple cells. *Nature Neuroscience*, 2:277–282, 1999.

[30] T. Chawanya, A. Aoyagi, T. Nishikawa, K. Okuda, and Y. Kuramoto. A model for feature linking via collective oscillations in the primary visual cortex. *Biol. Cybern.*, 68:483–90, 1993.

[31] E. Cinlar. Superposition of point processes. In P.A.W. Lewis, editor, *Stochastic Point Processes: Statistical Analysis, Theory, and Applications*, pages 549–606. Wiley, New York, NY, 1972.

[32] N.W. Daw, P.G.S. Stein, and K. Fox. The role of nmda receptors in information transmission. *Annu Rev Neurosci*, 16:207–222, 1993.

[33] R. De Valois, D. Albrecht, and L. Thorell. Spatial frequency selectivity of cells in macaque visual cortex. *Vision Res*, 22:545–559, 1982.

[34] G. DeAngelis, R. Ghose, I. Ohzawa, and R. Freeman. Functional micro-organization of primary visual cortex: Receptive field analysis of nearby neurons. *J. of Neurosci.*, 19:4046–4064, 1999.

[35] A. Destexhe, M. Rudolph, and D. Pare. The high-conductance state of neocortical neurons in vivo. *Nat. Rev., Neurosci*, 4:730–751, 2003.

[36] R. Everson, A. Prashanth, M. Gabbay, B. Knight, L. Sirovich, and E. Kaplan. Representation of spatial frequency and orientation in the visual cortex. *Proc. Natl. Acad. Sci. USA*, 95:8334–8338, 1998.

[37] D. Ferster and S. Lindstrom. An intracellular analysis of geniculo-cortical connectivity in area 17 of the cat. *J Physiol*, 342:181–215, 1983.

[38] D. Ferster and K.D. Miller. Neural mechanisms of orientation selectivity in the visual cortex. *Annu Rev Neurosci*, 23:441–471, 2000.

[39] D. Fitzpatrick, J. Lund, and G. Blasdel. Intrinsic connections of macaque striate cortex Afferent and efferent connections of lamina 4C. *Journal of Neuroscience*, 5:3329–3349, 1985.

[40] N. Fourcaud and N. Brunel. Dynamics of the firing probability of noisy integrate-and-fire neurons. *Neural Comp.*, 14:2057–2110, 2002.

[41] S. Friedman-Hill, P.E. Maldonado, and C.M. Gray. Dynamics of striate cortical activity in the alert macaque: I. Incidence and stimulus-dependence of gamma-band neuronal oscillations. *Cereb Cortex*, 10(11):1105–1116, 2000.

[42] W. Gerstner. Population dynamics of spiking neurons: Fast transients, asynchronous states, and locking. *Neural Comp.*, 12:43–89, 2000.

[43] C. Gielen, J. van Gisbargen, and A. Ventric. Characterization of spatial and temporal properties of monkey LGN Y-cells. *Bio. Cyber.*, 40:157–170, 1981.

[44] P. Hammond and D.M. MacKay. Differential responsiveness of simple and complex cells in cat striate cortex to visual texture. *Exp Brain Res*, 30(2-3):275–296, 1977.

[45] D. Hansel and C. van Vreeswijk. How noise contributes to contrast invariance of orientation tuning in cat visual cortex. *J. Neurosci.*, 22:5118–5128, 2002.

[46] E. Haskell, D.Q. Nykamp, and D. Tranchina. Population density methods for large-scale modeling of neuronal networks with realistic synaptic kinetics: cutting the dimension down to size. *Network: Compt. Neural. Syst*, 12:141–174, 2001.

[47] J.A. Hirsch and C.D. Gilbert. Synaptic physiology of horizontal connections in the cat's visual cortex. *J. Neurosci.*, 11:1800–1809, 1991.

[48] K.P. Hoffman and J. Stone. Conduction velocity of afferents to cat visual cortex: a correlation with cortical receptive field properties. *Brain Res*, 32(2):460–466, 1971.

[49] D. Hubel and T. Wiesel. Receptive fields, binocular interaction and functional architecture of the cat's visual cortex. *J Physiol (Lond)*, 160:106–154, 1962.

[50] D. Hubel and T. Wiesel. Receptive fields of optic nerve fibres in the spider monkey. *J. Physiol. (Lond)*, 154:572–580, 1962.

[51] D. Hubel and T. Wiesel. Receptive fields and functional architecture of the monkey striate cortex. *J Physiol (Lond)*, 195:215–243, 1968.

[52] M. Hubener, D. Shoham, A. Grinvald, and T. Bonhoeffer. Spatial relationships among three columnar systems in cat area 17. *J. Neurosci.*, 17:9270–9284, 1997.

[53] N.P. Issa, C. Trepel, and M.P. Stryker. Spatial frequency maps in cat visual cortex. *J. Neurosci.*, 20:8504–8514, 2000.

[54] D. Jancke, F. Chavance, S. Naaman, and A. Grinvald. Imaging cortical correlates of illusion in early visual cortex. *Nature*, 428:423–426, 2004.

[55] E. Kaplan, K. Purpura, and R.M. Shapley. Contrast affects the transmission of visual information through the mammalian lateral geniculate nucleus. *J. Physiol.*, 391:267–288, 1987.

[56] E. Kaplan and R. Shapley. X and Y cells in the lateral geniculate nucleus of the macaque monkey. *J.Physiol.*, 330:125–143, 1982.

[57] T. Kenet, D. Bibitchkov, M. Tsodyks, A. Grinvald, and A. Arieli. Spontaneously emerging cortical representations of visual attributes. *Nature*, 425:954–956, 2003.

[58] Z. Kisvarday, E. Toth, M. Rausch, and U. Eysel. Orientation-specific relationship between populations of excitatory and inhibitory lateral connections in the visual cortex of the cat. *Cereb. Cortex*, 7:605–618, 1997.

[59] Z.F. Kisvárday, K.A.C. Martin, T.F. Freund, Z. Magloczky, D. Whitteridge, and P. Somogy. Synaptic targets of HRP-filled layer III pyramidal cells in the cat striate cortex. *Exp. Brain Res.*, 64:541–552, 1986.

[60] B. Knight. Dynamics of encoding in a population neurons. *J. Gen. Physiol.*, 59:734–766, 1972.

[61] B. Knight, D. Manin, and L. Sirovich. Dynamical models of interacting neuron populations. In E. Gerf, editor, *Symposium on Robotics and Cybernetics: Computational Engineering in Systems Applications*. Cite Scientifique, Lille, France, 1996.

[62] C. Koch. *Biophysics of Computation*. Oxford University Press, Oxford, 1999.

[63] A. Kohn and M.A. Smith. Stimulus dependence of neuronal correlation in primary visual cortex of the macaque. *J Neurosci*, 25(14):3661–3673, 2005.

[64] S.W. Kuffler. Discharge patterns and functional organization of the mammalian retina. *J. Neurophysiol.*, 16:37–68, 1953.

[65] C. Monier L. Borg-Graham and Y. Fregnac. Voltage-clamp measurement of visually-evoked conductances with whole-cell patch recordings in primary visual cortex. *J. Physiol Paris*, 90:185–188, 1996.

[66] L. Lapicque. Recherches quantitatives sur l'excitation electrique des nerfs traitee comme une polarization. *Journal de Physiologie et Pathologie Géné ral*, 9:620–635, 1907.

[67] J.S. Lund. Local circuit neurons of macaque monkey striate cortex: Neurons of laminae 4C and 5A. *Journal of Comparative Neurology*, 257:60–92, 1987.

[68] J.S. Lund, A. Angelucci, and P.C. Bressloff. Anatomical substrates for functional columns in macaque monkey primary visual cortex. *Cerebral Cortex*, 12:15–24, 2003.

[69] R. Malach, Y. Amir, M. Harel, and A. Grinvald. Relationship between intrinsic connections and functional architecture revealed by optical imaging and in vivo targeted biocytin injections in primate striate cortex. *Proc. Natl. Acad. Sci. USA*, 90:10469–10473, 1993.

[70] P. Maldonado, I. Godecke, C. Gray, and T. Bonhoeffer. Orientation selectivity in pinwheel centers in cat striate cortex. *Science*, 276:1551–1555, 1997.

[71] P. E. Maldonado, S. Friedman-Hill, and C. M. Gray. Dynamics of striate cortical activity in the alert macaque: II. Fast time scale synchronization. *Cereb Cortex*, 10(11):1117–1131, 2000.

[72] J.G. Malpeli. Activity of cells in area 17 of the cat in absence of input from layer a of lateral geniculate nucleus. *J Neurophysiol*, 49(3):595–610, 1983.

[73] J.G. Malpeli, C. Lee, H.D. Schwark, and T.G. Weyand. Cat area 17. i. pattern of thalamic control of cortical layers. *J Neurophysiol*, 56(4):1062–1073, 1986.

[74] J. Marino, J. Schummers, D. C. Lyon, L. Schwabe, O. Beck, P. Wiesing, K. Obermayer, and M. Sur. Invariant computations in local cortical networks with balanced excitation and inhibition. *Nat. Neurosci.*, 8(2):194–201, 2005.

[75] K.A.C. Martin and D. Whitteridge. Form, function and intracortical projections of spiny neurons in the striate cortex of the cat. *J. Physiol. (London)*, 353:463–504, 1984.

[76] B.A. McGuire, C.D. Gilbert, P.K. Rivlin, and T.N. Wiesel. Targets of horizontal connections in macaque primary visual cortex. *J. Comp. Neurol.*, 305:370–392, 1991.

[77] D. McLaughlin, R. Shapley, M. Shelley, and J. Wielaard. A neuronal network model of macaque primary visual cortex (V1): Orientation selectivity and dynamics in the input layer 4Cα. *Proc. Natl. Acad. Sci. USA*, 97:8087–8092, 2000.

[78] F. Mechler, D. Reich, and J.D. Victor. Detection and discrimination of relative spatial phase by V1 neurons. *J. Neurosci.*, 22:6129–6157, 2002.

[79] F. Mechler and D. Ringach. On the classification of simple and complex cells. *Vis. Res.*, 42:1017–1033, 2002.

[80] M. Mignard and J.G. Malpeli. Paths of information flow through visual cortex. *Science*, 251(4998):1249–1251, 1991.

[81] K. Miller. Synaptic economics: Competition and cooperation in synaptic plasticity. *Neuron*, 17:371–374, 1996.

[82] K. Miller and D. MacKay. The role of constraints in hebbian learning. *Neural Computation*, 6:100–126, 1994.

[83] K. Miller and T. Troyer. Neural noise can explain expansive, power-law nonlinearities in neural response functions. *J. Neurophys.*, 87:653–659, 2002.

[84] S. Molotchnikoff, P.-C. Gillet, S. Shumikhina, and M. Bouchard. Spatial frequency characteristics of nearby neurons in cats' visual cortex. *Neuroscience Letters*, 418(3):242–247, 2007.

[85] J.A. Movshon. The velocity tuning of single units in cat striate cortex. *J Physiol*, 249(3):445–468, 1975.

[86] J. A. Movshon, I. D. Thompson, and D. J. Tolhurst. Receptive field organization of complex cells in the cat's striate cortex. *J Physiol (Lond)*, 283:79–99, 1978.

[87] J. A. Movshon, I. D. Thompson, and D. J. Tolhurst. Spatial summation in the receptive fields of simple cells in the cat's striate cortex. *J Physiol (Lond)*, 283:53–77, 1978.

[88] D. Nykamp and D. Tranchina. A population density method that facilitates large-scale modeling of neural networks: Analysis and application to orientation tuning. *J. of Computational Neuroscience*, 8:19–50, 2000.

[89] D. Nykamp and D. Tranchina. A population density method that facilitates large-scale modeling of neural networks: Extension to slow inhibitory synapses. *Neural Computation*, 13:511–546, 2001.

[90] A. Omurtag, E. Kaplan, B. Knight, and L. Sirovich. A population approach to cortical dynamics with an application to orientation tuning. *Network*, 11:247–260, 2000.

[91] A. Omurtag, B.W. Knight, and L. Sirovich. On the simulation of large populations of neurons. *J. of Comp. Neurosci.*, 8:51–63, 2000.

[92] D. Pare, E. Shink, H. Gaudreau, A. Destexhe, and E.J. Lang. Impact of spontaneous synaptic activity on the resting properties of cat neocortical pyramidal neurons in vivo. *J Neurophysiol*, 79:1450–1460, 1998.

[93] J. Pham, K. Pakdaman, J. Champagnat, and J. Vibert. Activity in sparsely connected excitatory neural networks: effect of connectivity neural networks. *Neural Networks*, 11:415–434, 1998.

[94] A.V. Rangan, D. Cai, and D.W. McLaughlin. Modeling the spatiotemporal cortical activity associated with the line-motion illusion in primary visual cortex. *Proc. Natl. Acad. Sci. USA*, 102(52):18793–18800, 2005.

[95] A.V. Rangan, D. Cai, and L. Tao. Numerical methods for solving moment equations in kinetic theory of neuronal network dynamics. *J. Comput. Phys.*, 221(2):781–798, 2007.

[96] R.C. Reid and J.-M. Alonso. Specificity of monosynaptic connections from thalamus to visual cortex. *Nature*, 378:281–284, 1995.

[97] D. Ringach. Spatial structure and symmetry of simple-cell receptive fields in macaque primary visual cortex. *J. Neurophysiol.*, 88:455–463, 2002.

[98] D. Ringach, M. Hawken, and R. Shapley. Dynamics of orientation tuning in macaque primary visual cortex. *Nature*, 387:281–284, 1997.

[99] D. Ringach, R. Shapley, and M. Hawken. Orientation selectivity in macaque V1: Diversity and laminar dependence. *J. Neuroscience*, 22:5639–5651, 2002.

[100] C. Rivadulla, J. Sharma, and M. Sur. Specific roles of nmda and ampa receptors in direction-selective and spatial phase-selective response in visual cortex. *J. Neurosci.*, 21:1710–1719, 2001.

[101] B. Roerig and J.P. Kao. Organization of intracortical circuits in relation to direction preference maps in ferret visual cortex. *J Neurosci*, 19(24):RC44, 1999.

[102] S. Royer and D. Pare. Bidirectional synaptic plasticity in intercalated amygdala neurons and the extinction of conditioned fear responses. *Neuroscience*, 115:455–462, 2002.

[103] S. Royer and D. Pare. Conservation of total synaptic weight through balanced synaptic depression and potentiation. *Nature*, 422:518–522, 2003.

[104] H. Sato, Y. Hata, and T. Tsumoto. Effects of blocking non-n-methyl-d-aspartate receptors on visual responses of neurons in the cat visual cortex. *Neuroscience*, 94:697–703, 1999.

[105] C.E. Schroeder, D.C. Javitt, M. Steinschneider, A.D. Mehta, S.J. Givre, H.G. Vaughan, Jr., and J.C. Arezzo. N-methyl-D-aspartate enhancement of phasic responses in primate neocortex. *Exp. Brain Res.*, 114:271–278, 1997.

[106] J. Schummers, J. Marino, and M. Sur. Synaptic integration by v1 neurons depends on location within the orientation map. *Neuron*, 36:969–978, 2002.

[107] L. Schwabe, K. Obermayer, A. Angelucci, and P.C. Bressloff. The role of feedback in shaping the extra-classical receptive field of cortical neurons: A recurrent network model. *J. Neurosci.*, 26(36):9117–9129, 2006.

[108] M.N. Shadlen and W.T. Newsome. The variable discharge of cortical neurons: implications for connectivity, computation and information coding. *J Neurosci*, 18:3870–3896, 1998.

[109] R.M. Shapley and J.D. Victor. The effect of contrast on the non-linear response of the y cell. *J. Physiol.*, 302:535–547, 1980.

[110] M. Shelley and D. McLaughlin. Coarse-grained reduction and analysis of a network model of cortical response. I. drifting grating stimuli. *J. Comp. Neurosci.*, 12:97–122, 2002.

[111] M. Shelley, D. McLaughlin, R. Shapley, and J. Wielaard. States of high conductance in a large-scale model of the visual cortex. *J. Comp. Neurosci.*, 13:93–109, 2002.

[112] L. Sincich and G. Blasdel. Oriented axon projections in primary visual cortex of the monkey. *J. Neurosci.*, 21:4416–4426, 2001.

[113] W. Singer and C.M. Gray. Visual feature integration and the temporal correlation hypothesis. *Annu Rev Neurosci.*, 18:555–586, 1995.

[114] W. Singer, F. Tretter, and M. Cynader. Organization of cat striate cortex: a correlation of receptive-field properties with afferent and efferent connections. *J Neurophysiol*, 38(5):1080–1098, 1975.

[115] L. Sirovich and R. Uglesich. The organization of orientation and spatial frequency in primary visual cortex. *Proc Natl Acad Sci U S A*, 101(48):16941–16946, 2004.

[116] B.C. Skottun, R.L. DeValois, D.H. Grosof, J.A. Movshon, D.G. Albrecht, and A.B. Bonds. Classifying simple and complex cells on the basis of response modulation. *Vis. Res.*, 31:1079–1086, 1991.

[117] D. Somers, S. Nelson, and M. Sur. An emergent model of orientation selectivity in cat visual cortical simple cells. *Journal of Neuroscience*, 15:5448–5465, 1995.

[118] D.C. Somers, E.V. Todorov, A.G. Siapas, L.J. Toth, D.S. Kim, and M. Sur. A local circuit approach to understanding integration of long-range inputs in primary visual cortex. *Cereb Cortex*, 8(3):204–217, 1998.

[119] H. Sompolinsky and R. Shapley. New perspectives on the mechanisms for orientation selectivity. *Current Opinion in Neurobiology*, 7:514–522, 1997.

[120] H. Spitzer and S. Hochstein. Simple- and complex-cell response dependences on stimulation parameters. *J.Neurophysiol*, 53:1244–1265, 1985.

[121] E.A. Stern, A.E. Kincaid, and C.J. Wilson. Spontaneous subthreshold membrane potential fluctuations and action potential variability of rat corticostriatal and striatal neurons in vivo. *J. Neurophysiol.*, 77:1697–1715, 1997.

[122] K. Tanaka. Organization of geniculate inputs to visual cortical cells in the cat. *Vis. Res.*, 25:357–364, 1985.

[123] L. Tao, D. Cai, D. McLaughlin, M. Shelley, and R. Shapley. Orientation selectivity in visual cortex by fluctuation-controlled criticality. *Proc. Natl. Acad. Sci. USA*, 103:12911–12916, 2006.

[124] L. Tao, M. Shelley, D. McLaughlin, and R. Shapley. An egalitarian network model for the emergence of simple and complex cells in visual cortex. *Proc Natl Acad Sci U S A*, 101(1):366–371, 2004.

[125] K. Toyama, M. Kimura, and K. Tanaka. Organization of cat visual cortex as investigated by cross-correlation technique. *J Neurophysiol*, 46(2):202–214, 1981.

[126] A. Treves. Mean field analysis of neuronal spike dynamics. *Network*, 4:259–284, 1993.

[127] T. Troyer, A. Krukowski, N. Priebe, and K. Miller. Contrast invariant orientation tuning in cat visual cortex with feedforward tuning and correlation based intracortical connectivity. *J. Neurosci.*, 18:5908–5927, 1998.

[128] M. Tsodyks, T. Kenet, A. Grinvald, and A. Arieli. Linking spontaneous activity of single cortical neurons and the underlying functional architecture. *Science*, 286:1943–1946, 1999.

[129] C. van Vreeswijk and H. Sompolinsky. Chaos in neuronal networks with balanced excitatory and inhibitory activity. *Science*, 274:1724–1726, 1996.

[130] C. van Vreeswijk and H. Sompolinsky. Chaotic balanced state in a model of cortical circuits. *Neural Comput.*, 15:1321–1371, 1998.

[131] J. Wielaard, M. Shelley, R. Shapley, and D. McLaughlin. How Simple cells are made in a nonlinear network model of the visual cortex. *J. Neuroscience*, 21:5203–5211, 2001.

[132] T.N. Wiesel and D.H. Hubel. Spatial and chromatic interactions in the lateral geniculate body of the rhesus monkey. *J. Neurophysiol.*, 29:1115–1156, 1966.

[133] W.J. Wilbur and J. Rinzel. A theoretical basis for large coefficient of variation and bimodality in neuronal interspike interval distributions. *J. Theor. Biol*, 105:345–368, 1983.

[134] H. Wilson and J. Cowan. A mathematical theory of the functional dynamics of cortical and thalamic nervous tissue. *Kybernetik*, 13:55–80, 1973.

[135] D. Xing, R.M. Shapley, M.J. Hawken, and D.L. Ringach. Effect of stimulus size on the dynamics of orientation selectivity in Macaque V1. *J Neurophysiol*, 94(1):799–812, 2005.

[136] Y. Yoshimura, H. Sato, K. Imamura, and Y. Watanabe. Properties of horizontal and vertical inputs to pyramidal cells in the superficial layers of the cat visual cortex. *J Neurosci*, 20:1931–1940, 2000.

[137] T. Yoshioka, G. Blasdel, J. Levitt, and J. Lund. Relation between patterns of intrinsic lateral connectivity, ocular dominance, and cytochrome oxidase-reactive regions in macaque monkey striate cortex. *Cereb. Cortex*, 6:297–310, 1996.

Stochastic processes and PDEs in mathematical biology

Juan J.L. Velázquez

Max-Planck-Institut
für Mathematik
in den Naturwissenschaften
Leipzig

Qualitative behavior of a Keller-Segel model with non-diffusive memory

by

Kyungkeun Kang, Angela Stevens, and Juan J.L. Velazquez

Preprint no.: 35 2008

Plan of the course.

Program

Systems with many particles. Interacting particle systems: How to describe using a reduced number of variables the dynamics of a system of many particles in suitable asymptotic limits.

Questions to be considered for interacting particle systems.

(i) Mean-field theories. Oelschlager results. Derivation of the KS model taking as a starting point a particle model.

(ii) Self-interacting particle systems with non-diffusive interactions. (Othmer-Stevens model).

(iii) Hydrodynamic limits of stochastic systems. (Luckhaus-Triolo model).

(iv) Kinetic equations. Examples

Lecture 1:

Introduction: On the motion of brownian particles: Independent particles: Discrete equations describing the evolution of individual particles. Diffusion equation. (Solution of the discrete problem in some simple cases). Drifting.

Continuous stochastic processes. Brownian motion. (Wiener measure). Local times. Ray-Knight theorems.

Lecture 2:

Interacting particle systems interacting by means of pair-potentials. Mean field theories:

(i) Deterministic case. (1D case). The Porous Medium Equation as limit.

(ii) Stochastic case. Limit equation. (Including the higher dimensional case).

(iii) Steven's results. Derivation of the KS limit in the mean-field limit case.

(iv) Open problems: Oeschlager problem in the higher dimensional deterministic case.

Lecture 3:

Systems with non-diffusive interactions:
(i) Reinforced random walks. (Self-interacting particle systems).
(ii) Mean-field approach: The Othmer-Stevens model. (Derivation).
(iii) Some mathematical results for the Othmer-Stevens model.
(iv) Which limit of particles gives the Othmer-Stevens model?.

Lecture 4:
Hydrodynamic limits

(i) Basic ideas in hydrodynamic limits: Local equilibrium with slowly varying parameters.
(ii) Oeschlager problem: Deterministic case in the hydrodinamic regime.
(iii) The Luckhaus-Triolo model: A tumour model with two time scales.

Examples of kinetic models in biological problems: (Amoeba like movements, alignment models).

IOP PUBLISHING NONLINEARITY

Nonlinearity **21** (2008) T283–T289 doi:10.1088/0951-7715/21/12/T04

OPEN PROBLEM

Partial differential equations and non-diffusive structures

A Stevens[1] **and J J L Velázquez**[2]

[1] Universität Heidelberg, Angewandte Mathematik und Bioquant, INF 267, D-69120 Heidelberg, Germany
[2] ICMAT (CSIC-UAM-UC3M-UCM), Facultad de Matemáticas, Universidad Complutense, Madrid 28040, Spain

E-mail: angela.stevens@uni-hd.de and velazque@mat.ucm.es

Received 15 September 2008, in final form 24 September 2008
Published 13 November 2008
Online at stacks.iop.org/Non/21/T283

Abstract
In this paper we give a short introduction to open problems and recent studies of classes of partial differential equations, which—in contrast to reaction–diffusion systems—describe phenomena with local interactions. Partial differential equations coupled with ordinary differential equations, models of transport type and hyperbolic systems are discussed with respect to their pattern forming behaviour.

Mathematics Subject Classification: 35K55, 45K05, 35L60, 35B10, 35B40, 82C70, 92C15, 92C17

1. Introduction

In the following we summarize some models of partial differential equations, which are characterized by the presence of at least one non-diffusible 'active agent'. We are interested in the pattern forming behaviour and the long time dynamics of such systems. From the applied point of view we will focus on biological examples and models here, although the mathematical questions we address also arise in other scientific contexts. From the mathematical point of view it turns out that the solutions of these models show peculiar patterns in comparison with mathematical models, where most agents in the system are assumed to diffuse. This latter type of systems and equations has been studied in mathematical biology in great detail, especially in the context of Turing type instabilities. The analysis of the 'more local' models requires different mathematical methods and techniques.

2. Reaction–diffusion equations coupled to ODEs

One example for a model of an interacting cell system whose continuous reaction–diffusion limit is given by a reaction–diffusion equation coupled to an ODE is the model for loss of

contact inhibition of malignant cells within a healthy tissue, proposed and analysed in [3, 17]. Two types of cells, malignant and healthy ones, move and divide on a two-dimensional lattice. The malignant cells, denoted by U, are supposed to be more motile and thus diffuse on the lattice much faster than the healthy cells, denoted by V. In the case of cell–cell contact the healthy cells are inhibited to grow, whereas the malignant cells can still grow in such a situation. Thus the malignant cells are able grow on top of other cells, i.e. the birth rate of U is assumed to be constant. The healthy V cells can only grow on empty sites. The death rate for all cells of type U and of type V increases with local overcrowding, since they are assumed to compete, e.g. for oxygen. In [3, 17] the following system of partial differential equations was rigorously derived for the macroscopic cell densities u, v by means of a hydrodynamic limit:

$$u_t = \Delta u + u(\beta - D(u) - D'(u)v),$$

$$v_t = v(\beta(1 - v)\exp(-u) - D(u)).$$

Here $D(u) = \sum_{k=0}^{\infty} \gamma(k+1)\frac{u^k}{k!}\mathrm{e}^{-u}$ and γ relate to the death processes in the original interacting stochastic many particle models and β relates to the birth rate (cf [17]). The diffusion of the V cells vanishes in this limit.

An interesting question for this limiting system is, what are the qualitative dynamics of the populations of malignant and of healthy cells, i.e. under what conditions does one of the cell populations spread faster than the other within the heterogeneous tissue. A first result was given in [17]. Related questions were pursued in [8].

3. Drift–diffusion models coupled to an ODE

A by now classical drift–diffusion model, respectively, cross-diffusion model in mathematical biology is the Keller–Segel (KS) model for chemotaxis [14]. Cells exhibiting chemotaxis move towards regions of higher concentrations of an attractive chemical signal. Well-known examples are the chemotactic behaviour of *Escherichia coli* and of the slime mould amoebae *Dictyostelium discoideum*.

Two particularly interesting limiting cases of the KS model exist. First, the case where the diffusion of the chemotactic species is much slower than the diffusion of the chemo-attractant. In suitable non-dimensional units the model then reduces to a parabolic–elliptic system:

$$u_t = \Delta u - \nabla(u\nabla v), \qquad x \in \Omega \in \mathbb{R}^N, \quad t > 0, \tag{1}$$

$$0 = \Delta v + u - c \qquad x \in \Omega, \quad t > 0. \tag{2}$$

Here $u = u(t, x)$ denotes the concentration of the chemotactic organism and $v = v(t, x)$ denotes the concentration of the chemo-attractant. This system is usually stated with zero-flux boundary conditions for a bounded domain Ω and initial data $u(0, x) = u_0(x)$. A compatibility condition which allows to solve (2) with zero-flux conditions is given by $c = \frac{1}{|\Omega|}\int_\Omega u_0 \,\mathrm{d}x$.

The mathematical properties of system (1) and (2) have been studied extensively, in particular steady states and conditions for initial data which ensure the global existence of solutions or blow-up in finite time. The number of papers on the KS model and related systems is rather large by now. A summary of the results on this topic in published papers and preprints until 2002 can be found in [9, 10].

So far a second interesting limiting case for the KS type of models has been studied much less. Instead of a diffusible chemo-attractant a kind of non-diffusible attractive memory is

assumed to be given:

$$u_t = \Delta u - \nabla(u \nabla g(z)), \qquad x \in \Omega \subset \mathbb{R}^N, \quad t > 0, \tag{3}$$

$$z_t = f(u, z). \tag{4}$$

For specific positive g and negative f chemotactic travelling bands were already discussed in [15], see also [11] and further references therein. In [23] and [2] the existence of global solutions for such models was proved.

Mathematically the situation becomes more involved for positive f. A specific example for system (3) and (4) with $g(z) = \theta \log(z)$ for $\theta > 0$ and $f(u, z) = u$ was introduced in [18, 24]. The idea for this model originated from a self-attracting reinforced random walk of a single particle, the derivation of conditions for recurrence and transience and the biological phenomenon of slime trail following and aggregation of myxobacteria (cf the review paper [19] for reinforced random walks and the book [4] for the self-organization of myxobacteria).

The PDE model (3) and (4) cannot provide an accurate description of the dynamics of the self-attracting reinforced random walk of a single particle in any nontrivial continuum limit. However, it seems likely that for a many particle model this PDE–ODE system results as a limit under suitable conditions on the number of particles and the law of reinforcement. Nevertheless, the rigorous derivation of (3) and (4) starting from a stochastic many particle system has not been obtained so far. In case equation (4) also allows diffusion, a rigorous derivation of the system from a moderately interacting stochastic many particle system has been obtained in [25].

For $f(u, z) = u \cdot z$ and $g(z) = \log(z)$ blow-up in finite time in one space dimension for specific initial data was proved in [16]. These functions give rise to a much stronger tendency for blow-up of solutions than the case $f(u, z) = u$ and $g(z) = \theta \log(z)$ for any $\theta > 0$. Therefore, the asymptotic behaviour of the solutions of (3) and (4) for $f(u, z) = u$ and $g(z) = \theta \log(z)$ for different space dimensions has recently been studied in [26] in more detail. Results include blow-up in finite time, blow-up in infinite time and convergence of solutions to zero in a self-similar way. Most of these solutions exhibit involved asymptotics, which require a careful analysis of several boundary layers. As a general rule *larger* values of θ and *smaller* values of the spatial dimension N yield a stronger tendency for blow-up. As a consequence, many critical parameter values occur for which the solutions change their asymptotic behaviour.

The asymptotics given in [26] do not yield blow-up for $\theta < 1$ in any space dimension. Given the form of equation (3) one can expect an increasing strength of the chemotactic attraction for increasing θ. The dependence of the behaviour of (3) and (4) on the space dimension N is not so obvious and requires a more detailed analysis than what is shown so far in [26]. An intuitive explanation for the dependence of blow-up on the spatial dimension is as follows: for smaller dimensions the motion of a Brownian particle covers space more densely than for larger dimensions. As a consequence, the modification of the environment (given by v) is smaller for larger dimensions and therefore the tendency for blow-up is weaker. Blow-up results from steepening gradients in the attractive environment v. In the case of a diffusing chemical environment v the result is different. Then the tendency for blow-up of solutions is stronger in larger dimensions.

Due to the hyperbolic character of equation (4) the asymptotics of the solutions of (3) and (4) depend very sensitively on the initial data in some cases. The strongest dependences occur for $N = 1, \theta = 1$. This has been rigorously proved in [13]. Also the concentration of mass to a Dirac mass in infinite time has been shown for the case $N = 1$, $1 < \theta < 3$.

It would be interesting to obtain rigorous proofs for various other asymptotic results derived in [26] and to understand them in a more general context.

4. Models of transport type

Models of transport type are extensively studied in the context of age and stage structured population dynamics, especially in epidemiology. Usually the dynamics of a distribution function $f = f(t, x, \theta)$ is described with respect to time, space and a set of internal variables or age/stage parameters θ. These variables can include magnitudes such as cell orientation or shape, the state within the cell cycle, age with respect to a disease state and magnitudes for internal cell states, such as chemical concentrations. Depending on the setting, f can be understood as a cell density or a probability distribution. Examples are given in [27] and [20]. Further classical references are cited in these books.

An example for a transport model analysed in mathematical biology is

$$(\partial_t f + v(\theta) \cdot \nabla_x f)(t, x, \theta) = \int_{[-1,1]} [K(\hat{\theta}, \theta; f) f(t, x, \hat{\theta}) - K(\theta, \hat{\theta}; f) f(t, x, \theta)] \, \mathrm{d}\hat{\theta}. \tag{5}$$

The left-hand side of this equation describes cell motion with speed $v(\theta)$, which may depend on the set of internal variables θ. The right-hand side describes the transition between different cell states. More generally derivatives with respect to θ could also be included and further dependences considered. Equations such as (5) have been used to study reorientation of cells due to interaction with themselves and with external cues. In the context of chemotaxis (cf [1]) the kernel K depends on an external attractive chemical signal instead of (or additionally to) f itself. For alignment of small stiff filaments and elongated cells equation (5) was discussed in [5] and [7], but cell motion in space was omitted.

The fact that the changes in the internal variables take place locally, i.e. in regions of a size which is smaller than the characteristic length scale used to define the distribution $f(t, x, v)$, justifies the discussion of equation (5) together with the other type of models presented in this paper.

4.1. Pattern formation in transport models with internal variables

An interesting feature of models of type (5) is that they can generate patterns with a characteristic wavelength. This is well known for reaction–diffusion systems and was discovered in the classical work by Turing [28]. The existence of pattern forming instabilities for (5) has been proved in [21] for a discrete set of state variables. The linearization of equations of type (5) can exhibit periodic oscillations with a characteristic wavelength, if at least three state variables are present. It has also been proved that the formation of nontrivial patterns is possible with at least four internal variables, if the resulting system is symmetric under reflections. The basic model in this case is

$$\begin{aligned}
(u_1)_t + \alpha(u_1)_x &= S_2(u_1, u_2, v_1, v_2) - T_1(u_1, u_2, v_1, v_2),\\
(u_2)_t + \beta(u_2)_x &= T_1(u_1, u_2, v_1, v_2) - T_2(u_1, u_2, v_1, v_2),\\
(v_1)_t - \alpha(v_1)_x &= T_2(u_1, u_2, v_1, v_2) - S_1(u_1, u_2, v_1, v_2),\\
(v_2)_t - \beta(v_2)_x &= S_1(u_1, u_2, v_1, v_2) - S_2(u_1, u_2, v_1, v_2).
\end{aligned}$$

Under suitable conditions on α, β, T_1, T_2 and S_1, S_2 the solutions of the linearized system show patterns with a defined wavelength.

These results can be interpreted in analogy to Turing's results. Nontrivial patterns are possible in reaction–diffusion systems only if they are complex enough. Linear systems with

one diffusing chemical cannot generate patterns, but—as Turing proved—this is possible if at least two different chemicals with different diffusion coefficients are involved. In the case of systems of type (5) the patterns are generated by a nontrivial coupling of the cell motility with the dynamics of the internal cell variables.

The models discussed in [21] are motivated by the peculiar counter migrating periodic wave-like patterns—or ripples—in cultures of myxobacteria (cf [4]). After alignment these bacteria move in a nearly one-dimensional manner, basically in two directions, and reverse upon contact after the exchange of a signal. It was proved in [21] that models with 'reasonable' functional dependences can reproduce the experimentally described ripples, if they contain three internal cell states for the cells moving in the same of the two possible directions, which means overall six equations for the full system. This result indicates that a minimal amount of complexity is required for such a system with local interaction to create the requested patterns. Of course more research is needed to clarify if and how the observed biological phenomenon relates to the models suggestions, i.e. what could be the mechanics of the different cell states. An additional test for the model is the experimental observation that the wavelength of the periodic pattern increases and finally disappears, if a specific type of mutants is added to the culture, namely, bacteria which are unable to submit the signal for reversal to their neighbours which are in direct contact with themselves. The suggested model together with the natural extension for the mutant population perfectly reflects this qualitative feature mathematically (cf [21]).

In [21] mathematical methods have been developed to study classes of equations of type (5) which generate patterns. A more systematic classification of such models is still open to do. It would also be interesting to study analogous effects for nonlinear problems. The analysis of pattern formation for nonlinear systems has been done for reaction–diffusion systems. Such results are lacking so far for nonlinear versions of the equations discussed in [21]. This seems interesting to analyse from the mathematical point of view.

4.2. Alignment in transport models

Models of type (5) were also discussed in [5] to study alignment of small, stiff filaments or elongated bacteria, namely

$$\partial_t f(t,\theta) = \int_{[-1,1]} [K(\hat{\theta},\theta;\, f) f(t,\hat{\theta}) - K(\theta,\hat{\theta};\, f) f(t,\theta)]\, \mathrm{d}\hat{\theta} \tag{6}$$

with

$$K(\theta,\hat{\theta};\, f) = \int_{[-1,1]} G_\sigma(\hat{\theta} - M_w(\theta)) f(t,w)\, \mathrm{d}w,$$

where G_σ is the standard periodic Gaussian

$$G_\sigma(u) = (4\pi\sigma)^{-1/2} \sum_{m\in\mathbb{Z}} \exp(-(u+2m)^2/(4\sigma)), \tag{7}$$

$M_w(\theta) = \theta + V(w-\theta)$ is the optimal reorientation due to interaction of bundles of filaments with those of orientation w, and V is the orientational angle. Here $\sigma = 0$ is a limiting case, where G_σ is the Dirac mass. Uniform convergence of solutions for $\sigma \to 0$ was established in [6].

In [5] and [7] involved bifurcation results for steady state solutions of (6) were obtained. In [12] and [22] the full equation was rigorously analysed. In [12] the model for deterministic

alignment mechanisms, namely, $\sigma = 0$, was studied. It was rigorously proved that for a specific class of initial data the solutions of the equation do align the filament bundles along two opposite directions. Nevertheless, the amount of mass aligning for each of the opposite directions turned out to be arbitrary. This is due to the deterministic character of the model. In [22] it was proved that in the presence of stochastic effects on the alignment mechanism, namely, $\sigma > 0$, mass selection results and only two values for the ratio between the masses aligning in opposite directions are possible. Either identical masses are aligned in the two directions, or most of the mass is concentrated in only one direction. Which of the two cases occurs depends on the specific form of the interaction given by V, as discussed in [22].

The results in [12] and [22] are basically local results and have been derived either for specific initial distributions or under suitable smallness conditions for the intensity of the stochasticity, the strength of the interactions for alignment, and others. It would be interesting to clarify the necessity of these restrictions.

The analysis in [5, 7, 12, 22] is restricted to spatially homogeneous situations. How additional spatial dependences do affect the system is largely open.

References

[1] Alt W 1981 Singular perturbation of differential integral equations describing biased random walks *J. Reine Angew. Math.* **322** 15–41

[2] Corrias L, Perthame B and Zaag H 2004 Global solutions of some chemotaxis and angiogenesis systems in high space dimensions *Milan J. Math.* **72** 1–28

[3] De Masi A, Luckhaus S and Presutti E 2007 Two scales hydrodynamic limit for a model of malignant tumour cells *Ann. Inst. H. Poincaré Probab. Statist.* **43** 257–97

[4] Dworkin M and Kaiser D (ed) 1993 *Myxobacteria II* (American Society for Microbiology Press)

[5] Geigant E 1999 Nichtlineare Integro-Differential-Gleichungen zur Modellierung interaktiver Musterbildungsprozesse auf $\mathbb{S}^1$ *PhD Thesis* Bonn University *Bonner Mathematische Schriften* vol 323 (Bonn University)

[6] Geigant E 2000 Stability analysis of a peak solution of an orientational aggregation model *EQUADIFF 99: Proc. Int. Conf. on Differential Equation (Berlin)* vol 2 (Singapore: World Scientific) pp 1210–16

[7] Geigant E and Stoll M 2003 Bifurcation analysis of an orientational aggregation model *J. Math. Biol.* **46** 537–63

[8] Heinze S and Schweitzer B 2005 Creeping fronts in degenerate reaction–diffusion systems *Nonlinearity* **18** 2455–76

[9] Horstmann D 2003 From 1970 until present: the Keller–Segel model in chemotaxis and its consequences: I *Jahresber. Deutsch. Math.-Verein.* **105** 103–65

[10] Horstmann D 2004 From 1970 until present: the Keller–Segel model in chemotaxis and its consequences: II *Jahresber. Deutsch. Math.-Verein.* **106** 51–69

[11] Horstmann D and Stevens A 2004 A constructive approach to travelling waves in chemotaxis *J. Nonlinear Sci.* **14** 1–25

[12] Kang K, Perthame B, Stevens A and Velázquez J J L 2008–2009 An integro-differential equation model for alignment and orientational aggregation *J. Diff. Eqns* at press

[13] Kang K, Stevens A and Velázquez J J L 2008 Qualitative behaviour of a Keller–Segel model with non-diffusive memory *Max-Planck-Institute for Mathematics in the Sciences, Leipzig, Germany*, *Preprint* 35 *Commun. Partial Diff. Eqns* submitted

[14] Keller E F and Segel L A 1970 Initiation of slime mold aggregation viewed as an instability *J. Theor. Biol.* **26** 399–415

[15] Keller E F and Segel L A 1971 Travelling bands of chemotactic bacteria: a theoretical analysis *J. Theor. Biol.* **30** 235–48

[16] Levine H and Sleeman B 1997 A system of reaction diffusion equations arising in the theory of reinforced random walks *SIAM J. Appl. Math.* **57** 683–730

[17] Luckhaus S and Triolo L 2004 The continuum reaction–diffusion limit of a stochastic cellular growth model *Rend. Mat. Ac. Lincei* s.9 **15** 215–23

[18] Othmer H G and Stevens A 1997 Aggregation, blow-up and collapse. The ABC's of taxis in reinforced random walks *SIAM J. Appl. Math.* **57** 1044-81

[19] Pemantle R 2007 A survey of random processes with reinforcement *Probab. Surv.* **4** 1–79

[20] Perthame B 2007 *Transport Equations in Biology, Frontiers in Mathematics* (Basle: Birkhäuser)
[21] Primi I, Stevens A, Velázquez J J L Pattern forming instabilities driven by non-diffusive interaction *Preprint*
[22] Primi I, Stevens A and Velázquez J J L 2007 Mass-selection in alignment models with non-deterministic effects *Max-Planck-Institute for Mathematics in the Sciences, Leipzig, Germany*, *Preprint* 34 *Commun. Partial Diff. Eqns* submitted
[23] Rascle M 1979 Sur une équation intégro-différentielle non linéaire issue de la biologie *J. Diff. Eqns* **32** 420–53
[24] Stevens A 1995 Trail following and aggregation of myxobacteria *J. Biol. Syst.* **3** 1059–68
[25] Stevens A 2000 The derivation of chemotaxis equations as limit dynamics of moderately interacting stochastic many-particle systems *SIAM J. Appl. Math.* **61** 183–212
[26] Stevens A and Velázquez J J L Asymptotics study of a partial differential equation system motivated by reinforced random walks *Preprint*
[27] Thieme H 2003 *Mathematics in Population Biology* (*Princeton Series in Theoretical and Computational Biology*) (Princeton: Princeton University Press)
[28] Turing A 1952 The chemical basis of morphogenesis *Phil. Trans. R. Soc.* B **237** 37–72

Qualitative behavior of a Keller-Segel model with non-diffusive memory

Kyungkeun Kang*, Angela Stevens†, Juan J. L. Velázquez‡

Abstract

In this paper a one-dimensional Keller-Segel model with a logarithmic chemotactic-sensitivity and a non-diffusing chemical is classified with respect to its long time behavior. The strength of production of the non-diffusive chemical has a strong influence on the qualitative behavior of the system concerning existence of global solutions or Dirac-mass formation. Further, the initial data play a crucial role.

1 Introduction

We consider a chemotaxis-system with a logarithmic chemotactic sensitivity and a non-diffusing chemical. The main question addressed is whether smooth solutions exist globally in time, or blowup happens. A crucial assumption is that the chemical is produced by the chemotactic species and decay terms do not occur. Thus a drift-diffusion equation is coupled to an ODE. In [5] Keller and Segel discussed traveling waves for a similar system, where for the chemical reaction kinetics just a decay term is considered. Thus existence of global solutions can always be expected. When varying the strength of the production an interesting long time behavior can be expected for the system, as introduced in [11] and formally explored in [8]. Existence of global solutions for linear production kinetics with respect to the chemotactic species was proved in [13]. For a fixed and strong production kinetics in [6] finite time blowup was shown for specific explicit initial data.

In this paper we classify the system for a variety of production kinetics and types of initial data. The aim is to find "critical conditions" for the switch between existence of global solutions and Dirac mass formation.

The system we study is

$$u_t = u_{xx} - \left(u\frac{w_x}{w}\right)_x, \qquad w_t = uw^\lambda \quad \text{for } t>0,\ x\in I=[0,\pi], \quad \text{and} \quad \lambda\in[0,1)\,,$$

*Department of Mathematics, Sungkyunkwan University and Institute of Basic Science, Suwon 440-746, Republic of Korea (kkang@skku.edu)

†University of Heidelberg, Applied Mathematics and Bioquant, BQ 0021, INF 267, D-69120 Heidelberg, Germany (angela.stevens@uni-hd.de)

‡Departamento de Matemática Aplicada, Facultad de Ciencias Matemáticas, 28040 Madrid, Spain (JJ_Velazquez@mat.ucm.es)

with periodic boundary conditions. Here u models the chemotactic species and w the non-diffusive memory. By setting $\theta = \frac{1}{1-\lambda}$ and $z = w^{\frac{1}{\theta}}$ we obtain

$$u_t = u_{xx} - \theta \left(u \frac{z_x}{z} \right)_x , \qquad z_t = u \quad \text{for } t > 0,\ x \in I = [0, \pi] . \tag{1}$$

So $\theta \in [1, \infty)$. In [13] a result for $\lambda = 0$, respectively $\theta = 1$ was obtained. In [6] a result for $\lambda = 1$ was given. We will have a closer look at the regime in between, where the interesting switch from the existence of global solutions toward Dirac mass formation is to be expected.

Throughout this paper we will use the following notation for the functional spaces for given $t > 0$:

$$H^k = H^k(I) = \{\, f(t,\cdot) :\ D_j f(t,\cdot) \in L^2(I),\ 0 \le j \le k \,\}.$$

2 Qualitative behavior of system for $\theta = 1$:

In this section C will always denote a generic constant that can change from line to line. We will show that there exist global smooth solutions for system (1) with periodic boundary conditions. In [13] an L^∞-estimate was proved for this case.

First note that $u(x,t) = a$ and $z(x,t) = at + b$ with $a, b > 0$ are homogeneous solutions of

$$u_t = u_{xx} - \left(u \frac{z_x}{z} \right)_x , \qquad z_t = u \quad \text{for } t > 0,\ x \in I = [0, \pi].$$

For convenience, define $\bar{z}(t) = at + b$. We will first study the stability for this problem. Due to translation, e.g. $\tau = t + \frac{b}{a}$, one can assume w.l.o.g. that $t \ge \frac{b}{a}$, so $\bar{z}(t) = at$. For simplicity, we set $a = b$. Our main result of this section is

Theorem 2.1 *Let (a, at) be a space-independent solution of (1), where $a > 0$ is constant. If (u, z) is a solution with initial data (u_0, z_0) sufficiently close to (a, a), then there exists $v_\infty \in H^2$ such that u and $\frac{z}{t}$ both converge to $a + v_\infty$ for $t \to \infty$.*

We need several steps to prove this theorem. So we are looking for solutions of type

$$u(x,t) = a + v(x,t), \qquad z(x,t) = \bar{z}(t) + \zeta(x,t) . \tag{2}$$

Assume that $v_0(x) = v(x,1)$ and $\zeta_0(x) = \zeta(x,1)$ are "sufficiently" small and regular. Further details will be specified later. Substituting (2) into (1), we have

$$v_t = v_{xx} - \left((a+v) \frac{\zeta_x}{\bar{z} + \zeta} \right)_x = v_{xx} - \left(\frac{1}{t} \zeta_x \right)_x - \left(\frac{\zeta_x}{\bar{z} + \zeta} v - \frac{a \zeta \zeta_x}{\bar{z}(\bar{z} + \zeta)} \right)_x , \quad \zeta_t = v. \tag{3}$$

Also we will consider the Fourier-expansion

$$v(x,t) = \sum_{n=-\infty}^{\infty} v_n(t) e^{inx}, \quad \zeta(x,t) = \sum_{n=-\infty}^{\infty} \zeta_n(t) e^{inx}.$$

2.1 The linearized problem

First we linearize system (3) around the homogenous solutions and obtain

$$v_t = v_{xx} - \frac{1}{t}\zeta_{xx} \ , \quad \zeta_t = v \ , \quad \text{in } \ I = [0,\pi] \ . \tag{4}$$

We show that the space-independent solution (a, at) of (3) is stable on the linearized level.

Proposition 2.2 *Let (v,ζ) be a solution of (4). There exist $\epsilon > 0$ and $\delta = \delta(\epsilon)$ such that for $\|v(1)\|_{H^2} + \|\zeta(1)\|_{H^2} < \delta$ one obtains $\|v(t)\|_{H^2} \le \epsilon$ and $\|\zeta(t)\|_{H^2} \le \epsilon t$ for all $1 \le t < \infty$. Moreover, there exists $v_\infty \in H^2$ with*

$$\int_\Omega v_\infty e^{inx} dx = \zeta_n(1) - (\zeta_n(1) - v_n(1)) \int_1^\infty \frac{e^{n^2(1-s)}}{s^2} ds$$

such that

$$\|v(t) - v_\infty\|_{H^2} \ , \quad \left\| \frac{\zeta(t)}{t} - v_\infty \right\|_{H^2} \ \longrightarrow \ 0 \quad \textit{as} \ \ t \to \infty.$$

Proof. The Fourier coefficients of v and ζ must satisfy

$$v_n'(t) = -n^2 v_n(t) + \frac{1}{t} n^2 \zeta_n(t), \qquad \zeta_n'(t) = v_n(t).$$

Therefore,

$$\zeta_n''(t) = -n^2 \zeta_n'(t) + \frac{1}{t} n^2 \zeta_n(t).$$

Solving this ODE, we get

$$\zeta_n(t) = A_n t + B_n t \int_t^\infty \frac{e^{-n^2 s}}{s^2} ds, \quad v_n(t) = A_n + B_n \int_t^\infty \frac{e^{-n^2 s}}{s^2} ds - \frac{B_n}{t} e^{-n^2 t}, \tag{5}$$

where

$$A_n = \zeta_n(1) - (\zeta_n(1) - v_n(1)) \int_1^\infty \frac{e^{n^2(1-s)}}{s^2} ds, \quad B_n = e^{n^2} \left(\zeta_n(1) - v_n(1)\right).$$

Formula (5) is valid also for $n = 0$, in which case $\zeta_0(t) = A_0 t + B_0$ and $v_0(t) = A_0$. Due to the assumptions on the initial conditions, we have $\sum_{n=-\infty}^{\infty} (1+n^4) \left(|v_n(1)|^2 + |\zeta_n(1)|^2 \right) < \delta^2$, and for all $n \in \mathbb{Z}$ we have $v_n - \zeta_n/t = -B_n e^{-n^2 t}/t$. Thus, direct computations show that

$$\left\| v - \frac{\zeta}{t} \right\|_{H^2}^2 \le \sum_{n=-\infty}^{\infty} (1+n^4) B_n^2 \frac{e^{-2n^2 t}}{t^2} = \sum_{n=-\infty}^{\infty} (1+n^4) \left|\zeta_n(1) - v_n(1)\right|^2 \frac{e^{2n^2(1-t)}}{t^2}$$

$$\le \frac{\|\zeta(1) - v(1)\|_{H^2}^2}{t^2} < \frac{\delta^2}{t^2} \ .$$

It is straightforward that

$$\sum_{n=-\infty}^{\infty}(1+n^4)A_n^2 \le C\sum_{n=-\infty}^{\infty}(1+n^4)\left(|v_n(1)|^2+|\zeta_n(1)|^2\right) \le C\delta^2\,,$$

and for any t with $1 \le t < \infty$ we have

$$\sum_{n=-\infty}^{\infty}(1+n^4)B_n^2\left(\int_t^\infty \frac{e^{-n^2 s}}{s^2}ds\right)^2 \le \sum_{n=-\infty}^{\infty}(1+n^4)(\zeta_n(1)-v_n(1))^2\left(\int_t^\infty \frac{e^{n^2(1-s)}}{s^2}ds\right)^2$$

$$\le \sum_{n=-\infty}^{\infty}(1+n^4)(\zeta_n(1)-v_n(1))^2\frac{1}{t^2} < \frac{\delta^2}{t^2}.$$

Summing up all estimates, we obtain

$$\|v\|_{H^2}^2 \le \sum_{n=-\infty}^{\infty}(1+n^4)\left[A_n^2+B_n^2\left(\int_t^\infty \frac{e^{-n^2 s}}{s^2}ds\right)^2+B_n^2\frac{e^{-2n^2 t}}{t^2}\right] \le C\delta^2, \quad 1 \le t < \infty$$

and

$$\|v-v_\infty\|_{H^2}^2 = \sum_{n=-\infty}^{\infty}(1+n^4)\left[B_n^2\left(\int_t^\infty \frac{e^{-n^2 s}}{s^2}ds\right)^2+B_n^2\frac{e^{-2n^2 t}}{t^2}\right] \le C\frac{\delta^2}{t^2}.$$

This completes the proof. □

2.2 Nonlinear stability

Let $f(x,t)$ be the nonlinear part of (3) and let f_n denote the n-th Fourier coefficient of f, namely

$$f(x,t) = -\left(\frac{\zeta_x}{\bar{z}+\zeta}v - \frac{a\zeta\zeta_x}{\bar{z}(\bar{z}+\zeta)}\right)_x = -\left(\frac{\zeta_x}{\bar{z}+\zeta}(v-\frac{\zeta}{t})\right)_x, \quad f_n(t) := (f(x,t), e^{inx}).$$

Recalling (3) and comparing Fourier coefficients, we have

$$\zeta_n''(t) + n^2\zeta_n'(t) - \frac{1}{t}n^2\zeta_n(t) = f_n(t). \tag{6}$$

By setting $\zeta_n(t) = t\Phi_n(t)$, we get

$$\Phi_n'(t) = \frac{e^{-n^2 t}}{t^2}\int_1^t f_n(s)se^{n^2 s}ds. \quad \text{So}\,, \quad \Phi_n(t) = \int_1^t \frac{e^{-n^2\xi}}{\xi^2}\left(\int_1^\xi f_n(s)se^{n^2 s}ds\right)d\xi.$$

The general solution of (6) is given by

$$\zeta_n(t) = A_n t + B_n t \int_t^\infty \frac{e^{-n^2 s}}{s^2} ds + t \int_1^t \frac{e^{-n^2 \xi}}{\xi^2} \left(\int_1^\xi f_n(s) s e^{n^2 s} ds \right) d\xi,$$

$$v_n(t) = A_n + B_n \int_t^\infty \frac{e^{-n^2 s}}{s^2} ds - \frac{B_n}{t} e^{-n^2 t} + \int_1^t \frac{e^{-n^2 \xi}}{\xi^2} \left(\int_1^\xi f_n(s) s e^{n^2 s} ds \right) d\xi + \frac{e^{-n^2 t}}{t} \left(\int_1^t f_n(s) s e^{n^2 s} ds \right),$$

where

$$A_n = \zeta_n(1) - B_n \int_1^\infty \frac{e^{-n^2 s}}{s^2} ds, \quad B_n = e^{n^2} \left(\zeta_n(1) - v_n(1) \right).$$

In the sequel we assume that the solutions $\zeta(x,t)$ and $v(x,t)$ are in H^2, and that the initial data are small, i.e.

$$\sum_{n=-\infty}^{\infty} (1+n^4) \left(|v_n(1)|^2 + |\zeta_n(1)|^2 \right) < \epsilon.$$

Next we introduce the norm

$$|||\psi|||_{L,k}^2 = \int_{(L-1)^+}^L \|\psi(t)\|_{H^k(\Omega)}^2 \, dt, \quad k \geq 0,$$

with $L > 1$, $(L-1)^+ = \max\{L-1, 1\}$.

Lemma 2.3 *Let ψ be smooth in $[(L-1)^+, L] \times \Omega$. Then*

$$\sup_{(L-1)^+ < t < L} \|\psi(t)\|_{H^2} \leq C \left(|||\psi|||_{L,2} + |||\psi_t|||_{L,2} \right). \tag{7}$$

Proof. We note first that there exists $\bar{t} \in ((L-1)^+, L)$ such that $\|\psi(\bar{t})\|_{H^2} \leq |||\psi|||_{L,2}$. Thus

$$\psi(x,t) - \psi(x,\bar{t}) = \int_{\bar{t}}^t \psi_s(x,s) ds, \quad \text{for any } (L-1)_+ < t < L.$$

Taking the H^2-norm on both sides of the equality and using Hölder's inequality, (7) is immediate. □

Now we state local existence of small solutions.

Proposition 2.4 *Let (v, ζ) be a solution of (3). There exist $\epsilon > 0$ and $\delta = \delta(\epsilon)$ such that for $\|v(1)\|_{H^2} + \|\zeta(1)\|_{H^2} < \delta$ there exists $T = T(\epsilon) > 0$ such that*

$$\sup_{L<T} |||v|||_{L,2} < \epsilon, \quad \sup_{L<T} |||\zeta|||_{L,2} < \epsilon L.$$

Proof. The proof is standard, so details are skipped. □

Lemma 2.5 *Let $T \in (1,\infty]$ be the time in Proposition 2.4. Then for any $t < T$*

$$\|\zeta(t)\|_{L^\infty} + \|\zeta(t)\|_{H^2} \le C\epsilon t. \tag{8}$$

Proof. Since $\|\zeta(t)\|_{L^\infty} \le C\|\zeta(t)\|_{H^2}$, it is sufficient to estimate $\|\zeta(t)\|_{H^2}$. Let $t \in ((L-1)^+, L)$ where $L < \min\{T, 2t\}$. Due to Lemma 2.3 and Proposition 2.4 we have

$$\|\zeta(t)\|_{H^2} \le C\left(|||\zeta|||_{L,2} + |||\zeta_t|||_{L,2}\right) \le C\left(|||\zeta|||_{L,2} + |||v|||_{L,2}\right) \le C\epsilon L \le C\epsilon t.$$

This completes the proof. □

Lemma 2.6 *Let $T \in (1,\infty]$ be the time in Proposition 2.4. Then for any $t < T$,*

$$\left\| v(t) - \frac{\zeta(t)}{t} \right\|_{H^1} \le C\epsilon e^{-Ct}, \qquad \|f(t)\|_{L^2} \le C\epsilon^2 e^{-Ct}.$$

Proof. With (8) we can estimate $f(x,t)$ for $t \in [1,T)$ as follows

$$\begin{aligned}\|f(t)\|_{L^2(\Omega)} &\le \left\| \left(\frac{\zeta_x}{\bar{z}+\zeta}(v - \frac{\zeta}{t}) \right)_x \right\|_{L^2(\Omega)} \le C\left(\frac{1}{t}\|\zeta\|_{H^2} \left\| v - \frac{\zeta}{t} \right\|_{H^1} + \frac{1}{t^2}\|\zeta\|_{H^2}^2 \left\| v - \frac{\zeta}{t} \right\|_{L^2} \right) \\ &\le C(\epsilon + \epsilon^2) \left\| v - \frac{\zeta}{t} \right\|_{H^1} \le C\epsilon \left\| v - \frac{\zeta}{t} \right\|_{H^2}. \end{aligned} \tag{9}$$

Since $v_n' + n^2 v_n - \frac{n^2}{t}\xi_n = f_n$, we have

$$\frac{d}{dt}(v_n - \frac{\xi_n}{t}) + n^2(v_n - \frac{\xi_n}{t}) + \frac{1}{t}(v_n - \frac{\xi_n}{t}) = f_n.$$

Multiplying with $n^2(v_n - \frac{\xi_n}{t})$, we get

$$\frac{n^2}{2}\frac{d}{dt}(v_n - \frac{\xi_n}{t})^2 + n^4(v_n - \frac{\xi_n}{t})^2 + \frac{n^2}{t}(v_n - \frac{\xi_n}{t})^2 = f_n n^2 (v_n - \frac{\xi_n}{t}).$$

This implies that

$$\frac{1}{2}\frac{d}{dt}\left\| v - \frac{\zeta}{t} \right\|_{H^1}^2 + \left\| v - \frac{\zeta}{t} \right\|_{H^2}^2 + \left\| \frac{1}{\sqrt{t}}(v - \frac{\zeta}{t}) \right\|_{H^1}^2 \le \|f\|_{L^2} \left\| v - \frac{\zeta}{t} \right\|_{H^2}.$$

Due to (9), we obtain

$$\frac{1}{2}\frac{d}{dt}\left\| v - \frac{\zeta}{t} \right\|_{H^1}^2 + (1 - C\epsilon)\left\| v - \frac{\zeta}{t} \right\|_{H^2}^2 \le 0. \tag{10}$$

Hence as long as ϵ is sufficiently small, by integrating over $[1,t)$ we obtain

$$\left\| v(t) - \frac{\zeta(t)}{t} \right\|_{H^1} \le \|v_0 - \zeta_0\|_{H^1} e^{-Ct} \le \epsilon e^{-Ct}. \tag{11}$$

The second estimate is direct from (9) and (11). This completes the proof. □

Proposition 2.7 *There exist $\epsilon > 0$ and $\delta = \delta(\epsilon)$ such that for $\|v(1)\|_{H^2} + \|\zeta(1)\|_{H^2} < \delta$ we have $|||v|||_{t,2} \le \epsilon$ and $|||\zeta|||_{t,2} \le \epsilon t$ for all $t < \infty$. Moreover, there exists $v_\infty \in H^2$ such that*

$$\left\| \frac{\zeta(t)}{t} - v_\infty \right\|_{H^2} \longrightarrow 0 \quad \text{for } t \to \infty,$$
$$\|v(t) - v_\infty\|_{H^1} \longrightarrow 0 \quad \text{for } t \to \infty, \text{ and}$$
$$|||v - v_\infty|||_{L,2} \longrightarrow 0 \quad \text{for } L \to \infty.$$

Proof. Let T be the time in Proposition 2.4. We claim that $T = \infty$. Suppose that this is not the case, i.e. $T < \infty$. Then either $|||v|||_{T,2} > \epsilon$ or $|||\zeta|||_{T,2} > \epsilon T$. Suppose that $|||v|||_{T,2} > \epsilon$. For the case $|||\zeta|||_{T,2} > \epsilon T$ we could argue similarly.

Recall the representation formula for v_n:

$$v_n(t) = A_n + B_n \int_t^\infty \frac{e^{-n^2 s}}{s^2} ds - \frac{B_n}{t} e^{-n^2 t}$$
$$+ \int_1^t \frac{e^{-n^2 \xi}}{\xi^2} \left(\int_1^\xi f_n(s) s e^{n^2 s} ds \right) d\xi + \frac{e^{-n^2 t}}{t} \left(\int_1^t f_n(s) s e^{n^2 s} ds \right), \tag{12}$$

where

$$A_n = \zeta_n(1) - B_n \int_1^\infty \frac{e^{-n^2 s}}{s^2} ds, \quad B_n = e^{n^2} \left(\zeta_n(1) - v_n(1) \right).$$

It is sufficient to consider the nonlinear parts (12). For simplicity denote

$$\Psi_n(t) := \int_1^t \frac{e^{-n^2 \xi}}{\xi^2} \left(\int_1^\xi f_n(s) s e^{n^2 s} ds \right) d\xi + \frac{e^{-n^2 t}}{t} \left(\int_1^t f_n(s) s e^{n^2 s} ds \right) = I_n(t) + II_n(t).$$

Integrating by parts we obtain

$$I_n(t) = -\frac{e^{-n^2 t}}{n^2 t^2} \int_1^t f_n(s) s e^{n^2 s} ds + \frac{1}{n^2} \int_1^t \frac{f_n(\xi)}{\xi} d\xi - \frac{2}{n^2} \int_1^t \frac{e^{-n^2 \xi}}{\xi^3} \left(\int_1^\xi f_n(s) s e^{n^2 s} ds \right) d\xi .$$

Direct computations show that

$$\int_{(T-1)^+}^T \sum_{n=-\infty}^\infty n^4 I_n^2(\tau) d\tau \le C \int_1^T \sum_{n=-\infty}^\infty f_n^2(s) ds = C \|f\|^2_{L^2(Q_T)} \le C\epsilon^4 \int_1^T e^{-ct} dt \le C\epsilon^4.$$

Next consider

$$|II_n(t)| \le \frac{e^{-n^2 t}}{t} \left(\int_1^t |f_n(s)| \, s e^{n^2 s} ds \right) \le \int_1^t |f_n(s)| \, e^{n^2 (s-t)} ds =: y(t).$$

Since the right hand side is a solution of $y'(t) + n^2 y(t) = |f_n|$, one can estimate

$$\int_{(T-1)^+}^T \sum_{n=-\infty}^\infty n^4 II_n^2(\tau) d\tau \le C \int_1^T \sum_{n=-\infty}^\infty f_n^2(s) ds = C \|f\|^2_{L^2(Q_T)} \le C\epsilon^4. \tag{13}$$

This can be seen by defining $y_n(t) = \int_1^t |f_n(s)|\, e^{n^2(s-t)} ds$. Thus $y_n'(t) + n^2 y_n(t) = |f_n(t)|$. Define

$$Y(x,t) = \sum_{n\neq 0} y_n(t)\, e^{inx}, \qquad F(x,t) = \sum_{n\neq 0} |f_n(t)|\, e^{inx}.$$

Then for $t \geq 1$, Y solves in $I = [0,\pi]$ the following equation

$$Y_t = Y_{xx} + F, \qquad Y(x,1) = 0.$$

Further, classical estimates, using the fact that we do not have a neutral eigenvalue, yield

$$\|Y(\cdot,t)\|_{L^2}^2 \leq C \int_1^T \|F(\cdot,t)\|_{L^2}^2\, dt\ .$$

With classical regularity theory for the heat equation we obtain

$$\begin{aligned}\int_{(T-1)_+}^T \|Y(\cdot,t)\|_{H^2}^2 &\leq C \sup_{t-1\leq s\leq t} \|Y(\cdot,s)\|_{L^2}^2 + C\int_{(T-1)_+}^T \|F(\cdot,t)\|_{L^2}^2\, dt \\ &\leq C\int_1^T \|F(\cdot,t)\|_{L^2}^2\, dt\ .\end{aligned}$$

Since

$$\sum_n n^4 II_n^2 = \sum_{n\neq 0} n^4 |y_n(t)|^2 = \|Y(\cdot,t)\|_{H^2}^2\,,$$

the estimate (13) follows. Summing up, we obtain

$$\begin{aligned}\|v\|_{T,2} &\leq \{\text{linear terms}\} + \left(\int_{(T-1)^+}^T \sum_{n=-\infty}^{\infty} n^4 I_n^2(\tau) d\tau\right)^{\frac{1}{2}} + \left(\int_{(T-1)^+}^T \sum_{n=-\infty}^{\infty} n^4 II_n^2(\tau) d\tau\right)^{\frac{1}{2}} \\ &\leq C\delta + C\epsilon^2.\end{aligned}$$

This shows $|||v|||_{T,2} < \epsilon$, which contradicts our hypothesis. Thus, T cannot be finite.

Next we show convergence. We will prove that $I_n(t) = \zeta_n/t - A_n \in H^2$ and $I_n(t) \leq C\epsilon^2$ for all t. By changing the order of integration and using Hölder's inequality, we obtain

$$|I_n(t)| = \left|\int_1^t f_n(s) s e^{n^2 s} \int_s^t \frac{e^{-n^2\xi}}{\xi^2} d\xi ds\right| \leq \int_1^t |f_n(s)|\, s e^{n^2 s} \int_s^t \frac{e^{-n^2\xi}}{\xi^2} d\xi ds$$

$$\leq \frac{C}{n^2}\int_1^t \frac{|f_n(s)|}{s} ds \leq \frac{C}{n^2}\left(\int_1^t |f_n|^2\, ds\right)^{\frac{1}{2}} \left(\int_1^t s^{-2} ds\right)^{\frac{1}{2}} \leq \frac{C}{n^2}\left(\int_1^t |f_n|^2\, ds\right)^{\frac{1}{2}}.$$

Due to Lemma 2.6, we have that $n^4 |I_n(t)|^2 \leq C\epsilon^4$ for all t. This implies that ζ/t is in H^2 and converges to $v_\infty \in H^2$ for $t\to\infty$, with

$$v_\infty = \sum (v_\infty)_n e^{inx}, \quad \text{where} \quad (v_\infty)_n = A_n + I_n(\infty),$$

and

$$I_n(\infty) = \int_1^\infty \frac{e^{-n^2\xi}}{\xi^2} \left(\int_1^\xi f_n(s) s e^{n^2 s} ds \right) d\xi.$$

Now it is direct that

$$\frac{\zeta}{t} \longrightarrow v_\infty \quad \text{in } H^2 \quad \text{for } t \to \infty. \tag{14}$$

From (10), we have

$$\left\| v(t) - \frac{\zeta(t)}{t} \right\|_{H^1} \longrightarrow 0 \text{ for } t \to \infty, \qquad \left| \left| \left| v(t) - \frac{\zeta(t)}{t} \right| \right| \right|_{L,2} \longrightarrow 0 \text{ for } L \to \infty. \tag{15}$$

Combining (14) and (15), we obtain that v converges to v_∞ in the H^1 and the $(L,2)-$norm, since

$$\begin{aligned} \|v - v_\infty\|_{H^1} + |||v - v_\infty|||_{L,2} &\le \left\| v - \frac{\zeta}{t} \right\|_{H^1} + \left\| \frac{\zeta}{t} - v_\infty \right\|_{H^1} + \left| \left| \left| v - \frac{\zeta}{t} \right| \right| \right|_{L,2} + \left| \left| \left| \frac{\zeta}{t} - v_\infty \right| \right| \right|_{L,2} \\ &\le \left\| v - \frac{\zeta}{t} \right\|_{H^1} + \left| \left| \left| v - \frac{\zeta}{t} \right| \right| \right|_{L,2} + \left\| \frac{\zeta}{t} - v_\infty \right\|_{H^2}. \end{aligned}$$

This completes the proof. □

Summarizing the previous estimates, for $\theta = 1$ we obtain our main result of this section, namely Theorem 2.1.

3 Qualitative behavior of the system for $1 < \theta < 3$

From now on let $I = [-1, 1]$. The reason for this change of domain of integration is simply to fix the expected singularity at the origin and avoid dealing with complicated shifts of its location. We consider

$$u_t = u_{xx} - \theta \left(\frac{z_x}{z} u \right)_x, \qquad z_t = u \qquad \text{in } I \times [0, \infty),$$

$$u(x,0) = u_0(x), \quad z(x,0) = z_0(x), \text{ with periodic boundary conditions.}$$

First, to get a quick insight, we give a heuristic argument regarding the blow-up asymptotics for this system for $t \to \infty$. After this we will go into the details of the rigorous analysis. For the heuristics we assume w.l.o.g. that $\int_I u\, dx = 1$ and consider the simplified equation

$$\bar{z}_t = \frac{\bar{z}^\theta}{\int_I \bar{z}^\theta dx}.$$

We expect this simplified equation to be a good approximation for the dynamics of the original problem for $t \to \infty$. Assuming that $z_0(0) > z_0(x)$ for any $x \in I \setminus \{0\}$ we can solve this equation and obtain

$$\bar{z}^{1-\theta}(x,t) = \bar{z}_0^{1-\theta}(x) - (\theta - 1) \int_0^t \frac{ds}{\int_I \bar{z}^\theta(x,s) dx}.$$

We assume further that z_0 can be expanded near zero as follows:

$$\bar{z}_0^{1-\theta}(x) = \bar{z}_0^{1-\theta}(0) + Bx^2 + h.o.t. \qquad \text{for } x \to 0.$$

Here B is a positive constant depending on the initial data. Continuing the heuristic argument, we thus obtain

$$\bar{z}^{1-\theta}(x,t) \approx \bar{z}_0^{1-\theta}(0) + Bx^2 - (\theta-1)\int_0^t \frac{ds}{\int_I \bar{z}^\theta(x,s)dx}\,.$$

Define

$$\psi(t) := \bar{z}_0^{1-\theta}(0) - (\theta-1)\int_0^t \frac{ds}{\int_I \bar{z}^\theta(x,s)dx}.$$

Thus $\bar{z}^{1-\theta}(x,t) \approx Bx^2 + \psi(t)$, and

$$\bar{z}(x,t) \approx \frac{1}{(Bx^2+\psi(t))^{\frac{1}{\theta-1}}}.$$

Direct computations show

$$-\frac{\theta-1}{\psi'(t)} \approx \int_I \frac{dx}{(Bx^2+\psi(t))^{\frac{\theta}{\theta-1}}}.$$

So we get $\psi'(t) \approx -K\psi^{\frac{\theta+1}{2(\theta-1)}}(t)$, where K is a positive constant. This yields $\psi(t) \approx At^{-\frac{2(\theta-1)}{3-\theta}}$ with a constant $A > 0$ for $t\to\infty$. Since $\psi(t)\to 0$ for $t\to\infty$, we see that

$$\bar{z}_0^{1-\theta}(0) \approx (\theta-1)\int_0^\infty \frac{ds}{\int_I \bar{z}^\theta(x,s)dx}.$$

Therefore, noting that $\psi'(t) \approx -KA^{\frac{\theta+1}{2(\theta-1)}}t^{-\frac{\theta+1}{3-\theta}}$ for $t\to\infty$, we obtain

$$\psi(t) \approx (\theta-1)\int_t^\infty \frac{ds}{\int_I \bar{z}^\theta dx} \quad \Longrightarrow \quad \int_I \bar{z}^\theta dx \approx \frac{\theta-1}{KA^{\frac{\theta+1}{2(\theta-1)}}}t^{\frac{\theta+1}{3-\theta}},$$

and

$$\bar{z}(x,t) \approx \frac{1}{\left(Bx^2 + At^{-\frac{2(\theta-1)}{3-\theta}}\right)^{\frac{1}{\theta-1}}} = \frac{t^{\frac{2}{3-\theta}}}{\left(Bx^2t^{\frac{2(\theta-1)}{3-\theta}} + A\right)^{\frac{1}{\theta-1}}}.$$

Now we are ready to present rigorous arguments which justify the given heuristics. A first idea for a quasi-steady state approximation of the system under consideration in the given regime for θ was given by Schwetlick, [10]. The main theorem we will prove in this section is the following

Theorem 3.1 *There exist initial data $u_0, z_0 \in C^{2,\nu}$ such that the corresponding solutions (u, z) of (1) satisfy $u(x,t) \to m\delta(x)$ and $z(x,t) \approx \frac{t^{\frac{2}{3-\theta}}}{(Bx^2 t^{\frac{2(\theta-1)}{3-\theta}} + A)^{\frac{1}{\theta-1}}}$ for $t \to \infty$, where $m = \int_I u_0(x)dx$ and A, B are constants depending on the initial data.*

Remark: As we will see in Assumption 3.5 later, the condition on the initial data is, that u_0, z_0 are symmetric, u_0 is concentrated at the origin, and z_0 behaves like a power law at the origin. For convenience we will also assume in the following that $m = 1$.

To prove this theorem we need several steps.

3.1 The Eigenvalue problem

We define the differential operator

$$\tilde{A}_z(f) := f_{xx} - \theta\left(\frac{z_x}{z}f\right)_x = \left(f_x - \theta\left(\frac{z_x}{z}f\right)\right)_x \qquad \text{in } [-1,1].$$

Consider the eigenvalue problem $\tilde{A}_z(f) = \lambda f$, i.e.

$$f_{xx} - \theta\left(\frac{z_x}{z}f\right)_x = \lambda f, \qquad f(-1) = f(1),\ \ f_x(-1) = f_x(1).$$

Since we have assumed periodic boundary conditions in $\mathbb{R}$, it is direct that $f(-1) = f(1) = f_x(-1) = f_x(1) = 0$. Now a class of functions $\mathcal{A}$ is introduced, which is assumed to contain z.

Assumption 3.2 *Let $0 < \nu < 1$ and let $\mathcal{A}$ be a class of nonnegative functions such that for $g \in \mathcal{A}$ the following conditions hold*

1. *$g \in \mathcal{C}^{2,\nu}$ is nonnegative and symmetric with respect to zero, i.e $g(-x) = g(x)$. Furthermore, there exists $M > 0$ such that*

$$t^{-\frac{2}{3-\theta}}\left[t^{-\frac{\theta-1}{3-\theta}(2+\nu)} \sup_{|x_1|,|x_2|\le t^{-\frac{\theta-1}{3-\theta}}}\left(\frac{|g_{xx}(x_1) - g_{xx}(x_2)|}{|x_1 - x_2|^{\nu}}\right)\right]$$
$$+ \sup_{t^{-\frac{\theta-1}{3-\theta}} \le R \le 1} R^{\frac{2}{\theta-1}}\left[R^{(2+\nu)} \sup_{R/2 \le |x_1|,|x_2| \le R} \frac{|g_{xx}(x_1) - g_{xx}(x_2)|}{|x_1 - x_2|^{\nu}}\right] \le M\ .$$

2. *There exist $A, B, M > 0$ such that*

$$\frac{t^{\frac{2}{3-\theta}}}{M\left(Bx^2 t^{\frac{2(\theta-1)}{3-\theta}} + A\right)^{\frac{1}{\theta-1}}} \le g(x) \le \frac{Mt^{\frac{2}{3-\theta}}}{\left(Bx^2 t^{\frac{2(\theta-1)}{3-\theta}} + A\right)^{\frac{1}{\theta-1}}}.$$

3. There exist $A, B, M > 0$ such that

$$|g_x| \leq M \frac{x t^{\frac{2\theta}{3-\theta}}}{\left(Bx^2 t^{\frac{2(1-\theta)}{3-\theta}} + A\right)^{\frac{\theta}{\theta-1}}}.$$

4. There exists $\epsilon_0 > 0$ such that

$$\left|\frac{g_x}{g} - \frac{1}{\theta-1}\frac{1}{x}\right| \leq \frac{\epsilon_0}{|x|}, \qquad \left|\left(\frac{g_x}{g} - \frac{1}{\theta-1}\frac{1}{x}\right)_x\right| \leq \frac{\epsilon_0}{|x|^2}.$$

From now on, and in difference to the previous section, the appearing constants $C = C(\theta, M)$ will depend on θ and on M, as well as the constants denoted by C_δ, C_γ.

Lemma 3.3 *The operator $\tilde{A}_z(t)$ is self-adjoint with respect to the weighted integral $\frac{dx}{z^\theta}$. All eigenvalues are non-positive and the first eigenvalue λ_0 is equal to 0 with corresponding eigenfunction z^θ.*

Proof. We know that $h_x - \theta\frac{z_x}{z}h = (\frac{h}{z^\theta})_x z^\theta$ for any h and

$$\int_I \tilde{A}_z(f) g \frac{dx}{z^\theta} = -\int_I (f_x - \theta\frac{z_x}{z}f)\left(\frac{g}{z^\theta}\right)_x dx = -\int_I \left(\frac{f}{z^\theta}\right)_x (g_x - \theta\frac{z_x}{z}g)dx = \int_I f\tilde{A}_z(g)\frac{dx}{z^\theta}.$$

It follows from standard arguments that all eigenvalues are non-positive (compare [1]). It is straightforward that z^θ is an eigenvector corresponding to the eigenvalue 0. □

Proposition 3.4 *Let λ_1 be the second eigenvalue for the differential operator $\tilde{A}_z(t)$. Suppose that $z(x,t)$ satisfies Assumption 3.2. Then there exists an absolute constant $C > 0$ independent of z such that*

$$\lambda_1 \leq -C \qquad \text{for all } t.$$

Proof. Suppose that this is not the case. Then there exist a sequence of t_m, functions $z_m \in \mathcal{A}$, and eigenvalues $\lambda_{1,m} \nearrow 0$ for $t_m \to t_\infty$ (with t_∞ being either finite or infinite), and corresponding eigenfunctions $\phi_{1,m}$ such that

$$\tilde{A}_{z_m}(\phi_{1,m}) = (\phi_{1,m})_{xx} - \theta\left(\frac{(z_m)_x}{z_m}\phi_{1,m}\right)_x = \lambda_{1,m}\phi_{1,m}.$$

Here we assume that the eigenfunction $\phi_{1,m}$ is normalized i.e. $\int |\phi_{1,m}|^2 \frac{dx}{z_m^\theta} = 1$.

• **If** $t_\infty < \infty$, then by Assumption 3.2 we have that $\|z_m\|_{\mathcal{C}^{2,\nu}}$ is uniformly bounded, and z_m converges to z_∞ in $\mathcal{C}^2$. Classical regularity theory implies that $\phi_m \in \mathcal{C}^{2,\nu}$ and $\|\phi_m\|_{\mathcal{C}^{2,\nu}} \leq C$ for all m. Due to Sturm-Liouville theory, the eigenfunctions $\phi_{1,m}$ satisfy

$\phi_{1,m}(0) = 0$ and $\phi_{1,m}(x) > 0$ for $x \in (0,1)$. In addition, there exists $\phi_{1,\infty}$ such that $\phi_{1,m} \to \phi_{1,\infty}$ in $\mathcal{C}^2$. Then the limiting equation becomes

$$\tilde{A}_{z_\infty}(\phi_{1,\infty}) = (\phi_{1,\infty})_{xx} - \theta \left(\frac{(z_\infty)_x}{z_\infty} \phi_{1,\infty} \right)_x = 0.$$

This equation can be solved explicitly and we obtain

$$\phi_{1,\infty}(x) = K z_\infty^\theta(x) + C \int_0^x \frac{z_\infty^\theta(x)}{z_\infty^\theta(\xi)} d\xi.$$

Since $\phi_{1,\infty}$ is periodic and z_∞ is nonnegative, the integral term above must vanish, and thus $\phi_{1,\infty}(x) = K z_\infty^\theta(x)$. This yields $K = 0$, because $\phi_{1,\infty}(0) = 0$ and $z_\infty(0) > 0$. Hence $\phi_{1,\infty} = 0$, which contradicts the fact that $\int |\phi_{1,\infty}|^2 \frac{dx}{z_\infty^\theta} = 1$.

• **The case $t_\infty = \infty$.** For any $0 < \delta < 1$ we note that $\|z_m\|_{\mathcal{C}^{2,\nu}(I \setminus [-\delta,\delta])} \le C_\delta$. Let $\delta_0 > 0$ be sufficiently small. Let $\psi(x) = C_\gamma x^\gamma$ with $\gamma > 1$, where C_γ is a constant satisfying $C_\gamma \delta_0^\gamma = C_\delta$ in $[0, \delta_0]$. We show that $\psi \ge z_m$ for all m. Indeed, for sufficiently small $\epsilon = \epsilon(\gamma)$ we have

$$\tilde{A}_{z_m}(\psi) = \gamma(\gamma-1)x^{\gamma-2} - \frac{\theta}{\theta-1}(\gamma-1)x^{\gamma-2} - \theta \left((\frac{(z_m)_x}{z_m} - \frac{1}{(\theta-1)x})\psi \right)_x$$

$$= (\gamma-1)\left(\gamma - \frac{\theta}{\theta-1}\right) x^{\gamma-2} - \theta \left(\frac{(z_m)_x}{z_m} - \frac{1}{(\theta-1)x} \right)_x \psi - \theta \left(\frac{(z_m)_x}{z_m} - \frac{1}{(\theta-1)x} \right) \psi_x$$

$$\le (\gamma-1)\left(\gamma - \frac{\theta}{\theta-1}\right) x^{\gamma-2} + \theta \frac{\epsilon}{x^2} x^\gamma + \theta\gamma \frac{\epsilon}{x} x^{\gamma-1}$$

$$= (\gamma-1)\left(\gamma - \frac{\theta}{\theta-1} + \theta\epsilon \frac{1+\gamma}{\gamma-1}\right) x^{\gamma-2} .$$

So $\tilde{A}_{z_m}(\psi) \le 0$ in $[0, \delta_0]$ for $1 < \gamma < \frac{\theta}{\theta-1}$ and so ψ is a super-solution of $\phi_{1,m}$ for all m, namely, due to the maximum principle,

$$|\phi_{1,m}(x)| \le C_\gamma |x|^\gamma , \qquad 0 \le x \le \delta_0.$$

There exists $\phi_{1,\infty}$ such that $\phi_{1,m} \to \phi_{1,\infty}$ in $\mathcal{C}^2$ over $[\delta, 1]$ for any $0 < \delta < 1$ and thus the limiting equation becomes

$$\tilde{A}_{z_\infty}(\phi_{1,\infty}) = (\phi_{1,\infty})_{xx} - \theta \left(\frac{(z_\infty)_x}{z_\infty} \phi_{1,\infty} \right)_x = 0.$$

As in the previous case, this leads to a contradiction and completes the proof. □

For convenience, we denote $< g, h >= \int_I g(x)h(x)\frac{dx}{z^\theta}$ for functions g and h which are integrable with respect to dx/z^θ. We define v in terms of $u := \frac{z^\theta}{\int_I z^\theta dx} + v$. Note that $\int_I v dx = 0$ and $< z^\theta, v >= 0$. Furthermore, v solves

$$v_t = v_{xx} - \theta\left(\frac{z_x}{z}v\right)_x - \left(\frac{z^\theta}{\int_I z^\theta dx}\right)_t . \tag{16}$$

For simplicity we denote

$$\mathcal{R}(x,t) := -\left(\frac{z^\theta}{\int_I z^\theta dx}\right)_t = -\theta\frac{z^{\theta-1}u}{\int_I z^\theta dx} + \theta\frac{z^\theta \int z^{\theta-1}udx}{\left(\int_I z^\theta dx\right)^2} . \tag{17}$$

Now we make an assumption on v, which will be recovered in the end.

Assumption 3.5 *Suppose that $z(x,t)$ satisfies Assumption 3.2. Further suppose that*

$$|v(x,t)| \le M\frac{z^\theta(x,t)}{\int_I z^\theta(y,t)dx} ,$$

for a suitable constant $M > 0$.

Let us first give a useful lemma, which is an adaptation of a result given in [7] and provides one of the main estimates for the result stated thereafter. For the purpose of this paper we use a formulation restated in [4], which is more accessible. The proof of our lemma will be given later in the paper.

Lemma 3.6 *Let $1 < \theta < 3$. Suppose that $\zeta \in C^1([0,1])$ with $\zeta(0) = 0$, and z satisfy Assumption 3.2 for all $t \ge 1$. Then*

$$\left(\int_0^1 z^{(p-1)\theta}|\zeta|^p dx\right)^{\frac{1}{p}} \le C\left(\int_0^1 z^\theta |\zeta_x|^2 dx\right)^{\frac{1}{2}}, \qquad p = \frac{6\theta-2}{\theta+1}.$$

With this result we can show a Sobolev inequality with the weighted norm $z^{-\theta}$.

Lemma 3.7 *Suppose that $z(x,t)$ satisfies Assumption 3.2, and that $h_x \in L^2(z^{-\theta}dx)$ with $\int_I h = 0$, where $I = [-1,1]$. Then*

$$\left(\int_I |h|^p \frac{dx}{z^\theta}\right)^{\frac{1}{p}} \le C\left(\int_I \left|h_x - \theta\frac{z_x}{z}h\right|^2 \frac{dx}{z^\theta}\right)^{\frac{1}{2}}, \qquad p = \frac{6\theta-2}{\theta+1} . \tag{18}$$

Here C is an absolute constant independent of t, z, and θ, but depending on M.

Proof. We consider the following variational problem:

$$-\left(h_x - \theta\frac{z_x}{z}h\right)_x = \lambda\left(|h|^{p-2}h - z^\theta\frac{\int_I |h|^{p-2}hdx}{\int_I z^\theta dx}\right)$$

with $\int_I |h|^p \frac{dx}{z^\theta} = 1$. Due to Assumption 3.2, $z(x,t)$ is non-singular for every finite t, and thus classical theory for semi-linear elliptic boundary value problems with constraints, compare [12] implies that there exists $\lambda(t) > 0$ such that

$$\left(\int_I |h|^p \frac{dx}{z^\theta}\right)^{\frac{1}{p}} \leq \frac{1}{\sqrt{\lambda(t)}} \left(\int_I \left|h_x - \theta \frac{z_x}{z} h\right|^2 \frac{dx}{z^\theta}\right)^{\frac{1}{2}}.$$

Our goal is to show that there exists $k > 0$ such that $\lambda \geq k$ for all $t \geq t_0$.
Suppose that this not the case. Then there exist t_n, z_n, h_n with $\int_I |h_n|^p \frac{dx}{z_n^\theta} = 1$ and $\lambda_n(t_n) \searrow 0$ for $t_n \to \infty$, possibly after choosing a suitable subsequence, such that

$$\lambda_n = \int_I \left|(h_n)_x - \theta \frac{(z_n)_x}{z_n} h_n\right|^2 \frac{dx}{z_n^\theta}.$$

We introduce a new function $\varphi_n := \frac{h_n}{z_n^\theta}$. Then, since we want to minimize the constant C in (18), the given problem can be rewritten as an eigenvalue problem

$$-\left(z_n^\theta (\varphi_n)_x\right)_x = \lambda_n \left[z_n^{(p-1)\theta} |\varphi_n|^{p-2} \varphi_n - \frac{\int_I z_n^{(p-1)\theta} |\varphi_n|^{p-2} \varphi_n dx}{\int_I z_n^\theta dx} z_n^\theta\right],$$

because

$$\int_I |h_n|^p \frac{dx}{z_n^\theta} = \int_I |\varphi_n|^p z_n^{(p-1)\theta} dx \,. \tag{19}$$

Additionally, the normalization and orthogonality condition have to be fulfilled, namely

$$\int_I z_n^{(p-1)\theta} |\varphi_n|^p \, dx = 1, \quad \int_I z_n^\theta \varphi_n dx = 0, \quad \text{and} \quad \lambda_n = \int_I z_n^\theta |(\varphi_n)_x|^2 \, dx.$$

Now expressing $\varphi_n = \varphi_n(0) + \psi_n$ we can estimate (19) by

$$\int_I |\varphi_n|^p z_n^{(p-1)\theta} dx \leq \int_I |\varphi_n(0,t)|^p z_n^{(p-1)\theta} dx + \int_I |\psi_n(x,t)|^p z_n^{(p-1)\theta} dx \,. \tag{20}$$

To control the first term on the right hand side of (20), we estimate $|\varphi_n(0,t)|$. First, by Hölder's inequality we obtain

$$\begin{aligned} |\varphi_n(x,t) - \varphi_n(0,t)| = \left|\int_0^x (\varphi_n)_x(\xi,t) d\xi\right| &\leq \left(\int_0^x |(\varphi_n)_x|^2 z_n^\theta d\xi\right)^{\frac{1}{2}} \left(\left|\int_0^x \frac{d\xi}{z_n^\theta}\right|\right)^{\frac{1}{2}} \\ &\leq \sqrt{\lambda_n} \left(\left|\int_0^x \frac{d\xi}{z_n^\theta}\right|\right)^{\frac{1}{2}}. \end{aligned} \tag{21}$$

Therefore, we have

$$|\varphi_n(x,t)| \leq |\varphi_n(0,t)| + \sqrt{\lambda_n} \left(\left|\int_0^x \frac{d\xi}{z_n^\theta(\xi,t)}\right|\right)^{\frac{1}{2}}. \tag{22}$$

Due to (21), it is direct that $|\psi_n| \leq \sqrt{\lambda_n}\left(\left|\int_0^x \frac{d\xi}{z_n^\theta(\xi,t)}\right|\right)^{\frac{1}{2}}$. Using $0 = \int_I z_n^\theta \varphi_n dx = \varphi_n(0,t)\int_I z_n^\theta dx + \int_I z_n^\theta \psi_n dx$, we obtain due to (22)

$$|\varphi_n(0,t)| = \left|\frac{\int_I z_n^\theta \psi_n dx}{\int_I z_n^\theta dx}\right| \leq \frac{\sqrt{\lambda_n}\int_I z_n^\theta \left(\left|\int_0^x \frac{d\xi}{z_n^\theta}\right|\right)^{\frac{1}{2}} dx}{t^{\frac{\theta+1}{3-\theta}}} \leq C\sqrt{\lambda_n} t^{-\frac{\theta+1}{3-\theta}}.$$

Here we used that $\int_I z_n^\theta \left(\int_I \frac{d\xi}{z_n^\theta}\right)^{\frac{1}{2}} dx \leq C$. Due to Assumption 3.2, 2., we compute

$$\int_I z_n^{(p-1)\theta} |\varphi_n(0)|^p \, dx \leq C\lambda_n^{\frac{p}{2}} t^{-\frac{(\theta+1)p}{3-\theta}} \int_I z_n^{(p-1)\theta} dx \leq C\lambda_n^{\frac{p}{2}} t^{-\frac{3\theta-1}{1+\theta}},$$

where we used $\int_I (y^2+a)^{-\frac{\theta(p-1)}{\theta-1}} dy < \infty$. Now we estimate the second term in (20). This is done by Lemma 3.6. For $p > 2$ we obtain

$$\begin{aligned}\left(\int_I z_n^{(p-1)\theta} |\varphi_n|^p \, dx\right)^{\frac{1}{p}} &\leq \left(\int_I z_n^{(p-1)\theta} |\varphi_n(0,t)|^p \, dx\right)^{\frac{1}{p}} + \left(\int_I z_n^{(p-1)\theta} |\psi_n|^p \, dx\right)^{\frac{1}{p}} \\ &\leq C\lambda_n^{\frac{p}{2}} t^{-\frac{3\theta-1}{1+\theta}} + C\left(\int_I z_n^\theta |(\psi_n)_x|^2 \, dx\right)^{\frac{1}{2}} \leq C\lambda_n \to 0 \quad \text{for } n \to \infty \,.\end{aligned}$$

This is a contradiction to our hypothesis and thus completes the proof of Lemma 3.7. □

Now we give the proof of Lemma 3.6. If z would behave like a power law, we could have mainly used the estimate given in [4] to obtain our result. But unfortunately this is not the case everywhere, so that we have to introduce boundary layer estimates.

Proof of Lemma 3.6
For convenience, we denote $\alpha = \frac{\theta-1}{3-\theta}$. First the contributions where z is large are analyzed. For this, as can be seen from Assumption 3.2, we have to look at a specific domain of integration. So we show that for a smooth function ζ with $\zeta(0) = 0$

$$\left(\int_0^{2t^{-\alpha}} z^{(p-1)\theta} |\zeta|^p \, dx\right)^{\frac{1}{p}} \leq C\left(\int_0^{2t^{-\alpha}} z^\theta |\zeta_x|^2 \, dx\right)^{\frac{1}{2}}. \tag{23}$$

Indeed, due to Assumption 3.2 and with the change of variables $y = t^\alpha x$ and $\tilde{\zeta}(y) = \zeta(t^{-\alpha}y)$, we have

$$\left(\int_0^{2t^{-\alpha}} z^{(p-1)\theta} |\zeta|^p \, dx\right)^{\frac{1}{p}} \leq \left(\int_0^{2t^{-\alpha}} \frac{t^{\frac{2(p-1)\theta}{3-\theta}}}{(x^2t^{2\alpha}+a)^{\frac{(p-1)\theta}{\theta-1}}} |\zeta|^p \, dx\right)^{\frac{1}{p}}$$

$$= t^{\frac{2(p-1)\theta}{3-\theta}-\frac{\alpha}{p}} \left(\int_0^2 \frac{1}{(y^2+a)^{\frac{(p-1)\theta}{\theta-1}}} \left|\tilde{\zeta}\right|^p dy \right)^{\frac{1}{p}} \leq C t^{\frac{2(p-1)\theta}{3-\theta}-\frac{\alpha}{p}} \left(\int_0^2 \frac{1}{(y^2+a)^{\frac{p\theta}{\theta-1}}} \left|\tilde{\zeta}_x\right|^2 dy \right)^{\frac{1}{2}}$$

$$\leq C t^{\frac{2(p-1)\theta}{3-\theta}-\frac{\alpha}{p}-\frac{\theta}{3-\theta}-\frac{\alpha}{2}} \left(\int_0^{2t^{-\alpha}} z^\theta |\zeta_x|^2 dx \right)^{\frac{1}{2}} \leq C \left(\int_0^{2t^{-\alpha}} z^\theta |\zeta_x|^2 dx \right)^{\frac{1}{2}},$$

since $\frac{2(p-1)\theta}{3-\theta} - \frac{\alpha}{p} - \frac{\theta}{3-\theta} - \frac{\alpha}{2} = 0$. Next we do a further splitting

$$\zeta(x,t) = \eta(xt^\alpha)\zeta(x,t) + (1-\eta(xt^\alpha))\zeta(x,t) := \tilde{\zeta}(x,t) + \hat{\zeta}(x,t),$$

where η is a standard cut-off function such that $\eta(y) = 1$ for $y \leq 1$ and $\eta = 0$ if $y \geq 2$. Then, since $\tilde{\zeta}$ is supported in $[0, 2t^{-\alpha})$ and $\tilde{\zeta}(0) = 0$, using (23), we get

$$\left(\int_0^1 z^{(p-1)\theta} \left|\tilde{\zeta}\right|^p dx \right)^{\frac{1}{p}} \leq C \left(\int_0^1 z^\theta \left|\tilde{\zeta}_x\right|^2 dx \right)^{\frac{1}{2}}.$$

Because $\tilde{\zeta}_x = \eta(xt^\alpha)\zeta_x + t^\alpha \eta'(xt^\alpha)\zeta$, we obtain

$$\left(\int_0^1 z^{(p-1)\theta} \left|\tilde{\zeta}\right|^p dx \right)^{\frac{1}{p}} \leq C \left(\int_0^1 z^\theta |\zeta_x|^2 dx \right)^{\frac{1}{2}} + C \left(\int_0^1 z^\theta t^{2\alpha} \left|\eta'\zeta\right|^2 dx \right)^{\frac{1}{2}}. \tag{24}$$

We now give an estimate for the second term on the right hand side of (24). Noting that η' is supported in $(t^{-\alpha}, 2t^{-\alpha})$, we compute

$$\left(\int_0^1 z^\theta t^{2\alpha} \left|\eta'\zeta\right|^2 dx \right)^{\frac{1}{2}} \leq \left(\int_{t^{-\alpha}}^{2t^{-\alpha}} \frac{t^{\frac{2\theta}{3-\theta}}}{(x^2t^{2\alpha}+a)^{\frac{\theta}{\theta-1}}} t^{2\alpha} |\zeta|^2 dx \right)^{\frac{1}{2}}$$

$$= t^{\frac{2\theta}{3-\theta}+\frac{\beta}{2}} \left(\int_1^2 \frac{1}{(y^2+a)^{\frac{\theta}{\theta-1}}} |\zeta|^2 dy \right)^{\frac{1}{2}} \leq t^{\frac{2\theta}{3-\theta}+\frac{\beta}{2}} \left(\int_0^2 \frac{1}{(y^2+a)^{\frac{\theta}{\theta-1}}} |\zeta|^2 dy \right)^{\frac{1}{2}}$$

$$\leq C t^{\frac{2\theta}{3-\theta}+\frac{\beta}{2}} \left(\int_0^2 \frac{1}{(y^2+a)^{\frac{\theta}{\theta-1}}} |\zeta_y|^2 dy \right)^{\frac{1}{2}} \leq C \left(\int_0^{2t^{-\alpha}} z^\theta |\zeta_x|^2 dx \right)^{\frac{1}{2}}, \tag{25}$$

where we used $\psi_n(0) = 0$.
Combining (24) and (25), we obtain

$$\left(\int_I z^{(p-1)\theta} \left|\tilde{\zeta}\right|^p dx \right)^{\frac{1}{p}} \leq C \left(\int_I z^\theta |\zeta_x|^2 dx \right)^{\frac{1}{2}}.$$

It remains to show that

$$\left(\int_I z^{(p-1)\theta}\left|\hat{\zeta}\right|^p dx\right)^{\frac{1}{p}} \leq C\left(\int_I z^\theta |\zeta_x|^2 dx\right)^{\frac{1}{2}}. \tag{26}$$

Keeping in mind that $\hat{\zeta}$ vanishes in $[0, t^{-\alpha}]$, we note that z is comparable to $|x|^{-\frac{2}{\theta-1}}$. It is direct that $z \leq C|x|^{\frac{2}{\theta-1}}$. On the other hand, since $x > t^{-\alpha}$, we have $|x|^{-\frac{2}{\theta-1}} \leq C(x^2+t^{-\alpha})^{-\frac{1}{\theta-1}} \leq Cz$. Therefore,

$$\left(\int_I z^{(p-1)\theta}\left|\hat{\zeta}\right|^p dx\right)^{\frac{1}{p}} \leq C\left(\int_I x^{-\frac{2(p-1)\theta}{\theta-1}}\left|\hat{\zeta}\right|^p dx\right)^{\frac{1}{p}}$$

$$\leq C\left(\int_I x^{-\frac{2\theta}{\theta-1}}\left|\hat{\zeta}_x\right|^2 dx\right)^{\frac{1}{2}} \leq C\left(\int_I z^\theta\left|\hat{\zeta}_x\right|^2 dx\right)^{\frac{1}{2}},$$

where we used a known Sobolev inequality with weight (see e.g. [[7], Theorem 1 and corollaries in 2]).

For $\tilde{\zeta}$, we note that $\hat{\zeta}_x = (1-\eta(xt^\alpha))\zeta_x - t^\alpha\eta'(xt^\alpha)\zeta$.
Following a similar procedure as for the estimate (25), we can show without giving further details, that

$$\left(\int_I z^\theta\left|\hat{\zeta}_x\right|^2 dx\right)^{\frac{1}{2}} \leq C\left(\int_I z^\theta |\zeta_x|^2 dx\right)^{\frac{1}{2}}.$$

Summarizing the above estimates, we obtain

$$\left(\int_I z^{(p-1)\theta}\left|\hat{\zeta}\right|^p dx\right)^{\frac{1}{p}} \leq C\left(\int_I z^\theta |\zeta_x|^2 dx\right)^{\frac{1}{2}}. \tag{27}$$

Then estimates (26) and (27) lead to

$$\left(\int_0^1 z^{(p-1)\theta}|\zeta|^p dx\right)^{\frac{1}{p}} \leq \left(\int_0^1 z^{(p-1)\theta}\left|\tilde{\zeta}\right|^p dx\right)^{\frac{1}{p}} + \left(\int_0^1 z^{(p-1)\theta}\left|\hat{\zeta}\right|^p dx\right)^{\frac{1}{p}}$$

$$\leq C\left(\int_0^1 z^\theta |\zeta_x|^2 dx\right)^{\frac{1}{2}}.$$

This completes the proof of our lemma on the extension of the result given in [4]. □

Lemma 3.8 *Suppose that $z(x,t)$ and $v(x,t)$ satisfy the Assumption 3.2 and the Assumption 3.5, respectively. Then*

$$\langle v, v\rangle \leq \frac{C}{t^{\frac{\theta+5}{3-\theta}}} \qquad \text{and} \qquad |v(x,t)| \leq \frac{C}{t^{\frac{\theta+5}{2(3-\theta)}}} \quad \text{for} \quad |x| > \delta.$$

Proof. First we see, that

$$\int_I v v_t \frac{dx}{z^\theta} = \int_I \left(v_{xx} - \theta \left(\frac{z_x}{z} v \right)_x \right) v \frac{dx}{z^\theta} + \int_I \mathcal{R}(x,t) v \frac{dx}{z^\theta} =< v, \tilde{A}_z(v) > + < \mathcal{R}, v > \ .$$

Now we split the first term on the right hand side into half and since $< z^\theta, v >= 0$, due to Proposition 3.4, we have $\frac{1}{2} < v, \tilde{A}_z(v) >\leq -C < v, v >$ and thus obtain

$$\frac{d}{dt} < v, v > + \frac{C}{2} < v, v > + \frac{1}{2} < v_x - \theta \frac{z_x}{z} v, v_x - \theta \frac{z_x}{z} v >\leq |< \mathcal{R}, v >| + \frac{C}{t} < v, v > .$$

Using Hölder's inequality and (18), we have

$$\frac{d}{dt} \|v\|^2_{L^2(z^{-\theta}dx)} + C \|v\|^2_{L^2(z^{-\theta}dx)} + C \left\| v_x - \theta \frac{z_x}{z} v \right\|^2_{L^2(z^{-\theta}dx)} \leq \|\mathcal{R}\|_{L^{p'}(z^{-\theta}dx)} \|v\|_{L^p(z^{-\theta}dx)}$$

$$\leq C_\epsilon \|\mathcal{R}\|^2_{L^{p'}(z^{-\theta}dx)} + \epsilon \|v\|^2_{L^p(z^{-\theta}dx)} \leq C_\epsilon \|\mathcal{R}\|^2_{L^{p'}(z^{-\theta}dx)} + C \cdot \epsilon \left\| v_x - \theta \frac{z_x}{z} v \right\|^2_{L^2(z^{-\theta}dx)},$$

where p is given as in (18) and $p' = (6\theta - 2)/(5\theta - 3)$ is its Hölder conjugate. Summing up, we obtain

$$\frac{d}{dt} \|v\|^2_{L^2(z^{-\theta}dx)} + C \|v\|^2_{L^2(z^{-\theta}dx)} + C \left\| v_x - \theta \frac{z_x}{z} v \right\|^2_{L^2(z^{-\theta}dx)} \leq C_\epsilon \|\mathcal{R}\|^2_{L^{p'}(z^{-\theta}dx)} .$$

Due to Assumption 3.2, we compute

$$\|\mathcal{R}\|^2_{L^{p'}(z^{-\theta}dx)} = \left(\int \left| \frac{z^{\theta-1}u}{\int z^\theta dx} \right|^{p'} \frac{dx}{z^\theta} \right)^{\frac{2}{p'}} \leq \frac{C}{(\int z^\theta dx)^4} \left(\int z^{(2\theta-1)p' - \theta} dx \right)^{\frac{2}{p'}}$$

$$\leq C t^{-\frac{4(\theta+1)}{3-\theta}} t^{\frac{4(2\theta-1)p' - \theta(3-\theta) - (\theta-1)}{p'(3-\theta)}} \leq C t^{-\frac{\theta+5}{3-\theta}}.$$

Therefore, $< v, v >\leq C t^{-\frac{\theta+5}{3-\theta}}$ and so $|v(x,t)| \leq C t^{-\frac{\theta+5}{2(3-\theta)}}$ for $|x| > \delta$. This completes the proof. □

3.2 Estimates for the solution near $x = 0$

We introduce an internal variable in the following way:

$$\xi = t^{\frac{\theta-1}{3-\theta}} x, \qquad v(x,t) = t^{\frac{\theta-1}{3-\theta}} G(\xi, t), \qquad z(x,t) = t^{\frac{2}{3-\theta}} Z(\xi, t) \ , \tag{28}$$

and let $\alpha = (\theta - 1)/(3 - \theta)$ and $\gamma = 2/(3 - \theta)$. Due to Lemma 3.8, we have

$$|G(\xi, t)| \leq C t^{-\frac{\theta+5}{2(3-\theta)} - \frac{\theta-1}{3-\theta}} = C t^{\frac{-\theta-5-2\theta+2}{2(3-\theta)}} = C t^{-\frac{3(\theta+1)}{2(3-\theta)}} \quad \text{for } |\xi| \geq t^\alpha \delta \quad \text{for any } \delta > 0 \ .$$

If z satisfies Assumption 3.2, then $Z(\xi,t) \approx (\xi^2+a)^{-\frac{1}{\theta-1}}$. Furthermore, under Assumption 3.5, one can easily see that

$$|G(\xi,t)| \le M\frac{Z^\theta}{\Gamma(t)}, \qquad \text{with } \Gamma(t) = \int_{-t^\alpha}^{t^\alpha} Z^\theta(\xi,t)d\xi.$$

Since $\Gamma(t) \le C$ for all $t>0$, we obtain $|G(\xi,t)| \le CMZ^\theta$. Recalling (17), in terms of the new variables, simple computations show that

$$\mathcal{R}(\xi,t) = \theta t^{\alpha-1}\left(\frac{Z^{2\theta-1}}{\Gamma^2(t)} + \frac{Z^{\theta-1}G}{\Gamma^2(t)} + \frac{Z^\theta\Lambda(t)}{\Gamma^3(t)} + \frac{Z^\theta\Upsilon(t)}{\Gamma^2(t)}\right),$$

where

$$\Lambda(t) = \int_{-t^\alpha}^{t^\alpha} Z^{2\theta-1}(\xi,t)d\xi, \quad \Upsilon(t) = \int_{-t^\alpha}^{t^\alpha} Z^{\theta-1}(\xi,t)G(\xi,t)d\xi.$$

It is direct that $\Gamma(t), \Lambda(t)$, and $\Upsilon(t)$ are uniformly bounded for any t as long as z and v satisfy Assumptions 3.2 and 3.5, respectively. For convenience, denote $\mathcal{R} = t^{\alpha-1}\mathcal{R}_1 + \theta t^{\alpha-1}Z^{\theta-1}\Gamma^{-2}(t)G$, where

$$\mathcal{R}_1(\xi,t) = \theta\left(\frac{Z^{2\theta-1}}{\Gamma^2(t)} + \frac{Z^\theta\Lambda(t)}{\Gamma^3(t)} + \frac{Z^\theta\Upsilon(t)}{\Gamma^2(t)}\right).$$

By change of variable, due to (16), G solves

$$\frac{\theta-1}{3-\theta}t^{\frac{\theta-1}{3-\theta}-1}\left(G+\xi\frac{\partial G}{\partial\xi}\right) + t^{\frac{\theta-1}{3-\theta}}\frac{\partial G}{\partial t} = t^{\frac{3(\theta-1)}{3-\theta}}\left[G_{\xi\xi} - \theta\left(G\frac{Z_\xi}{Z}\right)_\xi\right] + \mathcal{R}(\xi,t). \tag{29}$$

Simplifying (29), we have

$$G_{\xi\xi} - \theta\left(G\frac{Z_\xi}{Z}\right)_\xi = \alpha t^{-2\alpha-1}\left(G+\xi\frac{\partial G}{\partial\xi}\right) + t^{-2\alpha}\frac{\partial G}{\partial t} - \theta t^{-2\alpha-1}\frac{Z^{\theta-1}}{\Gamma^2(t)}G + t^{-2\alpha-1}\mathcal{R}_1.$$

The next Lemma shows the asymptotic behavior of u under Assumption 3.2.

Lemma 3.9 *If $z(x,t)$ satisfies Assumption 3.2, then*

$$\left|u(x,t) - \frac{z^\theta}{\int_I z^\theta dx}\right| \le \varepsilon(t)\frac{z^\theta}{\int_I z^\theta dx},$$

where $\varepsilon(t) \le Ct^{-\beta}$ for some $\beta>0$.

The proof of Lemma 3.9 relies on

Lemma 3.10 *Suppose that $z(x,t)$ and $v(x,t)$ satisfy Assumption 3.2 and Assumption 3.5, respectively. Let G be defined as in (28) so that G solves the equation (29). Then there exists a super solution for G in the set $\xi \le \delta t^{(\theta-1)/(3-\theta)}$ with a sufficiently small $\delta>0$.*

Proof. First, we look for a super-solution of the form

$$\mathcal{G}_1(\xi,t) := \hat{S}(\xi,t) + \hat{U}(\xi,t) = t^{-(2\alpha+1)}S(\xi,t) + t^{-2(2\alpha+1)}U(\xi,t),$$

where

$$S(\xi,t) = Z^\theta(\xi,t)\int_0^\xi Z^{-\theta}(y,t)\int_y^\infty \mathcal{R}_1(\eta,t)d\eta dy,$$

and $\hat{U}$ solves

$$U_{\xi\xi} - \theta\left(U\frac{Z_\xi}{Z}\right)_\xi = \frac{K_1}{(\xi^2+a)^{\frac{1}{\theta-1}}}.$$

Here K_1 is a constant, which will be specified later. Since $\mathcal{R} \approx Z^\theta$, up to multiplicative constants depending on M, one can check that $S_{\xi\xi} - \theta\left(\frac{Z_\xi}{Z}S\right)_\xi \approx \mathcal{R}_1$ and

$$|S| + |\xi S_\xi| \approx \frac{1}{(\xi^2+a)^{\frac{1}{\theta-1}}}, \qquad |S_t| \approx \frac{1}{t(\xi^2+a)^{\frac{1}{\theta-1}}}, \tag{30}$$

again, all up to multiplicative constants depending on M. Similarly, we can show

$$|U| + |\xi U_\xi| \approx \frac{1}{(\xi^2+a)^{\frac{2-\theta}{\theta-1}}}, \qquad |U_t| \approx \frac{1}{t(\xi^2+a)^{\frac{2-\theta}{\theta-1}}}. \tag{31}$$

Now we define a differential operator $\mathcal{H}_Z$ as follows:

$$\mathcal{H}_Z(f) = -t^{-2\alpha}\frac{\partial f}{\partial t} + f_{\xi\xi} - \theta\left(\frac{Z_\xi}{Z}f\right)_\xi - \alpha t^{-2\alpha-1}\left(f + \xi\frac{\partial f}{\partial \xi}\right) + \theta t^{-2\alpha-1}\frac{Z^{\theta-1}}{\Gamma^2(t)}f.$$

And compute

$$\begin{aligned}
\mathcal{H}_Z(\mathcal{G}_1) &= -t^{-2\alpha}\frac{\partial \mathcal{G}_1}{\partial t} + t^{-2\alpha-1)}\mathcal{R}_1 + t^{-2(2\alpha+1)}\frac{K_1}{(\xi^2+a)^{\frac{1}{\theta-1}}} \\
&\quad -\alpha t^{-2\alpha-1}\left(\mathcal{G}_1 + \xi\frac{\partial \mathcal{G}_1}{\partial \xi}\right) + \theta t^{-2\alpha-1}\frac{Z^{\theta-1}}{\Gamma^2(t)}\mathcal{G}_1 \\
&= t^{-2(2\alpha+1)}\left(\frac{K_1}{(\xi^2+a)^{\frac{1}{\theta-1}}} - \alpha(S+\xi S_\xi) + \theta Z^{\theta-1}S - t^{2\alpha+2}\frac{\partial}{\partial t}(t^{-(2\alpha+1)}S)\right) \\
&\quad + t^{-3(2\alpha+1)}\left(\theta Z^{\theta-1}U - \alpha(U+\xi U_\xi) - t^{2\alpha+2}\frac{\partial}{\partial t}(t^{-2(2\alpha+1)}U)\right) + t^{-2\alpha-1}\mathcal{R}_1. \\
&\approx t^{-2(2\alpha+1)}(K_1+1)(\xi^2+a)^{-\frac{1}{\theta-1}} + t^{-3(2\alpha+1)}(\xi^2+a)^{-\frac{2-\theta}{\theta-1}} + t^{-2\alpha-1}\mathcal{R}_1,
\end{aligned} \tag{32}$$

where we used (30) and (31) and where $C_{\alpha,\theta}$ is a constant depending on α and θ.

Next we are looking for a super-solution of (29), which is of the form

$$\bar{G}(\xi,t)=\gamma(t)Z^{\theta}(\xi,t)+t^{-2\alpha-1}\gamma(t)\psi(\xi,t)+e^{-\mu(t-\bar{t})}Q(\xi,t),$$

where $\bar{t}$ in the last term is fixed and

$$\gamma(t)=C_{\delta}t^{-\frac{1}{2}},\qquad \psi(\xi,t)=K_2Z^{\theta}(\xi,t)\int_0^{\xi}Z^{-\theta}(y,t)\int_y^{\infty}Z^{\theta}(\nu,t)d\nu dy,$$

with constants K_2 and μ, which will be specified later, and C_δ with $C_\delta>2C$, where C is the absolute constant appearing in Lemma 3.8. For convenience, denote

$$\mathcal{G}_2:=\gamma(t)Z^{\theta}(\xi,t)+t^{-2\alpha-1}\gamma(t)\psi(\xi,t),\qquad \mathcal{G}_3:=e^{-\mu(t-\bar{t})}Q(\xi,t).$$

We have

$$\psi_{\xi\xi}-\theta\left(\frac{Z_\xi}{Z}\psi\right)_\xi=\frac{K_2}{(\xi^2+a)^{\frac{\theta}{\theta-1}}},\tag{33}$$

$$|\psi|+|\xi\psi_\xi|\approx\frac{1}{(\xi^2+a)^{\frac{1}{\theta-1}}},\qquad |\psi_t|\approx\frac{1}{t(\xi^2+a)^{\frac{1}{\theta-1}}}\ .\tag{34}$$

With (33) and (34), we can show that

$$\mathcal{H}_Z(\mathcal{G}_2)=-t^{-2\alpha}\frac{\partial\mathcal{G}_2}{\partial t}+t^{-2\alpha-1}\gamma(t)\frac{K_2}{(\xi^2+a)^{\frac{\theta}{\theta-1}}}-\alpha t^{-2\alpha-1}\left(\mathcal{G}_2+\xi\frac{\partial\mathcal{G}_2}{\partial\xi}\right)+t^{-2\alpha-1}\theta Z^{\theta-1}\mathcal{G}_2$$

$$\approx t^{-2\alpha-1}\gamma(t)\frac{1+K_2}{(\xi^2+a)^{\frac{\theta}{\theta-1}}}+t^{-4\alpha-2}\gamma(t)\left(\frac{1}{(\xi^2+a)^{\frac{\theta}{\theta-1}}}+\frac{1}{(\xi^2+a)^{\frac{1}{\theta-1}}}\right).\tag{35}$$

Finally, choose $\mathcal{G}_3=e^{-\mu(t-\bar{t})}Q(\xi,t)$ where Q satisfies

$$-t^{-2\alpha}Q_t+Q_{\xi\xi}-\theta\left(Q\frac{Z_\xi}{Z}\right)_\xi\le\alpha t^{-2\alpha-1}\left(Q+\xi\frac{\partial Q}{\partial\xi}\right)-\theta t^{-2\alpha-1}\frac{Z^{\theta-1}}{\Gamma^2(t)}Q-\mu t^{-2\alpha}Q\tag{36}$$

as well as $Q(\xi,t)>0$ on the boundary $|\xi|=\delta t^{\frac{\theta-1}{3-\theta}}$. We obtain a solution satisfying (36) in a perturbative manner. To do this we take $Q_0(\xi,t)=a(Z(\xi,t))^{\theta}$, where a is a constant of order one to be determined. Then Q_0 solves

$$Q_{0,\xi\xi}-\theta\left(Q_0\frac{Z_\xi}{Z}\right)_\xi=0.\tag{37}$$

We look for solutions of (36) of the form

$$Q\left(\xi,t\right)=Q_0\left(\xi,t\right)+Q_1\left(\xi,t\right),$$

where Q_0 is given in (37) and Q_1 satisfies

$$Q_{1,\xi\xi} - \theta\left(Q_1\frac{Z_\xi}{Z}\right)_\xi \leq -2\Big(\alpha t^{-2\alpha-1}Q_0 + \alpha t^{-2\alpha-1}\xi\left|\frac{\partial Q_0}{\partial\xi}\right| + \theta t^{-2\alpha-1}\frac{Z^{\theta-1}}{\Gamma^2(t)}Q_0 + \mu t^{-2\alpha}Q_0 + t^{-2\alpha}\left|Q_{0,t}\right|\Big) \tag{38}$$

with $Q_1(0,t) = 0$. Now it remains show that $Q = Q_0 + Q_1$ satisfies (36). Suppose that δ is sufficiently small. Assume that Q_1 satisfies

$$|Q_1| \leq Q_0 \ , \quad \left|\frac{\partial Q_1}{\partial\xi}\right| \leq \left|\frac{\partial Q_0}{\partial\xi}\right| \ , \quad \left|\frac{\partial Q_1}{\partial t}\right| \leq \left|\frac{\partial Q_0}{\partial t}\right| \tag{39}$$

in the set $|\xi| \leq \delta t^{\frac{\theta-1}{3-\theta}}$. We will check this condition "a posteriori". First we prove (36). We compute the following quantity

$$J \equiv -t^{-2\alpha}Q_t + Q_{\xi\xi} - \theta\left(Q\frac{Z_\xi}{Z}\right)_\xi - \alpha t^{-2\alpha-1}\left(Q + \frac{\partial Q}{\partial\xi}\right) + \theta t^{-2\alpha-1}\frac{Z^{\theta-1}}{\Gamma^2(t)}Q + \mu t^{-2\alpha}Q.$$

Using $Q = Q_0 + Q_1$ as well as (37), we obtain

$$J = Q_{1,\xi\xi} - \theta\left(Q_1\frac{Z_\xi}{Z}\right)_\xi - t^{-2\alpha}Q_{0,t} - t^{-2\alpha}Q_{1,t} - \alpha t^{-2\alpha-1}\left(Q_0 + \frac{\partial Q_0}{\partial\xi}\right)$$

$$-\alpha t^{-2\alpha-1}\left(Q_1 + \frac{\partial Q_1}{\partial\xi}\right) + \theta t^{-2\alpha-1}\frac{Z^{\theta-1}}{\Gamma^2(t)}Q_0 + \theta t^{-2\alpha-1}\frac{Z^{\theta-1}}{\Gamma^2(t)}Q_1 + \mu t^{-2\alpha}Q_0 + \mu t^{-2\alpha}Q_1.$$

Thus it is immediate that

$$\begin{aligned} J \leq\ & Q_{1,\xi\xi} - \theta\left(Q_1\frac{Z_\xi}{Z}\right)_\xi \\ & + \left[\alpha t^{-2\alpha-1}Q_0 + \alpha t^{-2\alpha-1}\xi\left|\frac{\partial Q_0}{\partial\xi}\right| + \theta t^{-2\alpha-1}\frac{Z^{\theta-1}}{\Gamma^2(t)}Q_0 + \mu t^{-2\alpha}Q_0 + t^{-2\alpha}\left|Q_{0,t}\right|\right] \\ & + \left[\alpha t^{-2\alpha-1}Q_1 + \alpha t^{-2\alpha-1}\xi\left|\frac{\partial Q_1}{\partial\xi}\right| + \theta t^{-2\alpha-1}\frac{Z^{\theta-1}}{\Gamma^2(t)}Q_{10} + \mu t^{-2\alpha}Q_1 + t^{-2\alpha}\left|Q_{1,t}\right|\right]. \end{aligned}$$

Using the inequalities in (39), we have

$$\begin{aligned} J \leq\ & Q_{1,\xi\xi} - \theta\left(Q_1\frac{Z_\xi}{Z}\right)_\xi \\ & + 2\left[\alpha t^{-2\alpha-1}Q_0 + \alpha t^{-2\alpha-1}\xi\left|\frac{\partial Q_0}{\partial\xi}\right| + \theta t^{-2\alpha-1}\frac{Z^{\theta-1}}{\Gamma^2(t)}Q_0 + \mu t^{-2\alpha}Q_0 + t^{-2\alpha}\left|Q_{0,t}\right|\right]. \end{aligned}$$

With (38), we obtain $J \leq 0$, thus (36) follows.

Now we need to verify (39). We decompose Q_1 as a sum of $Q_{1,1}$ and $Q_{1,2}$, which solve

$$Q_{1,1,\xi\xi} - \theta\left(Q_{1,1}\frac{Z_\xi}{Z}\right)_\xi = -2\left[\alpha t^{-2\alpha-1}Q_0 + \alpha t^{-2\alpha-1}\xi\left|\frac{\partial Q_0}{\partial \xi}\right| + \theta t^{-2\alpha-1}\frac{Z^{\theta-1}}{\Gamma^2(t)}Q_0 + t^{-2\alpha}\left|Q_{0,t}\right|\right],$$
$$Q_{1,2,\xi\xi} - \theta\left(Q_{1,2}\frac{Z_\xi}{Z}\right)_\xi = -2\mu t^{-2\alpha}Q_0\,,$$

$$Q_{1,1}(0,t) = Q_{1,2}(0,t) = 0\,.$$

We will focus just on $Q_{1,2}$ since the analysis of $Q_{1,1}$ is similar and understanding $Q_{1,2}$ is more important in order to judge the role of μ. We are interested in obtaining a particular solution for this differential equation. Because the equation for $Q_{1,2}$ can be rewritten as $\left(Z^\theta\left(Z^{-\theta}Q_{1,2}\right)_\xi\right)_\xi = -2\mu t^{-2\alpha}Q_0$, after integration we choose

$$\left(Z^{-\theta}Q_{1,2}\right)_\xi = 2\mu t^{-2\alpha}Z^{-\theta}\int_\xi^{\delta(\bar{t})^{(\frac{\theta-1}{3-\theta})}} Q_0(\eta,t)\,d\eta.$$

Using $Q_{1,2}(0,t) = 0$, we have

$$Q_{1,2}(\xi,t) = 2\mu t^{-2\alpha}\left(Z(\xi,t)\right)^\theta\int_0^\xi d\lambda\left[\left(Z(\lambda,t)\right)^{-\theta}\int_\lambda^{\delta(\bar{t})^{(\frac{\theta-1}{3-\theta})}} Q_0(\eta,t)\,d\eta\right].$$

We can now estimate the behavior of $Q_{1,2}(\xi,t)$ for $\xi \gg 1$ and see how we choose μ. Using Assumption 3.2, it follows that Q_0 behaves like $\xi^{-\frac{2\theta}{\theta-1}}$ for large ξ. It is then easy to see that $Q_{1,2}$, up to multiplicative constants, behaves like

$$Q_{1,2} \approx \mu t^{-2\alpha}\frac{1}{\xi^{\frac{2\theta}{\theta-1}}}\xi^2 \approx \mu t^{-2\alpha}\xi^{-\frac{2}{\theta-1}}$$

for large ξ, by recalling that $\alpha = \frac{\theta-1}{3-\theta}$. Now we can compare Q_0 with $Q_{1,2}$. Note that $Q_0 > 0$ for $|\xi| \approx \delta t^{\frac{\theta-1}{3-\theta}}$. Moreover

$$Q_0 \approx \xi^{-\frac{2\theta}{\theta-1}}, \qquad Q_{1,2} \approx \mu t^{-2\alpha}\xi^{-\frac{2}{\theta-1}}.$$

Therefore, for μ of order one and δ small it follows that $|Q_{1,2}| \ll Q_0$. In a similar manner, we can show that $|(Q_{1,2})_\xi| \ll |(Q_0)_\xi|$ and $|(Q_{1,2})_t| \ll |(Q_0)_t|$. Details are omitted. This completes the estimate (39).

So, we conclude that $\mathcal{H}_Z(\mathcal{G}_3) \le 0$, which yields $\mathcal{H}_Z(\mathcal{G}) \le 0$. Indeed, together with (32), (35), we obtain

$$\begin{aligned}
&\mathcal{H}_Z(\mathcal{G}_1+\mathcal{G}_2+\mathcal{G}_3-G) \le \mathcal{H}_Z(\mathcal{G}_1)+\mathcal{H}_Z(\mathcal{G}_2)-\mathcal{H}_Z(G)\\
&\approx t^{-2(2\alpha+1)}(K_1+1)(\xi^2+a)^{-\frac{1}{\theta-1}} + t^{-3(2\alpha+1)}(\xi^2+a)^{-\frac{2-\theta}{\theta-1}}\\
&+t^{-2\alpha-1}\gamma(t)\frac{1+K_2}{(\xi^2+a)^{\frac{\theta}{\theta-1}}} + t^{-4\alpha-2}\gamma(t)\left(\frac{1}{(\xi^2+a)^{\frac{\theta}{\theta-1}}}+\frac{1}{(\xi^2+a)^{\frac{1}{\theta-1}}}\right),
\end{aligned}$$

where we used that $\mathcal{H}_Z(\mathcal{G}) = t^{-2\alpha-1}\mathcal{R}_1$. Suppose that t is as large as needed, which can be obtained by setting $\bar{t} \ge t_0$ for an arbitrary large number t_0. By choosing constants K_1 and K_2 such that $K_1+1<0$ and $K_2+1<0$, we can obtain that $\mathcal{H}_Z(\mathcal{G}_1+\mathcal{G}_2+\mathcal{G}_3-G)<0$.

In order to apply the maximum principle, we need $\mathcal{G}_1+\mathcal{G}_2+\mathcal{G}_3 > G$ for $t=\bar{t}$ and $G \ge Ct^{-\frac{3(\theta+1)}{2(3-\theta)}}$ for $|\xi| = \delta t^\alpha$.

The positivity of $\mathcal{G}_1+\mathcal{G}_2+\mathcal{G}_3-G$ for $t=\bar{t}$ is due to the fact that $\mathcal{G}_3$ is the largest term among $\{\mathcal{G}_i : i=1,2,3\}$ and $\mathcal{G}_3 > G$ for $t=\bar{t}$. On the other hand, at the boundary $|\xi| = \delta t^\alpha$ the inequality $G \ge Ct^{-\frac{3(\theta+1)}{2(3-\theta)}}$ results from the fact that $\mathcal{G}_3>0$ and $\mathcal{G}_2 > Ct^{-\frac{3(\theta+1)}{2(3-\theta)}}$ for $|\xi| = \delta t^\alpha$. Note that $\mathcal{G}_1$ is added to control the "small nonlinear terms", which are very small compared with $\mathcal{G}_2$. Summing up all above given, we conclude that $\mathcal{G}_1+\mathcal{G}_2+\mathcal{G}_3 \ge G$ is a super-solution for G. □

With this construction of a super-solution above, we can now prove Theorem 3.9.

Proof of Lemma 3.9 : Since the super-solution given above is bounded by $Ct^{-\frac{1}{2}}Z^\theta(\xi,t)$ for large t with $t \ge \bar{t} + K\log(\bar{t})$, it follows that there exists $\beta>0$ such that the super-solution is bounded by $Ct^{-\beta}Z^\theta(\xi,t)$ for any $t \ge t_0$, and thus, back in the original variable, we obtain

$$\left| u(x,t) - \frac{z^\theta}{\int_I z^\theta dx}\right| = t^{\frac{\theta-1}{3-\theta}}|G(\xi,t)| \le Ct^{-\beta}t^{\frac{\theta-1}{3-\theta}}\frac{Z^\theta(\xi,t)}{\int_I Z^\theta(\xi,t)d\xi} = Ct^{-\beta}\frac{z^\theta(x,t)}{\int_I z^\theta(x,t)dx},$$

where we used $\int_I Z^\theta(\xi,t)d\xi \le C$, with $C=C(\theta,M)$ depends on. This completes the proof of our lemma. □

Finally we conclude the proof of the main theorem in this section with

Lemma 3.11 *There exist solutions u, z which satisfy all conditions of Assumption 3.2 for all $t \ge t_0$.*

Proof. Without loss of generality, the initial time of our problem is t_0, since the system under consideration is invariant under time translations $t \to t - t_0$. Our choice of initial data $u(\cdot,t_0)$ and $z(\cdot,t_0)$ is sufficiently smooth and moreover, $u(\cdot,t_0)$ is assumed to be very close to the expected asymptotic behavior $t^{\frac{\theta-1}{3-\theta}}\left(Bx^2t^{\frac{2(\theta-1)}{3-\theta}}+A\right)^{-\frac{1}{\theta-1}}$.

We begin proving the L^∞-estimate for z according to Assumption 3.2, 2. By Lemma 3.9 we have

$$\left| z_t - \frac{z^\theta}{\int_I z^\theta dx} \right| \leq \varepsilon(t) \frac{z^\theta}{\int_I z^\theta dx}.$$

Integrating this equation starting from $t = t_0$, exactly as we did in the formal computations at the begining of Section 3 we obtain 2. in Assumption 3.2, which implies that z blows up in infinite time. More precisely, if for the initial data we have

$$\left| z_0(x,t_0) - \frac{t_0^{\frac{2}{3-\theta}}}{\left(Bx^2 t_0^{\frac{2(\theta-1)}{3-\theta}} + A \right)^{\frac{1}{\theta-1}}} \right| \leq \frac{1}{2} \frac{t_0^{\frac{2}{3-\theta}}}{\left(Bx^2 t_0^{\frac{2(\theta-1)}{3-\theta}} + A \right)^{\frac{1}{\theta-1}}} .$$

Therefore we recover 2. in Assumption 3.2 with M replaced by $\frac{M}{2}$ for $t_0 \leq t < \infty$, if M is sufficiently large and then t_0 chosen accordingly large enough.

Finally we derive the estimates for the derivatives and the Hölder norms in 1.,3., and 4. of Assumption 3.2. The arguments are similar as those given in [2] and [3]. Suppose that $\bar{t} \geq t_0$. We introduce a characteristic length R satisfying $\frac{1}{(\bar{t})^{(\frac{2(\theta-1)}{3-\theta})}} \leq R < 1$. Using the new variables $y = x/R$ and $\tau = (t - \bar{t})/R^2$, we define

$$v_R(y,\tau) := R^{\frac{2\theta}{\theta-1}} v(Ry, \bar{t} + R^2\tau), \quad z_R(y,\tau) := R^{\frac{2}{\theta-1}} z(Ry, \bar{t} + R^2\tau).$$

Then, for $\tau \in (0,1)$ and $|y| \in (1/2, 3/2)$, we have

$$|v_R(y,\tau)| \leq \frac{2\epsilon(\bar{t})}{(\bar{t})^{\frac{\theta+1}{3-\theta}}} \ , \ |z_R(y,\tau)| \leq 2.$$

On the other hand v_R and z_R satisfy

$$v_{R,\tau} = v_{R,yy} - \theta \left(\frac{z_{R,y}}{z_R} v_R \right)_y - \frac{1}{R^2} \left(\frac{z_R^\theta}{\alpha(\tau)} \right)_\tau , \tag{40}$$

$$z_{R,\tau} = \frac{z_R^\theta}{\alpha(\tau)} + v_R, \tag{41}$$

with

$$\alpha(\tau) = \int_I z^\theta dx \approx (\bar{t})^{(\frac{\theta+1}{3-\theta})}.$$

The term $\left(\frac{z_R^\theta}{\alpha(\tau)} \right)_\tau$ can be shown to be sufficiently smooth and small by using (41), since

$$\left(\frac{z_R^\theta}{\alpha(\tau)} \right)_\tau = \frac{\theta z_R^{\theta-1}}{\alpha(\tau)} \left(\frac{z_R^\theta}{\alpha(\tau)} + v_R \right) - \frac{\alpha'(\tau)}{\alpha^2(\tau)} z_R^\theta.$$

Note that $\alpha'(\tau) \approx (\bar{t})^{\frac{2(\theta-1)}{3-\theta}}$. One can easily see that the above terms are small contributions compared to other terms on the right hand side of (40). In order to obtain $\mathcal{C}^{2+\nu}$ estimates, we first take two spatial derivatives in (41) and obtain

$$\left(\frac{\partial^2 z_R}{\partial y^2}\right)_\tau = \frac{\theta(\theta-1) z_R^{\theta-2}}{\alpha(\tau)} \left(\frac{\partial z_R}{\partial y}\right)^2 + \frac{\theta z_R^{\theta-1}}{\alpha(\tau)} \frac{\partial^2 z_R}{\partial y^2} + \frac{\partial^2 v_R}{\partial y^2}.$$

The above equation indicates that we have to control $\frac{\partial^2 v_R}{\partial y^2}$. In fact, an interior regularity result for v_R in the region $\frac{3}{4} \le |y| \le \frac{5}{4}$ is needed. We introduce a cutoff $\xi(y)$ which equals 1 for $\frac{3}{4} \le |y| \le \frac{5}{4}$ and vanishes for $|y-1| > \frac{1}{2}$. Then for $\xi(y) v_R =: \bar{v}_R$ it follows

$$\bar{v}_{R,\tau} = \bar{v}_{R,yy} - \theta \left(\frac{z_{R,y}}{z_R} \bar{v}_R\right)_y - 2 v_{R,y} \xi_y - v_R \xi_{yy} + \theta \left(\frac{z_{R,y}}{z_R} v_R \xi_y\right) - \frac{1}{R^2} \left(\frac{z_R^\theta \xi}{\alpha(\tau)}\right)_\tau.$$

The equation for $\bar{v}_R$ is similar to the one for v_R except for some source terms that are of order $\frac{\epsilon(\bar{t})}{\bar{t}^{\frac{\theta+1}{3-\theta}}}$. Since $\bar{v}_R$ vanishes, it follows that as long as z_R satisfies Assumption 3.1, the fundamental solution of the equation satisfied by $\bar{v}_R$ decreases exponentially in τ, and the $C^{2,\nu}$-derivatives in space also decay exponentially by standard regularizing effects. More precisely, we obtain two types of contributions for the derivatives of $\bar{v}_R$, one of which is the part associated to the initial data starting at $t = \bar{t}$ that decreases exponentially, and a second part associated to the source term which is of order $\frac{\epsilon(\bar{t})}{(\bar{t})^{\frac{\theta+1}{3-\theta}}}$. Due to the decay of the function $\frac{1}{\alpha(\tau)}$, we can obtain a similar decay for the derivatives of z_R and the Hölder estimates, by using derivatives of v_R as source terms in the equation (41). This gives the desired estimate for any $t \ge 2$. If $t \le 2$ we obtain similar results for $\|v_R(t)\|_{C^{2,\nu}}, \|z_R\|_{C^{2,\nu}}$ using the regularity of the initial data $v_0(x), z_0(x)$. In particular for $t \in [\bar{t}, \bar{t}+1]$ we can derive

$$\|v_R(\bar{t}+1)\|_{\mathcal{C}^{2,\nu}} \le \sigma \|v_R(\bar{t})\|_{\mathcal{C}^{2,\nu}} + \frac{C\epsilon(\bar{t})}{(\bar{t})^{\frac{\theta+1}{3-\theta}}},$$
$$\|z_R(\bar{t}+1)\|_{\mathcal{C}^{2,\nu}} \le \sigma \|z_R(\bar{t})\|_{\mathcal{C}^{2,\nu}} + C\epsilon(\bar{t}),$$

where $0 < \sigma < 1$ due to the exponential decay of the solutions for the initial data mentioned above. The main contribution is due to the sources. Usual iterative methods yield the global smallness estimates as desired. Taking the supremum for all the admissible values of R and returning to the original variables (x,t), we obtain estimates for the Hölder norms defined in Assumption 3.2. This completes the proof of our main theorem. □

Acknowledgement:
This paper was done while all three authors were at the Max-Planck-Institute for Mathematics in the Sciences, in Leipzig, Germany. Additionally the first author was partially supported by KRF-2006-331-C00020. The third author was also supported by the Humboldt foundation and by DGES Grant MTM2007-61755. Further support was given by The International Graduiertenkolleg IGK 710, Heidelberg, funded by the Deutsche Forschungsgemeinschaft, (DFG).

References

[1] R. Courant & D. Hilbert Methods of Mathematical Physics. Reprint of the 1962 original. Wiley Classics Library (1989), Wiley & Sons, New York.

[2] M.A. Herrero & J.J.L. Velazquez *Singularity patterns in a chemotaxis model.* Math. Ann. **306** (1996), 583–623.

[3] M.A. Herrero & J.J.L. Velazquez *A blow-up mechanism for a chemotaxis model.* Ann. Scuola Norm. Sup. Pisa **XXIV** (1997), 1739–1754.

[4] T. Horiuchi *Best constant in weighted Sobolev inequality with weights being powers of distance from the origin*, J. of Inequal. & Appl. **1** (1997), no. 3, 275–292.

[5] E. Keller & L. Segel *Traveling bands of chemotactic bacteria:A theoretical analysis*, J. Theor. Biol. **30** (1971), 235–248.

[6] H. Levine & B. Sleeman *A system of reaction diffusion equations arising in the theory of reinforced random walks.* SIAM J. Appl. Math **57** (1997), no. 3, 683–730.

[7] V.G. Maz'ja *Sobolev spaces* (1985), Springer Verlag, Berlin.

[8] H. G. Othmer & A. Stevens *Aggregation, blowup, and collapse: the ABC's of taxis in reinforced random walks.* SIAM J. Appl. Math. **57** (1997), no. 3, 1044-1081.

[9] M. Rascle *Sur uné equation intégro-différentielle non lineaire issue de la biologie*, J. Diff. Equ. **32** (1979), no. 3, 420–453.

[10] H. Schwetlick, *personal communication.*

[11] A. Stevens *Trail following and aggregation of myxobacteria.* J. of Biol. Systems **3** (1995), 1059–1068.

[12] M. Struwe *Variational methods. Applications to nonlinear differential equations and Hamiltonian systems*, (2000), Springer Verlag, Berlin.

[13] Y. Yang, H. Chen & W. Liu *On existence of global solutions and blow-up to a system of reaction diffusion equations modelling chemotaxis*, SIAM J. Math. Anal. **33** (2001), no. 4, 763-785.

Workshop

Speakers

Francesca Barbieri, Hospital Clínic - IDIBAPS

Nils Berglund, Université d'Orléans

María J. Cáceres, Universidad de Granada

Tom Chou, University of California at Los Angeles

Albert Compte, Hospital Clínic–IDIBAPS

Stephen Coombes, University of Nottingham

Gustavo Deco, Universitat Pompeu Fabra

Mathieu Desroches, University of Bristol

Maria R. D'Orsogna, California State University

Carlos Escudero, Instituto de Matemáticas y Física Fundamental - CSIC

Oliver Faugeras, INRIA Sophia Antipolis-Méditerranée

Jordi García-Ojalvo, Universitat Politècnica de Catalunya

Pedro E. García, CRM - Universitat Pompeu Fabra

David Gómez-Cabrero, Universitat de València

Virginia González-Vélez, Universitat Autónoma Metropolitana México

Vincent Hakim, École Normale Supérieure

Rikkert Hidrinks, Vrije Universiteit Amsterdam

Simona Mancini, Université d'Orléans

Giovann Naldi, Università degli Studi di Milano

Louis Tao, Beijing University

David H. Terman, Ohio State University

Joaquín J. Torres, Universidad de Granada

Juan J.L. Velázquez, Consejo Superior de Investigaciones Científicas

Gilles Wainrib, Université Paris VII

Foreword

This set of notes arises from the generous effort and the material provided by the speakers both of the Advanced Course and the Workshop on "*Deterministic and Stochastic Modeling in Computational Neuroscience and Other Biological Topics*", to be held between May 11th to 15th, 2009, at the Centre de Recerca Matemàtica (CRM) in Bellaterra (Barcelona).

The three short-courses of the Advanced Course are thought of as an introduction to modeling, simulation and analysis in the different biological areas of this research programme. We want to open the scope not only to experts but also to young researchers (from master/doctorate programmes on applied mathematics, physics, bioengineering, biology,...), by showing some aspects of mathematical modeling through stochastic differential equations and facilitating the follow-up of the Workshop. Gustavo Deco's course, "*The neurodynamics of attention, memory and decision-making*", will dive in on more cognitive aspects of brain modeling and their simulation and analysis; under the title "*Modelling large-scale dynamics in the primary visual cortex*", Louis Tao will explain the modeling and the analytic treatment of this specific area of the visual pathway; finally, the course by Juan José L. Velázquez, "*Stochastic processes and PDEs in mathematical biology*", is intended to cover other aspects (both biological and mathematical) of modeling in biology based on stochastic partial differential equations.

The idea of this double event (Advanced Course+Workshop) emerged after the interaction among the organizers around common topics in different areas of mathematical biology; namely, the use of mean-field techniques. In mathematical and computational neuroscience, this topic has become one of the major streams in the theoretical treatment of populations of neurons, but we can also find instances in the other branches of this research programme: tumour growth and cancer modeling, population dynamics and adaptive dynamics. We found, thus, interesting to gather specialists in these problems in the Workshop, together with other specialists both from different approaches to the same biological problems and from more theoretical fields like stochastic differential equations or dynamical systems. Therefore, this Workshop is thought of as a meeting point for discussion on intersecting research problems. A major goal is to visualize the mathematical transversality across biology; that is, to see how similar mathematical tools apply to different biological problems. The speakers are invited to guide a session consisting of a lecture about some hot topic of their preference, followed by a discussion with the audience after each session. This format is intended to strengthen interactions among participants and, hopefully, to promote future collaborations. We want to express our gratitude to the direction and the staff of the CRM who helped us in the organization of the thematic research program "*Mathematical Biology: Modelling and Differential Equations*".

We thank the INGENIO MATHEMATICA programme of the Spanish government for providing financial support to the organization of this event.

We wish a fruitful scientific experience to all the participants, coming both from biology, computational and mathematical areas, but all of you eager to explore the intersections of your research with other fields. We wish you, as well, a very pleasant stay in Barcelona.

Co-ordinators:

Àngel Calsina,
Universitat Autònoma de Barcelona

José A. Carrillo,
Institució Catalana de Recerca i Estudis Avançats - Universitat Autònoma de Barcelona

Toni Guillamon,
Universitat Politècnica de Catalunya

1. Practical Information

Lodging arrangements:

Those of you who have to pay the lodging (written on the list) will need to do it on **Tuesday (April 14) at the CRM Administration with Mrs. Consol Roca**. We only accept payments **in cash** (we do not accept credit cards).

Lecture room:

The Workshop will take place in the CRM Auditori located in the Sciences Building (Edifici de Ciències), Universitat Autònoma de Barcelona in Bellaterra (http://www.crm.es/General/LocationEng.htm). The lecture room is equipped with a multimedia projector connected to a computer. An overhead projector and blackboards are also available. Please check the following map to know where the following places are: CRM, Vila Universitària and Hotel Serhs Campus.

Administration:

The CRM Administration will be available to the participants from Monday to Friday from 9:00 am to 5:00 pm.

Computer facilities:

The computer space of the CRM will be available for the participants of the Course with the following login information:

username:	crmactivities
password:	participant

The CRM premises as well as most of the UAB campus have wireless access. The CRM wireless login information is: crmwifikey

Breaks:

Coffee and cookies will be served during the breaks to all participants.

Lunch*:

We will post a list of restaurants where you can use your lunch tickets on the Workshop's bulletin board.

Social programme*:

The social programme of the Workshop and Advanced Course includes:

1. A social dinner, Thursday, May 14, at 20:30h at Citrus Restaurant in Barcelona. Free for registered participants not receiving grants. Registered participants receiving grants will be asked to pay a 5 euros registration fee. A fee of 40 euros will be applied to accompanying persons who would like to attend the dinner. Everyone interested in attending (both participants and accompanying persons) should sign up before **Tuesday, May 12 at noon** at the Administration.

2. A guided visit to the Gothic Quarter, Friday, May 15, at 17:00 free for all registered participants. However, you need to sign for it before **Wednesday, May 13 at noon** at the Administration (a minimum of 10 participants).

Picture:

A group picture will be taken on Wednesday, May 13 before the coffee break. We will inform you of the place to meet. The picture will be posted on the Workshop's web page.

Questionnaire:

Following the directions of the CRM Governing Board, we give a questionnaire to all the people participating in activities at the CRM in order to assess their level of satisfaction. The questionnaire is anonymous and not mandatory, but we would greatly appreciate it if you could answer the questions and return it to us. Thank you for your cooperation.

Local emergency numbers:

Medical emergency campus number	1800 / 1900 during office hours 2525 at other times
UAB's Science Faculty reception office	1055
General emergency (police, fire-fighters, ambulances)	112

* CRM Visitors come to the Administration and talk to Núria Hernández about the lunch tickets and the social dinner.

2. Schedule

Wednesday, May 13

9:30 – 10:10	*Mean-field descriptions of populations of neurons* **Olivier Faugeras**, INRIA Sophia-Antipolis-Mediterranée
10:10 – 10:50	*Stochastic neuronal dynamics* **Vincent Hakim**, École Normale Supérieure, Paris
10:50 – 11:20	Coffee Break
11:20 – 12:00	*Irregular persistent activity in a model of a local cortical network* **Francesca Barbieri**, Hospital Clínic - IDIBAPS
12:00 – 12.40	*Fluid limit theorems for stochastic hybrid systems with application to neuron models* **Gilles Wainrib**, Université Paris VII
12:40 – 13:10	**DISCUSSION**
13:10 – 15:00	Lunch
15:00 – 15:40	*Nested oscillations in the emergent activity of cortical networks* **Albert Compte**, Hospital Clínic - IDIBAPS
15:40 – 16:20	*Modeling neural networks with activity dependent synapses* **Joaquin J. Torres**, Universidad de Granada
16:20 – 16:40	Break
16:40 – 17:20	*Dynamical insigths on the history-dependence during continuous presentation of rivaling stimuli* **Pedro E. García**, CRM-Universitat Pompeu Fabra
17:20 – 17:50	*Exploring the specificity of the relationship between cortical network function and biological simulation parameters with a Particle Swarm Optimization algorithm* **David Gómez-Cabrero**, IDIBAPS
17:50 – 18:20	**DISCUSSION**

Thursday, May 14

9:30 – 10:10	*Stochastic models of excitable systems* **Nils Berglund**, Université d'Orléans
10:10 – 10:50	*Fokker-Planck models in neuroscience* **Maria J. Cáceres**, Universidad de Granada
10:50 – 11:20	Coffee Break
11:20 – 12:00	*A Fokker-Planck equation for interacting neurons* **Simona Mancini**, Université d'Orléans
12:00 – 12.30	*The use of stochastic differential equations in recovering synchronization dynamics from macroscopic recordings of neuronal activity* **Rikkert Hindriks**, Vrije Universiteit Amsterdam
12:30 – 13:00	**DISCUSSION**
13:00 – 15:00	Lunch
15:00 – 15:40	*Analyzing neuronal networks using discrete-time dynamical systems* **David H. Terman**, Ohio State University
15:40 – 16:20	*Dynamics of Morris-Lecar models* **Stephen Coombes**, University of Nottingham
16:20 – 16:40	Break
16:40 – 17:10	*Numerical computation of slow manifolds and canard orbits near a folded node - Application to neuronal systems* **Mathieu Desroches**, University of Bristol
17:10 – 17:40	*Modeling the dynamics of calcium-triggered cell exocytosis: a Monte Carlo approach* **Virginia González-Vélez**, Universidad Autónoma Metropolitana México
17:40 – 18:10	**DISCUSSION**
20:30 – 23:52	**Workshop dinner at Restaurant Citrus** (Passeig de Gràcia, 44. Barcelona 08007)

Friday, May 15

9:30 – 10:10	*Physics of viral entry* **Tom Chou**, University of California at Los Angeles
10:10 – 10:50	*Axon growth in neural development: sensing, transduction and movement* **Giovanni Naldi**, Università degli Studi di Milano
10:50 – 11:20	Coffee Break
11:20 – 12:00	*United by noise: randomness helps swarms stay together* **Carlos Escudero**, Instituto de Matemáticas y Física Fundamental - CSIC
12:00 – 12.40	*Patterns, stability and collapse for two-dimensional biological swarms* **Maria R. d'Orsogna**, California State University at Northridge
12:40 – 13:20	*Excitable dynamics of cell regulation* **Jordi García-Ojalvo**, Universitat Politècnica de Catalunya
13:20 – 14:00	**DISCUSSION** and Closing Session
14:00	Lunch
17:00 – 19:15	**Social Activity**

3. Abstracts of Speakers

Francesca Barbieri

Irregular persistent activity in a model of a local cortical network.

Abstract: Recent neuro-physiological experiments on monkeys (Compte et al. 2003) have reported highly irregular persistent activity during the performance of an oculomotor delayed-response task. These experiments show that during the delay period the ISI's coefficient of variation (CV) of prefrontal neurons is above 1, on average, and larger than during the fixation period, regardless of whether the cue is preferred or nonpreferred. Previous models (Amit and Brunel 1997, Brunel 2000) of spontaneous and selective persistent activity in the cortex based on excitatory synaptic feedback do not reproduce this feature because the excitatory feedback during persistent activity brings neurons in a region of the f-I curve in which the firing is relatively independent from fluctuations and hence the CV is small. To overcome this problem, we introduced two ingredients: (1) a high post-spike reset potential (close to threshold), (2) a non-linear relationship between synaptic efficacy and pre-synaptic firing rate via a short-term depression (STD) mechanism. We show that when the reset potential is close enough to the threshold, the CV-I curve has a maximum above 1 for a sub-threshold mean current. The range of the mean synaptic input values for which the CV is greater than 1 is always in the sub-threshold regime in which firing is dominated by fluctuations of the mean synaptic input. With short-term depression, synaptic efficacies saturate at a certain limiting value of the presynaptic frequency; this is turn provokes a saturation of the mean synaptic current to a neuron at the same limiting presynaptic frequency. This allows the persistent state solution to reach the region of the f-I curve which corresponds to high values of the CV. We tested this idea both with numerical simulations and analytical techniques. For the analytical studies we used mean- field techniques, recently extended in presence of STD (Romani et al. 2006), that involves the use of the distribution of the interspikes intervals of an integrate-and-fire neuron receiving a Gaussian current in input; this permits to obtain an accurate estimate of the statistic of the postsynaptic current in presence of STD and hence to find the stationary states in a self-consistent way. We simulated a fully connected excitatory network of leaky integrate-and-fire neurons endowed with STD and we found a very good agreement with theoretical prediction for a large range of synaptic efficacies.

Contact address: `barbierifrancesc@gmail.com`

Nils Berglund

Stochastic models of excitable systems.

Abstract: The generation of action potentials in neurons is sometimes described by differential equations with two well-separated time scale. We shall describe the effect of noise on such equations, in particular on the statistics of interspike times. (Joint work with Barbara Gentz, University of Bielefeld.)

References:

N.B. and Barbara Gentz, *Noise-Induced Phenomena in Slow-Fast Dynamical Systems. A Sample-Paths Approach.* Springer, Probability and its Applications (2005).

N.B. and Barbara Gentz, *Stochastic dynamic bifurcations and excitability*, in C. Laing and G. Lord, (Eds.) Stochastic methods in Neuroscience, Oxford University Press (2009).

Contact address: `nils.berglund@univ-orleans.fr`

María J. Cáceres,
Fokker-Planck models in neuroscience.

Abstract: We are interested in a Fokker-Planck model, which describes the behavior of neuronal networks in the mammalian neocortex. In the mammalian brains there are around 10^{10} neurons, which represents a sufficiently large number to think of a kinetic approach as appropriate. In [1], the authors presented a detailed theorical framework for statistical descriptions of neuronal networks and derived 2-dimensional kinetic equations directly from conductance-based integrate-and-fire neuronal networks (see [2]). They reduced the dimension via moment closures and also described different limits of these kinetic equations. In our present work we are studying a numerical method to simulate the Fokker-Planck equations developed for these models. We try to numerically validate the moment clousures and limits presented in [1], comparing numerically the stationary solutions of these models with the stationary distribution function of the Fokker-Planck equations. Our solver allows us to obtain the numerical evolution of the solution and to consider the distribution function depending of all the variables.

References:

[1] Cai, D., Tao, L., Rangan, A. V. and Mclaughlin, D. W., *Kinetic theory for neuronal network dynamics*, Comm. Math. Sci., **4(1)** (2006), 97–127.

[2] Koch, C., *Biophysics of Computation*, Oxford University Press, Oxford, 1999.

Contact address: `caceresg@ugr.es`

Tom Chou
Physics of viral entry.

Abstract: I will develop and analyze three stochastic models used to describe how certain viruses enter the cell. The first model concerns the stochastic engagement of receptors and the entry mechanisms of viruses. The second model describes the transport of virus material to to the host cell nucleus, while the third model is a revisit of the classic translocation problem used to model how polymers enter through membrane pores.

Contact address: `tomchou@ucla.edu`

Albert Compte
Nested oscillations in the emergent activity of cortical networks.

Abstract: Neural activity in the cerebral cortex is characterized by temporal dynamics at a variety of temporal frequencies. Two frequency bands have been shown to rely primarily on mechanisms of the local cortical circuit: the slow oscillation band ($<$ 1 Hz) and the beta/gamma-frequency band (20-80 Hz). I will present simulation results from a computational model of the cortical microcircuit showing the generation of these nested oscillations, in agreement with the experimental data obtained in cortical slices in vitro. The model consists of 1,000 excitatory neurons and 250 inhibitory neurons modeled according to the Hodgkin-Huxley formalism, including physiologically identified ion channels of cortical neurons, and interconnected through conductance-based synapses. The model identifies key physiological mechanisms that underlie the generation of the various rhythms and their propagation across the network.

Contact address: `acompte@clinic.ub.es`

Stephen Coombes
Dynamics of Morris-Lecar models.

Abstract: The Morris-Lecar (ML) neuron model is a two dimensional conductance based model that is often used as an idealised fast-spiking pyramidal neuron. Its planar nature has encouraged much analysis of the single neuron model using tools from phase-plane analysis and the "geometry of excitability". When treating synaptic or gap junction coupled networks of oscillating ML neurons these techniques are the natural basis for developing a weakly-coupled oscillator theory. However, to probe network dynamics in the strong coupling regime requires an alternative approach. I will show how results in this area can be obtained by using a piece-wise linear caricature of the ML model. In illustration of the usefulness of such an approach I will first consider gap junction coupling and show how to analyse emergent fluctuations in the mean membrane potential (as instabilities of an asynchronous network state). Next I will treat synaptically coupled networks with a phenomenological form of retrograde second messenger signalling that can support depolarisation induced suppression of excitation. In this case I will describe a mechanism for the emergence of ultra-low frequency synchronised oscillations

Contact address: `stephen.coombes@nottingham.ac.uk`

Mathieu Desroches
Numerical computation of slow manifolds and canard orbits near a folded node - Application to neuronal systems.

Abstract: We investigate the geometry of two-dimensional slow manifolds and the organisation of associated canard solutions in three-dimensional slow-fast vector fields with two slow variables. To this end, we introduce a numerical method, based on the numerical solution of families of two-point boundary value problems using continuation techniques, that allows to compute the slow manifolds. We can then identify and compute canard orbits as individual objects and follow them in parameter space, that is, we compute one-parameter families of canard solutions in dependence of a given system's parameter. In this way we get new insight into

their underlying bifurcation structure. We will present this numerical method in the case of two neuronal systems, namely, the self-coupled FitzHugh-Nagumo system and a three-dimensional reduction of the Hodgkin-Huxley equation. We show how canard orbits organise the geometry and the dynamics of associated mixed-mode oscillations.

Contact address: m.desroches@bristol.ac.uk

Maria R. D'Orsogna
Patterns, stability and collapse for two-dimensional biological swarms.

Abstract: Schools of fish, flocks of birds and swarms of insects self-organize in response to external stimuli or by direct interaction, forming beautiful, coherent patterns. How do these arise?

What are their properties?

How are individual characteristics linked to collective behaviours?

In this talk we discuss the swarming of a non-linear system of self propelled agents that interact via pairwise attractive and repulsive potentials. We are able to predict distinct aggregation morphologies, such as flocks and vortices, by utilizing statistical mechanics tools. We also relate the interaction potential to the collapsing or dispersing behaviour of agents. A kinetic theory is derived and we analyze the continuum limit of our model. Finally, we also discuss possible applications to the development of artificial swarming teams.

Contact address: dorsogna@math.ecla.edu

Carlos Escudero
United by noise: randomness helps swarms stay together.
(With C. A. Yates, R. Erban, I. D. Couzin, J. Buhl, I. G. Kevrekidis, P. K. Maini, and D. J. T. Sumpter).

Abstract: Amongst the most striking aspects of the movement of many animal groups are their sudden coherent changes in direction. Recent observations of locusts and starlings have shown that this directional switching is an intrinsic property of their motion. Similar direction switches are seen in self-propelled particle (SPP) and other models of group motion. Comprehending the factors which determine such switches is key to understanding the movement of these groups. Here we adopt a coarse-grained approach to the study of directional switching in a SPP model assuming an underlying one-dimensional Fokker-Planck equation (FPE) for the mean velocity of the particles. We continue with this assumption in analysing experimental data on locusts and use a similar systematic FPE coefficient estimation approach to extract the relevant information for the assumed FPE underlying that data. We determine the mean time between direction switches as a function of group density for the SPP model. This systematic approach allows us to identify key differences between the SPP model and the data, revealing that individual locusts increase the randomness of their movements in response to a loss of alignment by the group. We give a quantitative description of how locusts use noise to maintain swarm alignment. We discuss further how properties of individual animal behaviour, inferred using the FPE coefficient estimation approach,

can be implemented in the SPP model in order to replicate qualitatively the group level dynamics seen in the experimental data.

Reference:

C. A. Yates, R. Erban, C. Escudero, I. D. Couzin, J. Buhl, I. G. Kevrekidis, P. K. Maini, and D. J. T. *Sumpter, Inherent noise can facilitate coherence in collective swarm motion*, Proc. Natl. Acad. Sci. USA **106** (2009), 5464–5469.

Contact address: `cel@imaff.cfmac.csic.es`

Olivier Faugeras
Mean-field descriptions of populations of neurons.

Abstract: We present a general approach to the analysis of large sets of neurons. It is firmly grounded in the mathematics of stochastic analysis and principles of large deviations. We start from a description of individual neurons as obeying a set of stochastic differential equations (SDEs) such as those of Hodgkin-Huxley, a description of their synaptic interactions, and proceed to develop a mean-field analysis and description of the activity of each neuronal population when the number of neurons in each population becomes very large. Unlike other approaches, we rigorously establish the SDESs that describe each individual population.

These SDEs turn out to be non-Markovian and display a strong coupling between the moments of the probabilistic laws describing the population membrane potentials. We relate them to some popular neural-mass equations such as those established by Jansen and Rit that are quite heavily used in the modeling of such signals as EEG and MEG. In doing so we discover that the coupling between the mean membrane potentials and their covariances that results from our equations significantly alters the time response of the populations to a given stimulus. This fact seems to have been overlooked in previous work. We discuss some of the consequences of our analysis on the modeling of neural populations.

Contact address: `Olivier.Faugeras@inria.fr`

Jordi Garcia-Ojalvo
Excitable dynamics of cell regulation.

Abstract: Excitability is a paradigmatic dynamical state that has been found to have important implications in biology, especially in the field of neuronal dynamics. In this talk I will discuss examples of excitable dynamics in a different type of biological process, namely gene regulation. In particular, I will first consider the competence response to stress of the bacterium *Bacillus subtilis*. Experimental analysis of this behavior via time-lapse fluorescence microscopy, together with mathematical modeling, has allowed us to identify an excitable genetic circuit module that behaves in an excitable way. The study shows that competence for DNA uptake arises in this circuit as a noise-driven excitable state, with the corresponding quiescent state representing vegetative growth. Identification of this excitable module allows us to devise ways to control the excitable dynamics, which could shed light on the evolutionary origin of this phenotypic behavior. As a second example of excitable dynamics in gene regulation, I will discuss the maintenance of pluripotency in mouse embryonic stem cells.

Contact address: `jordi.g.ojalvo@upc.edu`

Pedro E. García

Dynamical insigths on the history-dependence during continuous presentation of rivaling stimuli.

(With G. Deco, A. Pastukhov, J. Braun, T. Guillamon).

Abstract: The presence of memory effects during the perception of interrupted presentation of images, which allow two or more incompatible interpretations, is well established [1, 2]. A recent work tackling the role of adaptation in bistable perception has demonstrated that consecutive dominances phases reported during continuous presentation of rivaling stimuli are neither statistically independent [3]. The generality of the result was confirmed by using different kind of stimuli (binocular rivalry, kinetic-depth effect, and Necker cube). The research is based on a novel concept in which a cumulative history for each reported percept during a session is computed by the exponential convolution – with time constant τ_{decay} – of the previous perceptual trace. Then a no monotonic profile for the history-dominance times correlation vs. τ_{decay} is obtained, reaching a significant maximum of $0.2 - 0.5$ at values $0.3 < \tau_{\text{decay}}/T_{\text{dom}} < 1$ ($T_{\text{dom}}-$ average dominance duration of the complete session). Amazingly, a significant influence of such an integral measure of history on transition times and transition direction is also detected. When the respective cumulative histories of both percepts were balanced, transition durations and the likelihood of return (failed) transitions peaked.

In contrast with the classic framework mainly described by adaptation and inhibition variables [4], the modest degree of the history dependence for the dominance phases, coupled with extended transitions in the event of balanced histories, seems to reveal an essentially noise driven nature of the perceptual reversals [5]. To clarify this hypothesis we carry out intensive computational simulations of a simple rate model in the adaptation (Φ_H) inhibition (β) strengths variables. Then we checked the capacity of the system to simultaneously fulfill various experimental constraints, such as a T_{dom} value of the order of seconds and a coefficient of variation (CV) of about 0.5, together with the observed ranges in 10 observers of the data collected for the history-dependence of dominance times, transitions durations and probability of uncompleted transition phases. The significant regions in the $(\Phi_H) - \beta$ for each observable is shown in the first two columns of Figure 1, by a pair of isolines delimiting the range of experimental values observed. Third column always shows the overlap of the two preceding figures in the same row, with the goal to find a parameters region fulfilling both constraints. An additional line indicates the boundary between two essentially different regimes: *bi-stable*, where noise is indispensable to get alternations between two states that represent the two possible interpretations of an ambiguous stimulus, and *oscillatory*, where it is just the source of dispersion in dominance time distribution as experimentally observed. As it can be observed, even when the data related with transitions remains difficult to be reproduced, such a simple model can account for the constraints related with T_{dom}, CV and the new ones about the correlation data. Additionally, the results obtained in [3] restricts even more the zone allowed by the previous known data about T_{dom} and CV. Coincidently, it can be seen that the system should operate in the vicinity of the bifurcation line and inside the *bi-stable* regime, extending the validity of the results of recent theoretical studies [6] to new parametric spaces. Further validation tests of the model includes the

capacity to reproduce the general trends of history-dependencies shown by transition durations, frequency of failed transitions and T_{dom} time series, as observed in [3].

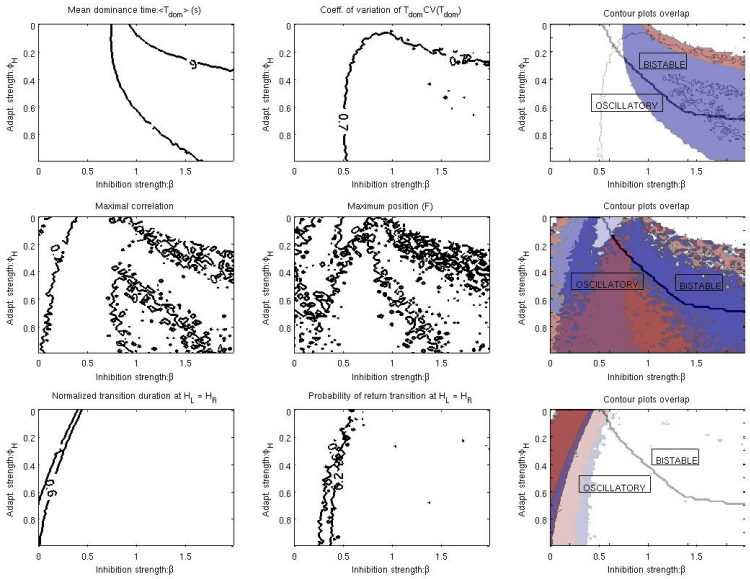

FIGURE 1. Computational simulations of a simple model in the "$\Phi_H - \beta$" parametric space. First row: Mean and Variation coefficient of dominance time; Second row: the maximum of $H - T$ correlation, and its position ($F = \tau / T_{\mathrm{mean}}$); Third row: Normalized transition duration and probability of a failed transition. An additional line in this third figure defines the boundary between bistable and oscillatory regions.

References:

[1] Pastukhov A., Braun J., *A short-term memory of multi-stable perception*, J. Vision 2008, **8(13)** (2008), 1–14.

[2] Brascamp JW., Knapen THJ., Kanai R., Noest AJ., van den Berg AV., *Multi-timescale perceptual history resolves visual ambiguity*, PLoS One 2008, **3(1)**: e1497.

[3] Pastukhov A., Braun J., Garcia P., Deco G., *History-dependence of multi-stable perception*, 2009 (to be submitted).

[4] Shpiro A., Curtu R., Rinzel J., Rubin N., *Dynamical characteristics common to neuronal competition models*, J. Neurophysiol. 2007, **97(1)** (2007), 462–473.

[5] Brascamp JW., Van Ee R., Noest AJ., Jacobs RHAH., van den Berg AV., *The time course of binocular rivalry reveals a fundamental role of noise*, J. Vision **6(11)** (2006), 1244–1256.

[6] Shpiro A., Moreno-Bote R., Rubin N. and Rinzel J., *Balance between noise and adaptation in competition models of perceptual bistability*, J. Comput. Neurosc., 2009 (in press).

Contact address:pedroernesto.garcia@gmail.com

David Gómez-Cabrero

Exploring the specificity of the relationship between cortical network function and biological simulation parameters with a Particle Swarm Optimization algorithm.

Abstract: Mechanistic aspects of brain function can be studied with the use of biologically detailed computational models. Often, a critical question that arises from these computational models is how critically the conclusions depend on a particular choice of the simulation parameters. It is difficult to establish that the presented network model is unique in producing the relevant phenomenology. This issue has been approached before for the case of single neurons or small networks of neurons. Here, we design a computational strategy to explore this for the case of large-scale biological neural network simulations. We focus on a specific neural function: visuo-spatial working memory, and we construct a biological neural network that mimics the cortical network. We search for sets of parameters such that the network sustains persistent activity. We design several evaluation functions that quantify this ability and weigh them in a proper way. To guide the search we rely on the Particle Swarm Optimization. The first objective is to find if there exists a unique solution or a set of significant different solutions. In the second case, we explore and typify the different areas of solutions. Analysis identify different types of solutions separated in the parameter space; this allow us to identify the main parameters associated with each behaviour, and give further insights of the model.

Contact address: david.gomez@uv.es

Virginia González-Vélez

Modelling the dynamics of calcium-triggered cell exocytosis: a Monte Carlo approach.

Abstract: The diffusion of different types of ions in the cytosol of living cells play a key role in their function. In particular, much attention has been paid to the diffusion of Ca2+ in intracellular media and for modeling this process there is a vast number of biological publications which rely on differential methods. The diffusion of calcium in the cytosol is also referred as calcium buffered diffusion. Models to describe buffered diffusion based on differential equations need drastic geometrical simplifications in order to be solved with ease. Depending on the geometrical assumptions considered most differential models lie within two categories: shell models, in which it is assumed that ions enter uniformly over the cell membrane and only the radial diffusion is of relevance (for spherical cells) and microdomain models, which solve the reaction diffusion equations in the vicinity of a channel pore, assuming azimuthal symmetry around the pore; in this last case it is necessary to assume that all channel pores are equidistant. However, it is well known that ions do not enter uniformly given that the channel pores are

not regularly spaced. These departures from symmetry may have an important impact on the functionality of the cells. In [1] it was described how the clustering of channels gives rise to calcium profiles which can not be obtained as a superposition of calcium concentrations developed by each individual channel. This non-linearity amplifies the effect of irregular distributions of calcium channels on the formation of submembrane calcium concentration profiles. With the idea in mind to overcome the geometrical simplifications imposed by differential methods, we developed a Monte Carlo simulation for the problem of 3-D buffered calcium diffusion [1, 2]. This scheme, which has proved to be successful in the study of the influence of the geometry in the exocytotic response of neuroendocrine cells [3, 4], is perfectly suitable for modelling exocytosis in presynaptic terminals, like the Calyx of Held synapse. We discuss resemblances and differences in the modelling of the exocytotic dynamics in both prototype cells.

References:

Gil A., Segura J., Pertusa JAG., and Soria B., *Monte Carlo simulation of 3-D buffered Ca2+ diffusion in neuroendocrine cells*, Biophys. J., **78(1)** (2000), 13–33.

[2]. Carrera G., Gil A., Segura J. and Soria B., *Software for simulating calcium-triggered exocytotic processes*, Am. J. Physiol. Cell. Physiol. **292** (2007), C749–C755.

[3] Segura J., Gil A., and Soria B., *Modeling study of exocytosis in neuroendocrine cells: inflluence of the geometrical parameters*, Biophys. J. **79(4)** (2000), 1771–1786.

[4] Gil A., González-Vélez V. and Segura J., *Stochastic modeling of L-type calcium channels and exocytosis in chromaffin cells*, European Biophysics Journal (to appear).

Contact address: vgv@correo.azc.uam.mx

Vincent Hakim

Stochastic neuronal dynamics.

Abstract: Neurons operate in vivo under strongly fluctuating inputs. I will introduce important quantities that help to analyze the ensuing stochastic dynamics. I will then show how they can be used to describe correlations between spike trains as well as oscillations in neuronal networks. Recent data on cerebellar cell networks will serve as an illustration.

Contact address: hakim@lps.ens.fr

Rikkert Hindriks

The use of stochastic differential equations in recovering synchronization dynamics from macroscopic recordings of neuronal activity.

Abstract: To study the mechanisms underlying large-scale synchronization processes in the human brain we fit coupled stochastic differential equations directly to human magnetoencephalographic (MEG) recordings. The used model allows for a characterization between neuronal interactions in phase and amplitude as well

as between interactions arising from deterministic and stochastic forces. We discuss the general applicability of coupled stochastic differential equations to model EEG/MEG recordings and address the statistical issues that arise.

While the use of stochastic differential equations in computational neuroscience is becoming widespread [1] their use in the analysis of macroscopic recordings of neural activity is still very limited. Most currently used EEG/MEG data-analysis methods focus on the detection and quantification of synchronization and do not provide insight into the dynamical mechanisms underlying the measurements. For this purpose, neuronal interaction is modeled explicitly and is directly fitted to the data. While deterministic synchronization models are increasingly used [2] the use of stochastic dynamical models is still very limited [3]. However, since noise is inherent to biophysical systems and given the meanfield nature of EEG/MEG recordings, models with a stochastic component are expected to provide a more realistic description of the electrophysiological processes underlying EEG/MEG recordings.

We fit a system of coupled stochastic differential equations to human MEG recordings of healthy subjects and Parkinsonian patients during a finger tapping task, localized to left and right primary motor cortices. We discuss the statistical issues that arise, like, an appropriate method to estimate drift and diffusion coefficients, how to check the goodness of fit, and how to assess the Markov property. The results provide insight into the dynamical mechanisms underlying interaction between primary motor cortices and their degradation as a consequence of Parkinson's disease.

References:

[1] Deco, G., Jirsa, V.K., Robsinson, P.A., Breakspear, M., Friston, K., *The dynamic brain: from spiking neurons to neural masses and cortical fields*, PLoS Comb. Biol. vol. 4, Issue 8, (2008).

[2] Hindriks, R., Bijma, F., van Dijk, B.W., Stam, C.J., van der Werf, Y.Y., van Someren, E.J.W., de Munck, J.C., van der Vaart, A. *Uncovering neuronal synchronization mechanisms from oscillatory data*, (submitted, December, 2008).

[3] Prusseit, J., Lehnerts, K. (2008): *Measuring interdependencies in dissipative dynamical systems with estimated Fokker-Planck coefficients*, Phys. Rev. E 77, 041914.

Contact address: `hindriks@few.vu.nl`

Simona Mancini

A Fokker-Planck equation for interacting neurons.

Abstract: We are interested in the study of the statistical properties of a large set of interacting neurons. Their behaviour is described in terms of the evolution of respective frequencies, whose dynamics is modelled by coupled stochastic ordinary differential equations, (ods), as done by Deco et al. From this system, we classically obtain a Fokker-Planck equation, describing the evolution in time of the distribution function with respect to the two family frequencies. We shall prove the existence, uniqueness and positivity of the solution at equilbrium for the Fokker- Planck model. Moreover, numerical simulations show that, at the equilibrium, the solution has double gaussian profile, which is the same obtained by

Deco et al. by means of moment analysis on the ods. Finally, we can compute the "escaping" time for differents values of the diffusion coefficient, and show that it has an exponential behaviour with respect to the diffusion coefficient.

Contact address: simona.mancini@univ-orleans.fr

Giovanni Naldi

Axon growth in neural development: sensing, transduction and movement.

Abstract: In the embryo, undifferentiated sets of cells form organized patterns following pathways marked by chemical cues. At this small scale, cues are represented by single molecules, displaced from their release location by diffusion. Diffusion is the movement of matter from areas with higher concentrations (near the source) to areas of lower concentrations. This works very much like the spreading by the grapevine of a metropolitan legend: news travel at a given speed and are subject to a progressive degradation. Cells crawl along the positive gradient, towards the direction of increasing chemical signal, from the periphery to the source. This establishes the controlled flow of material needed to build structured tissues. We may ask how far from its birthplace can we hear the metropolitan legend. Analogously, how far from its source can a chemical cue be found? The mathematics of diffusion shows that there exists a characteristic maximum reachable distance, called diffusion length, that depends on the volume (or on the weight) of the diffused molecule and on its activity time. Another aspect that we should consider is the fact that in the embryo, very much like in a noisy square, different cues are present at the same time. Following the chemical gradients can thus be as difficult as trying to localize (without a cell phone!) a friend who is calling us, lost in the crowd. How should we look for our friend and reach him? Cells work out the right direction sensing the chemical cues released in the environment, filtering out noise. To understand this mechanism, it is essential to dig into the process of gradient sensing. Cells try to detect very small differences in molecule concentration across their tiny diameter. With this respect, they behave like an instrument that counts molecules in its surroundings and is allowed only a limited number of probings. The study of the measurement errors of such an instrument can explain the shape of the trajectories. Moreover, we know that repeating the measure can reduce uncertainty, but it requires more time. A mathematical model of the measuring process and of the subsequent cell motion sheds light on the balance between the unevenness of trajectories and the time span of the motion in different conditions. This analysis can explain why neurons grow more slowly when the surrounding environment is more complex, for example when they have to perform sharp turns like when they approach the developing spinal cord. The model also suggests that some sort of amplification of the signal must occur inside the cell. This effect stems from a cascade of intracellular biochemical reactions that are only partially known to biologists. Mathematics can predict the magnitude of the amplification needed to separate a weak, but coherent signal, from the background noise and explain how even a couple of molecules in more in a certain direction can make the difference for life.

This is a joint work with P. Causin, G. Aletti (University of Milano, Italy), A. Zaghetto (Dulbecco Telethon Institute CNR-ITB, Italy), and G. Merlo (University of Torino, Italy).

Contact address: Giovanni.Naldi@mat.unimi.it

David H. Terman
Analyzing neuronal networks using discrete-time dynamical systems.

Abstract: We describe mathematical techniques for analyzing detailed biophysical models for excitatory-inhibitory neuronal networks. While these networks arise in numerous applications, the focus of this talk will be to better understand mechanisms that underlie temporally dynamic responses in the olfactory system. Our strategy is to first reduce the model to a discrete-time dynamical system. Using the discrete model, we can systematically study how the emergent firing patterns depend on parameters including the underlying network architecture.

Contact address: terman@math,ohio-state.edu

Joaquín J. Torres
Modeling neural networks with activity dependent synapses.

Abstract: In this talk, I review some of our recent work over the effect of activity-dependent synaptic processes, such as short-time depression and facilitation, on the emergent behavior of recurrent neural networks.

Depending on the synapse dynamics, different types of behavior can emerge, including a standard recall phase, a novel oscillatory regime, and a non-recall phase. In the oscillatory phase, the activity of the network continously jumps between different attractors associated to previously stored patterns. Our study have shown that the interplay between synaptic depression and stochasticity is important for destabilizing the attractors. This property is enhanced by synaptic facilitation which, therefore, improves the adaptation of the system to external stimuli. A detailed analysis of the network also reflects an efficient (more rapid and with less error) access to the memories when facilitation is increased. We also investigated the influence of facilitation and depression on the maximum storage capacity of the network. Our study shows that synaptic depression drastically reduces the capacity of the system to store an retrieve memories. Facilitation, however, enhances the memory capacity in different situations. In particular, we found optimal values of the relevant synaptic parameters for which the storage capacity can be maximal and similar to the one obtained with "static" synapses. We conclude that depressing synapses with a certain level of facilitation allow to recover the good retrieval properties of neural networks with static synapses while maintaining the nonlinear properties of dynamic synapses, convenient for dynamical information processing and coding.

Contact address: jtorres@ugr.es

Gilles Wainrib

Fluid limit theorems for stochastic hybrid systems with application to neuron models.

Abstract: Neurons are subject to various source of noise, both extrinsic and intrinsic. The main source of intrinsic noise is the stochastic behaviour of ion channels. Within the framework of stochastic hybrid processes, we establish mathematical results describing the limit of large number of ion channels.

Contact address: `wainrib.gilles@ ijm.jussieu.fr`

4. List of Participants

Name	Institution
Aalto, Daniel	University of Turku, Finland
Alabert Romero, Aureli	Universitat Autònoma de Barcelona, Spain
Andoni, Sari	University of Texas at Austin, USA
Barbieri, Francesca	Hospital Clínic - IDIBAPS, Spain
Berglund, Nils	Université d'Orléans, France
Borges Rutz, Ricardo	Universitat Autònoma de Barcelona, Spain
Cáceres, María J.	Universidad de Granada, Spain
Calsina, Àngel	Universitat Autònoma de Barcelona, Spain
Cano Colino, Maria	Hospital Clínic - IDIBAPS, Spain
Cañizo Rincón, José A.	Universitat Autònoma de Barcelona, Spain
Carrillo de la Plata, José A.	Universitat Autònoma de Barcelona, Spain
Cecilla Real, Enric	Universitat Barcelona, Spain
Chou, Tom	University of California at Los Angeles, USA
Compte Braquets, Albert	Hospital Clínic - IDIBAPS, Spain
Coombes, Stephen	University of Nottingham, United Kingdom
Cordier, Stéphane	Université d'Orléans, France
Cuadrado Gavilán, Sílvia	Universitat Autònoma de Barcelona, Spain
de Franciscis, Sebastiano	Universidad de Granada, Spain
Deco, Gustavo	Universitat Pompeu Fabra, Spain
Delshams Valdés, Amadeu	Universitat Politècnica de Catalunya, Spain
Desroches, Mathieu	University of Bristol, United Kingdom
Dies Miracle, Marta	Universitat Pompeu Fabra, Spain
D'Orsogna, Maria R.	California State University, USA
Echebarria, Blas	Universitat Politècnica de Catalunya, Spain
Escudero Liébana, Carlos	Instituto de Matemáticas y Física Fundamental - CSIC, Spain
Faugeras, Olivier	INRIA Sophia-Antipolis-Mediterranée
Font Martinez, Francesc	Universitat Politècnica de Catalunya, Spain
Galtier, Mathieu	INRIA Odyssee project, France
Garcia-Ojalvo, Jordi	Universitat Politecnica de Catalunya, Spain

Name	Institution
García, Pedro E.	CRM - Universitat Pompeu Fabra, Spain
Giovannucci, Andrea	Universitat Pompeu Fabra, Spain
Gómez-Cabrero, David	Universitat de València, Spain
Gómez-Marin, Alex	Centre de Regulació Genòmica, Spain
González Vélez, Virginia	Universidad Autónoma Metropolitana, México
Guillamon Grabolosa, Antoni	Universitat Politècnica de Catalunya, Spain
Gulliksson, Mårten	Mid Sweden University, Sweden
Hakim, Vincent	École Normale Supérieure, France
Herreros Alonso, Ian	Universitat Pompeu Fabra, Spain
Hindriks, Rikkert	Vrije Universiteit Amsterdam, Netherlands
Huguet Casades, Gemma	Centre de Recerca Matemàtica, Spain
Jarynowski, Andrzej	Wroclaw University of Technology, Poland
Kutafina, Ekaterina	University of Science and Technology, Poland
Landon, Damien	Université d'Orléans, France
Mancini, Simona	Université d'Orléans, France
Martínez Garcia, Marina	Universitat Politècnica de Cataluyna, Spain
Mejias, Jorge F.	Universidad de Granada, Spain
Naldi, Giovanni	Università degli studi di Milano, Italy
Oleynik, Anna	Norwegian University of Life Sciences, Norway
Perthame, Benoît	École Normale Supérieure de Paris, France
Polania, Rafael	Göttingen Universität, Germany
Rivas Cañas, Manolo	Universitat Politècnica de Catalunya, Spain
Rivaud Gallardo, Juan J.	Universitat Autònoma de Barcelona, Spain
Rosado Linares, Jesús	Universitat Autònoma de Barcelona, Spain
Rué, Pau	Univeristat Pompeu Fabra, Spain
Serna, Susana	Universitat Autònoma de Barcelona, Spain
Shlykova, Irina	Norwegian University of Life Sciences, Norway
Tao, Louis	Peking University, China
Terman, David H.	Ohio State University at Columbus, USA
Tierz, Miguel	Brandeis University, USA

Name	Institution
Tojtovska, Biljana	University “Sts Cyril and Methodius”, Macedonia
Torres, Joaquín J.	Universidad de Granada, Spain
Trenado Colin, Carlos	Saarland University Hospital, Germany
Trussard, Marie	Hospital Clínic - IDIBAPS, Spain
Utzet Civit, Frederic	Universitat Autònoma de Barcelona, Spain
Velázquez, Juan J.L.	Consejo Superior de Investigaciones Científicas
Veltz, Romain	INRIA Sophia Antipolis, France
Wainrib, Gilles	Université Paris VII, France
Zafar, Sundus Chalmers	University of Technology, Sweden